

An isogeometric finite element formulation for boundary and shell viscoelasticity based on a multiplicative surface deformation split

Karsten Paul^a and Roger A. Sauer^{a,b,c,*}

^a*Aachen Institute for Advanced Study in Computational Engineering Science (AICES),
RWTH Aachen University, Templergraben 55, 52062 Aachen, Germany*

^b*Faculty of Civil and Environmental Engineering, Gdańsk University of Technology,
ul. Gabriela Narutowicza 11/12, 80-233 Gdańsk, Poland*

^c*Department of Mechanical Engineering, Indian Institute of Technology Guwahati,
Assam 781039, India*

Published¹ in *International Journal for Numerical Methods in Engineering*,
doi: [10.1002/nme.7080](https://doi.org/10.1002/nme.7080)

Submitted on March 21, 2022; Revised on June 23, 2022; Accepted on June 24, 2022

Abstract: This work presents a numerical formulation to model isotropic viscoelastic material behavior for membranes and thin shells. The surface and the shell theory are formulated within a curvilinear coordinate system, which allows the representation of general surfaces and deformations. The kinematics follow from Kirchhoff-Love theory and the discretization makes use of isogeometric shape functions. A multiplicative split of the surface deformation gradient is employed, such that an intermediate surface configuration is introduced. The surface metric and curvature of this intermediate configuration follow from the solution of nonlinear evolution laws – ordinary differential equations (ODEs) – that stem from a generalized viscoelastic solid model. The evolution laws are integrated numerically with the implicit Euler scheme and linearized within the Newton-Raphson scheme of the nonlinear finite element framework. The implementation of membrane and bending viscosity is verified with the help of analytical solutions and shows ideal convergence behavior. The chosen numerical examples capture large deformations and typical viscoelasticity behavior, such as creep, relaxation, and strain rate dependence. It is also shown that the proposed formulation can be straightforwardly applied to model boundary viscoelasticity of 3D bodies.

Keywords: Viscoelasticity, Kirchhoff-Love shells, multiplicative split, isogeometric analysis, nonlinear finite element methods, surface elasticity

1 Introduction

Thin-walled structures are common to many engineering branches, as they have low weight combined with high strength. A suitable approach to model these structures is Kirchhoff-Love theory, especially for very slender structures. Many materials, such as polymers, bitumens, biological materials, and several metals or plastics at elevated temperatures, exhibit viscoelastic behavior, i.e. they show both elastic and viscous material properties. Elastic materials return to their original shape instantaneously once the applied loads are removed, whereas viscoelastic

*corresponding author, email: sauer@aices.rwth-aachen.de

¹This pdf is the personal version of an article whose journal version is available at <https://onlinelibrary.wiley.com>

materials return to their original shape gradually. For large deformations, the elastic and viscous deformations are in general modeled by a multiplicative split of the deformation gradient, which leads to an additive split of certain strains.

Kirchhoff-Love theory considers thin shells, such that out-of-plane shear strains can be neglected. Therefore, the cross-section always remains orthogonal to the shell's mid-plane during deformation. The governing equation of Kirchhoff-Love shells contains higher-order derivatives, as it describes bending in terms of deformation and not in terms of rotation. The weak form thus requires C^1 -continuity, which poses a requirement on the numerical discretization. Isogeometric analysis (IGA), introduced by Hughes et al. (2005), offers the possibility of discretizations with higher continuity by making use of splines for the description of the geometry and the solution, as is discussed in detail in Cottrell et al. (2009). IGA has interesting mathematical properties (Evans et al., 2009) and can be integrated into standard finite element codes by performing the numerical integration of smooth basis functions on Bézier elements (Borden et al., 2011) or Lagrange elements (Schillinger et al., 2016). Nguyen et al. (2015) provide an overview on isogeometric analysis and discuss implementation aspects. Isogeometric Kirchhoff-Love shells have been intensively studied in the literature, starting with Kiendl et al. (2009). Further works on isogeometric shells followed, such as blended shells (Benson et al., 2013), hierarchical shells (Echter et al., 2013), and large-strain Kirchhoff-Love shells (Kiendl et al., 2015; Duong et al., 2017). For complex engineering problems, single patches are often not sufficient to represent shell geometries, such that multi-patch descriptions are required. The continuity of such discretizations is not preserved at patch interfaces and needs to be restored, see Paul et al. (2020a) for a recent review on patch enforcement techniques in isogeometric analysis. Isogeometric analysis has been used within several shell and membrane applications, such as laminated composite shells (Thai et al., 2012; Deng et al., 2015), anisotropic shells (Nagy et al., 2013; Faroughi et al., 2020), shape optimization of shells (Kiendl et al., 2014; Hirschler et al., 2019), liquid membranes (Sauer, 2014; Roohbakhshan and Sauer, 2019), biological tissues (Tepole et al., 2015; Roohbakhshan and Sauer, 2017), topology optimization of shells (Kang and Youn, 2016; Zhang et al., 2020), shell fracture (Ambati and De Lorenzis, 2016; Kiendl et al., 2016), lipid bilayers (Sauer et al., 2017; Bartezzaghi et al., 2019), 2D materials (Ghaffari et al., 2018, 2019), shell elastoplasticity (Ambati et al., 2018; Huynh et al., 2020), inverse analysis of shells (Vu-Bac et al., 2018; Borzeszkowski et al., 2022), Cahn-Hilliard phase separations on deforming surfaces (Valizadeh and Rabczuk, 2019; Zimmermann et al., 2019), adaptive surface refinement (Paul et al., 2020b; Proserpio et al., 2020), and fiber-reinforced shells (Schulte et al., 2020; Duong et al., 2022).

The rigorous treatment of linear viscoelasticity dates back to the works by Coleman and Noll (1961) and Crochet and Naghdi (1969). Extensions to finite viscoelasticity have been provided by Koh and Eringen (1963) and Sidoroff (1974). Finite element implementations of viscoelasticity followed by Simo (1987) and Govindjee and Simo (1992). Reese and Govindjee (1998) present a theory for finite viscoelasticity based on a multiplicative split of the deformation gradient. Recent discussions on the origin, mathematics and application of the multiplicative split are provided by Lubarda (2004), Gupta et al. (2007), and Reina et al. (2018). Shaw et al. (1999) describe viscoelastic material models and discuss their numerical treatment including spatial adaptivity of the discretization. Miehe and Keck (2000) present a model for filled rubbery polymers considering a superimposed finite elastic-viscoelastic-plastoelastic stress response with damage and they discuss its numerical implementation. Holzapfel and Gasser (2001) provide a model for viscoelastic fiber-reinforced composites at finite strains and compare its finite element results with experimental data. Bonet (2001) proposes a continuum formulation for viscoelastic materials and corresponding constitutive models considering finite deformations. Adolfsson and Enelund (2003) make use of fractional derivatives to model large strain vis-

coelasticity. [Fancello et al. \(2006\)](#) propose a general variational framework for finite viscoelastic models and compare several models with each other. [Amin et al. \(2006\)](#) consider finite strain viscoelasticity of rubbers and investigate the effects of internal variables on viscous phenomena based on experiments and numerical models. [Hossain et al. \(2010\)](#) focus on the modeling of polymer curing by considering viscoelasticity and shrinking at finite strains. [Kästner et al. \(2012\)](#) propose an experimental procedure to classify the nonlinear, inelastic mechanical behavior of polymers and derive a corresponding material model. [Marques and Creus \(2012\)](#) provide a summary on computational viscoelasticity. [Shutov et al. \(2013\)](#) suggest an explicit solution for an implicit time stepping scheme used in finite strain viscoelasticity based on a multiplicative split of the deformation gradient. [James and Waisman \(2016\)](#) demonstrate the importance of the viscoelastic response in structural design optimization.

The extension of viscoelasticity to shells has been addressed in fewer works. [Evans and Hochmuth \(1976\)](#) propose a theory for viscoelastic membranes under large deformations and apply it to red cell discocytes. [Neff \(2005\)](#) provide the first model for viscoelastic membranes and shells based on the classical multiplicative split of the deformation gradient. Such a split can also be formulated directly on the surface, as was shown in the recent work of [Sauer et al. \(2019\)](#). Additive decompositions are used for erythrocyte membranes ([Lubarda, 2011](#)), for shell formulations based on three-dimensional viscoelasticity ([Li, 2012](#)), for micropolar plates and shells ([Altenbach and Eremeyev, 2015](#)), and for fiber reinforced composite shells ([Dörr et al., 2017](#)). [Liu et al. \(2017\)](#) consider surface viscoelasticity coupled with three-dimensional viscoelastic bulks to model cells and cell aggregates. [Hernandez et al. \(2020\)](#) study viscoelastic behavior of Reissner-Mindlin shells. [Dadgar-Rad and Firouzi \(2021\)](#) consider incompressible membranes and quasi-linear viscoelasticity. Following the work on surface elasticity by [Javili and Steinmann \(2009, 2010\)](#), [Dortdivanlioglu and Javili \(2021\)](#) develop a theory for nonlinear surface viscoelasticity at finite strains by accounting for strain-dependent boundary stresses.

Recently, viscoelasticity has also been considered in isogeometric analysis. The work of [Dortdivanlioglu and Javili \(2021\)](#) uses IGA, while [Shafei et al. \(2021\)](#) make use of isogeometric analysis for the analysis of nonlinear vibration of viscoelastic plates. Further, [Sun et al. \(2021\)](#) employ the isogeometric boundary element method to investigate viscoelastic materials.

The present work makes use of the new multiplicative surface deformation split of [Sauer et al. \(2019\)](#) in order to model isotropic viscoelastic material behavior of thin shell structures. Here, the flexibility and consistency of this split are demonstrated and the corresponding computational formulation is described. The nonlinear isogeometric thin shell formulation follows the work of [Duong et al. \(2017\)](#), see also Remark 1.1. The proposed formulation thus benefits from efficiency and accuracy gains provided by rotation-free isogeometric finite element formulations. A generalized viscoelastic solid is considered to model both membrane and bending viscosity, see also Remark 1.2. Several material models are outlined and a time integration scheme is presented to solve the evolution laws. Several material models are outlined and a time integration scheme is presented to solve the evolution laws. For several special cases, analytical solutions are derived. It is further shown that the proposed formulation can be applied to model boundary viscoelasticity of 3D bodies without any further modifications. In summary, the formulation in the present work

- employs a multiplicative split of the surface deformation gradient for large strains,
- allows to flexibly describe in-plane and out-of-plane viscoelasticity,
- captures typical viscoelastic effects, such as creep, relaxation, and strain rate dependency,
- uses an isogeometric finite element implementation,

- uses numerical time integration to solve the evolution laws,
- is verified by several analytical solutions,
- exhibits ideal convergence rates, and
- can model boundary viscoelasticity of 3D bodies without any further modifications.

Remark 1.1: The employed shell formulation is based on a direct surface approach, which directly formulates the kinematical quantities, balance laws and constitutive relations (in particular) for the surface, without resorting to 3D counterparts. The approach is consistent with 3D continuum mechanics, because the underlying kinematical assumptions, balance laws and constitutive principles are the same. It is therefore possible to show their equivalency for certain constitutive models (Duong et al., 2017), see also Remark 3.1. The direct surface approach enables a straightforward decomposition of the elastic energy density into membrane and bending contributions, which makes the constitutive modeling more flexible. Thus, the proposed approach admits any hyperelastic and viscous material that is consistent with the principles of material modeling such as the second law of thermodynamics.

Remark 1.2: The proposed formulation captures two separate cases in a unified manner: shell viscoelasticity (that includes membrane viscoelasticity as a special case) and boundary viscoelasticity of 3D bodies – a case which is sometimes referred to as *surface viscoelasticity* in the literature (Liu et al., 2017; Dortdivanlioglu and Javili, 2021). In the two cases, the term *surface* therefore either refers to the mid-plane of the shell or the boundary of the 3D solid. The separation into the two cases is only conceptual. Mathematically and computationally the two cases become identical in the proposed formulation. For brevity, terms like *surface viscoelasticity* are therefore simply used to subsume both cases.

The remainder of this paper is structured as follows: Sec. 2 summarizes the surface description and kinematics considering the multiplicative split of the surface deformation gradient. Sec. 3 describes constitutive relations and the extension of hyperelasticity to account for membrane and bending viscosity. In Sec. 4, the computational formulation including the time integration scheme and the linearization is outlined. Sec. 5 presents several numerical examples that highlight viscoelastic material behavior and ideal convergence rates. Sec. 6 concludes this paper with a summary and an outlook.

2 The multiplicative surface deformation split

This section summarizes the continuum formulation of viscoelastic shells based on a curvilinear surface description and the multiplicative surface deformation split of Sauer et al. (2019). A concise summary of the mathematical background of the thin shell theory can be found in Sauer (2018).

2.1 Surface description

The surface description is based on the four different domains shown in Fig. 1. The parameter domain is denoted by \mathcal{P} , while the reference, intermediate and current surface are denoted by \mathcal{S}_0 , $\hat{\mathcal{S}}$, and \mathcal{S} , respectively. The introduction of the intermediate configuration is required to account for deformations composed of two separate components, i.e. elastic and inelastic components. The mapping $\mathbf{X}(\xi^\alpha)$ describes the reference surface and it associates the covariant basis $\{\mathbf{A}_\alpha, \mathbf{N}\}$ to each surface point. Here, ξ^α ($\alpha = 1, 2$) denote the convective coordinates, \mathbf{A}_α are the tangent vectors and \mathbf{N} is the surface normal. In analogy, the current surface \mathcal{S} follows from $\mathbf{x}(\xi^\alpha, t)$ with covariant basis $\{\mathbf{a}_\alpha, \mathbf{n}\}$. Time is denoted t . In the intermediate configuration, the covariant basis is denoted $\{\hat{\mathbf{a}}_\alpha, \hat{\mathbf{n}}\}$. The deformation $\mathcal{S}_0 \rightarrow \hat{\mathcal{S}}$ is taken as the inelastic part (‘in’), and $\hat{\mathcal{S}} \rightarrow \mathcal{S}$ as the elastic part (‘el’).

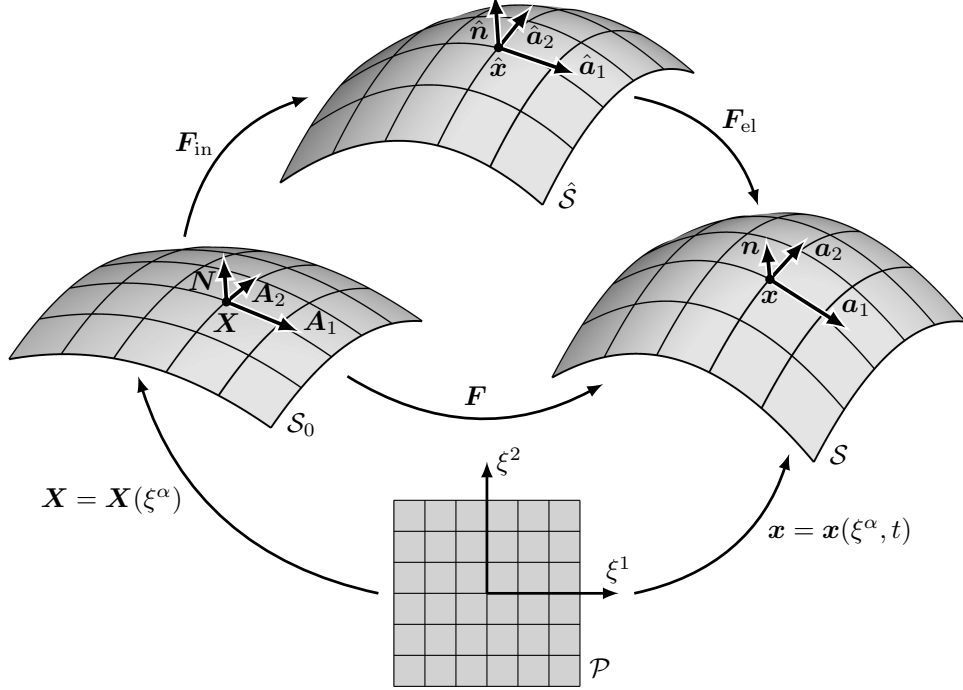


Figure 1: Surface mappings with the multiplicative surface deformation split into inelastic and elastic components (Sauer et al., 2019).

Given the mapping $\mathbf{x}(\xi^\alpha, t)$, the tangent vectors and surface normal follow as

$$\mathbf{a}_\alpha = \frac{\partial \mathbf{x}}{\partial \xi^\alpha}, \quad \text{and} \quad \mathbf{n} = \frac{\mathbf{a}_1 \times \mathbf{a}_2}{\|\mathbf{a}_1 \times \mathbf{a}_2\|}, \quad (1)$$

such that in-plane and out-of-plane surface objects can be characterized. The tangent vectors define the covariant surface metric with components

$$a_{\alpha\beta} = \mathbf{a}_\alpha \cdot \mathbf{a}_\beta, \quad (2)$$

which describe length and angle changes. In general, the basis $\{\mathbf{a}_\alpha, \mathbf{n}\}$ is not orthonormal. Orthonormality is restored by introducing a contravariant basis $\{\mathbf{a}^\alpha, \mathbf{n}\}$ through

$$\mathbf{a}^\alpha = a^{\alpha\beta} \mathbf{a}_\beta, \quad \text{with} \quad [a^{\alpha\beta}] = [a_{\alpha\beta}]^{-1}, \quad (3)$$

where $a^{\alpha\beta}$ refers to the contravariant surface metric. Note that index notation is used here, such that summation from 1 to 2 is implied on all terms with repeated Greek indices. Now, $\mathbf{a}^\alpha \cdot \mathbf{a}_\beta = \delta_\beta^\alpha$ with Kronecker delta δ_β^α .

The second parametric derivative $\mathbf{x}_{,\alpha\beta} = \mathbf{a}_{\alpha,\beta} = \partial \mathbf{a}_\alpha / \partial \xi^\beta$ is introduced to define the surface curvature

$$b_{\alpha\beta} = \mathbf{a}_{\alpha,\beta} \cdot \mathbf{n}. \quad (4)$$

It can be used to determine the mean and Gaussian curvature

$$H = 1/2 a^{\alpha\beta} b_{\alpha\beta}, \quad \text{and} \quad \kappa = \det[b^{\alpha\beta}], \quad (5)$$

respectively, where $[b^{\alpha\beta}] = [a^{\alpha\gamma} b_{\gamma\beta}]$. In contrast to the parametric derivative $\mathbf{a}_{\alpha,\beta}$, the covariant derivative of \mathbf{a}_α can be defined as $\mathbf{a}_{\alpha;\beta} := (\mathbf{n} \otimes \mathbf{n}) \mathbf{a}_{\alpha,\beta}$.

The description of the reference surface \mathcal{S}_0 follows in analogy to the surface description of \mathcal{S} presented above. The intermediate configuration $\hat{\mathcal{S}}$ is described by the unknown tangent vectors

$\hat{\mathbf{a}}_\alpha$. Given these tangent vectors, the intermediate surface quantities can be characterized analogously to \mathcal{S}_0 and \mathcal{S} . For the reference surface, capital letters or the index ‘0’ are used, whereas quantities on the intermediate configuration are denoted with a hat, ‘ $\hat{\bullet}$ ’. The intermediate surface metric $\hat{a}_{\alpha\beta}$ and curvature $\hat{b}_{\alpha\beta}$ are particularly important to describe viscoelasticity. These quantities follow in analogy to Eqs. (2) and (4).

2.2 Surface kinematics

Fig. 1 shows that the mappings between the different surface configurations are characterized by the surface deformation gradient \mathbf{F} , or its elastic or inelastic part, \mathbf{F}_{el} and \mathbf{F}_{in} , respectively. They are given by

$$\mathbf{F} = \mathbf{a}_\alpha \otimes \mathbf{A}^\alpha, \quad \mathbf{F}_{\text{el}} = \mathbf{a}_\alpha \otimes \hat{\mathbf{a}}^\alpha, \quad \text{and} \quad \mathbf{F}_{\text{in}} = \hat{\mathbf{a}}_\alpha \otimes \mathbf{A}^\alpha, \quad (6)$$

such that the deformation gradient is multiplicatively split into its elastic and inelastic part, i.e. $\mathbf{F} = \mathbf{F}_{\text{el}} \mathbf{F}_{\text{in}}$. Based on this split, the tangent vectors can be expressed as

$$\begin{aligned} \mathbf{A}_\alpha &= \mathbf{F}_{\text{in}}^{-1} \hat{\mathbf{a}}_\alpha = \mathbf{F}^{-1} \mathbf{a}_\alpha, & \hat{\mathbf{a}}_\alpha &= \mathbf{F}_{\text{in}} \mathbf{A}_\alpha = \mathbf{F}_{\text{el}}^{-1} \mathbf{a}_\alpha, & \mathbf{a}_\alpha &= \mathbf{F}_{\text{el}} \hat{\mathbf{a}}_\alpha = \mathbf{F} \mathbf{A}_\alpha, \\ \mathbf{A}^\alpha &= \mathbf{F}_{\text{in}}^{\text{T}} \hat{\mathbf{a}}^\alpha = \mathbf{F}^{\text{T}} \mathbf{a}^\alpha, & \hat{\mathbf{a}}^\alpha &= \mathbf{F}_{\text{in}}^{-\text{T}} \mathbf{A}^\alpha = \mathbf{F}_{\text{el}}^{\text{T}} \mathbf{a}^\alpha, & \mathbf{a}^\alpha &= \mathbf{F}_{\text{el}}^{-\text{T}} \hat{\mathbf{a}}^\alpha = \mathbf{F}^{-\text{T}} \mathbf{A}^\alpha. \end{aligned} \quad (7)$$

Based on the surface deformation gradient \mathbf{F} in Eq. (6), the surface Cauchy-Green tensors can be determined, i.e.

$$\mathbf{C} = \mathbf{F}^{\text{T}} \mathbf{F} = a_{\alpha\beta} \mathbf{A}^\alpha \otimes \mathbf{A}^\beta, \quad \text{and} \quad \mathbf{B} = \mathbf{F} \mathbf{F}^{\text{T}} = A^{\alpha\beta} \mathbf{a}_\alpha \otimes \mathbf{a}_\beta. \quad (8)$$

They have the two invariants

$$I_1 = \mathbf{I} : \mathbf{C} = \mathbf{i} : \mathbf{B} = A^{\alpha\beta} a_{\alpha\beta}, \quad \text{and} \quad J = \frac{\sqrt{\det[a_{\alpha\beta}]}}{\sqrt{\det[A_{\alpha\beta}]}}, \quad (9)$$

The second invariant in Eq. (9) characterizes the surface stretch between \mathcal{S}_0 and \mathcal{S} . Based on the surface identities $\mathbf{I} = \mathbf{A}_\alpha \otimes \mathbf{A}^\alpha$ on \mathcal{S}_0 and $\mathbf{i} = \mathbf{a}_\alpha \otimes \mathbf{a}^\alpha$ on \mathcal{S} and Eq. (8), the surface Green-Lagrange and surface Almansi strain tensors follow as

$$\mathbf{E} = \frac{1}{2} (\mathbf{C} - \mathbf{I}) = \varepsilon_{\alpha\beta} \mathbf{A}^\alpha \otimes \mathbf{A}^\beta, \quad \text{and} \quad \mathbf{e} = \frac{1}{2} (\mathbf{i} - \mathbf{B}^{-1}) = \varepsilon_{\alpha\beta} \mathbf{a}^\alpha \otimes \mathbf{a}^\beta, \quad (10)$$

respectively. In Eq. (10), the strain components are given by

$$\varepsilon_{\alpha\beta} = \frac{1}{2} (a_{\alpha\beta} - A_{\alpha\beta}). \quad (11)$$

Now, the right surface Cauchy-Green tensor can be pushed forward to the intermediate configuration, and the inverse of the left surface Cauchy-Green tensor can be pulled back to the intermediate configuration, i.e.

$$\begin{aligned} \mathbf{C}_{\text{el}} &:= \mathbf{F}_{\text{in}}^{-\text{T}} \mathbf{C} \mathbf{F}_{\text{in}}^{-1} = \mathbf{F}_{\text{el}}^{\text{T}} \mathbf{F}_{\text{el}} = a_{\alpha\beta} \hat{\mathbf{a}}^\alpha \otimes \hat{\mathbf{a}}^\beta, \quad \text{and} \\ \mathbf{B}_{\text{in}}^{-1} &:= \mathbf{F}_{\text{el}}^{\text{T}} \mathbf{B}^{-1} \mathbf{F}_{\text{el}} = \mathbf{F}_{\text{in}}^{-\text{T}} \mathbf{F}_{\text{in}}^{-1} = A_{\alpha\beta} \hat{\mathbf{a}}^\alpha \otimes \hat{\mathbf{a}}^\beta. \end{aligned} \quad (12)$$

In analogy to the push forward and pull back operations in Eq. (12), the surface Green-Lagrange strain tensor \mathbf{E} can be pushed forward, or equivalently, the surface Almansi strain tensor \mathbf{e} can be pulled back to the intermediate configuration, i.e.

$$\hat{\mathbf{e}} = \mathbf{F}_{\text{in}}^{-\text{T}} \mathbf{E} \mathbf{F}_{\text{in}}^{-1} = \mathbf{F}_{\text{el}}^{\text{T}} \mathbf{e} \mathbf{F}_{\text{el}}, \quad (13)$$

which results in

$$\hat{\mathbf{e}} = \frac{1}{2}(\mathbf{C}_{\text{el}} - \mathbf{B}_{\text{in}}^{-1}) = \varepsilon_{\alpha\beta} \hat{\mathbf{a}}^\alpha \otimes \hat{\mathbf{a}}^\beta, \quad (14)$$

due to Eqs. (7), (10) and (12). Eq. (14) shows that the multiplicative split of the deformation tensor, see Eq. (6), leads to the additive split of the strains

$$\hat{\mathbf{e}} = \hat{\mathbf{e}}_{\text{el}} + \hat{\mathbf{e}}_{\text{in}}, \quad (15)$$

where

$$\hat{\mathbf{e}}_{\text{el}} = \frac{1}{2}(\mathbf{C}_{\text{el}} - \hat{\mathbf{i}}) = \varepsilon_{\alpha\beta}^{\text{el}} \hat{\mathbf{a}}^\alpha \otimes \hat{\mathbf{a}}^\beta, \quad \text{and} \quad \hat{\mathbf{e}}_{\text{in}} = \frac{1}{2}(\hat{\mathbf{i}} - \mathbf{B}_{\text{in}}^{-1}) = \varepsilon_{\alpha\beta}^{\text{in}} \hat{\mathbf{a}}^\alpha \otimes \hat{\mathbf{a}}^\beta, \quad (16)$$

with the surface identity $\hat{\mathbf{i}} = \hat{\mathbf{a}}_\alpha \otimes \hat{\mathbf{a}}^\alpha$ on $\hat{\mathcal{S}}$. The strain components in Eq. (11) are then also additively split, i.e.

$$\varepsilon_{\alpha\beta} = \varepsilon_{\alpha\beta}^{\text{el}} + \varepsilon_{\alpha\beta}^{\text{in}}, \quad (17)$$

with

$$\varepsilon_{\alpha\beta}^{\text{el}} = \frac{1}{2}(a_{\alpha\beta} - \hat{a}_{\alpha\beta}), \quad \text{and} \quad \varepsilon_{\alpha\beta}^{\text{in}} = \frac{1}{2}(\hat{a}_{\alpha\beta} - A_{\alpha\beta}). \quad (18)$$

Based on the multiplicative split of \mathbf{F} , the surface stretch in Eq. (9.2) becomes

$$J = J_{\text{el}} J_{\text{in}}, \quad (19)$$

with

$$J_{\text{el}} = \frac{\sqrt{\det[a_{\alpha\beta}]}}{\sqrt{\det[\hat{a}_{\alpha\beta}]}}}, \quad \text{and} \quad J_{\text{in}} = \frac{\sqrt{\det[\hat{a}_{\alpha\beta}]}}{\sqrt{\det[A_{\alpha\beta}]}}}. \quad (20)$$

Further, the first invariant of \mathbf{C}_{el} is given by

$$I_1^{\text{el}} = \hat{a}^{\alpha\beta} a_{\alpha\beta}. \quad (21)$$

In analogy to Eq. (17), the additive curvature decomposition

$$\kappa_{\alpha\beta} = \kappa_{\alpha\beta}^{\text{el}} + \kappa_{\alpha\beta}^{\text{in}}, \quad (22)$$

with

$$\kappa_{\alpha\beta}^{\text{el}} = b_{\alpha\beta} - \hat{b}_{\alpha\beta}, \quad \text{and} \quad \kappa_{\alpha\beta}^{\text{in}} = \hat{b}_{\alpha\beta} - B_{\alpha\beta}, \quad (23)$$

is introduced. In analogy to Eq. (5), the mean and Gaussian curvature of the intermediate surface are given by

$$\hat{H} = \frac{1}{2} \hat{a}^{\alpha\beta} \hat{b}_{\alpha\beta}, \quad \text{and} \quad \hat{\kappa} = \det[\hat{b}_{\alpha\beta}^{\alpha\beta}]. \quad (24)$$

The influences of the split of the surface deformation gradient on the surface motion, stresses, moments and balance laws are further discussed in [Sauer et al. \(2019\)](#).

2.3 Weak form

The quasi-static weak form for deforming shells is given by ([Sauer and Duong, 2017](#))

$$G_{\text{int}} - G_{\text{ext}} = 0, \quad \forall \delta \mathbf{x} \in \mathcal{U}, \quad (25)$$

with variation $\delta \mathbf{x}$ taken from some suitable space \mathcal{U} . The internal and external virtual work in Eq. (25) are given by

$$\begin{aligned} G_{\text{int}} &:= \int_{\mathcal{S}_0} \frac{1}{2} \delta a_{\alpha\beta} \tau^{\alpha\beta} \, dA + \int_{\mathcal{S}_0} \delta b_{\alpha\beta} M_0^{\alpha\beta} \, dA, \quad \text{and} \\ G_{\text{ext}} &:= \int_{\mathcal{S}} \delta \mathbf{x} \cdot \mathbf{f} \, dA + \int_{\partial \mathcal{S}} \delta \mathbf{x} \cdot \mathbf{T} \, ds + \int_{\partial \mathcal{S}} \delta \mathbf{n} \cdot \mathbf{M} \, ds, \end{aligned} \quad (26)$$

where $\delta a_{\alpha\beta}$ and $\delta b_{\alpha\beta}$ refer to the variation of the surface metric and curvature, respectively. The external forces \mathbf{f} , \mathbf{T} , and \mathbf{M} describe prescribed body forces, boundary tractions and boundary moments, respectively. The stress components $\tau^{\alpha\beta}$ and moment components $M_0^{\alpha\beta}$ in Eq. (26.1) follow from constitution, which is discussed in the subsequent section.

3 Surface constitution

This section is concerned with the constitutive relations for viscoelastic shells. Sec. 3.1 focuses on elastic materials, which is then extended to viscoelastic materials in Sec. 3.2.

3.1 Surface elasticity

For hyperelastic shells, it is advantageous to consider a decomposition of the elastic energy density into in-plane and out-of-plane contributions, i.e.

$$\Psi_{\text{el}}(a_{\alpha\beta}, b_{\alpha\beta}) = \Psi_{\text{mem}}(a_{\alpha\beta}) + \Psi_{\text{bend}}(a_{\alpha\beta}, b_{\alpha\beta}), \quad (27)$$

where Ψ_{mem} refers to the elastic energy density associated with in-plane membrane deformations, while Ψ_{bend} refers to the elastic energy density associated with out-of-plane bending. Given the elastic energy density, the membrane stress and moment components can be computed via

$$\sigma^{\alpha\beta} = \frac{2}{J} \frac{\partial \Psi_{\text{el}}}{\partial a_{\alpha\beta}}, \quad \text{and} \quad M^{\alpha\beta} = \frac{1}{J} \frac{\partial \Psi_{\text{el}}}{\partial b_{\alpha\beta}}. \quad (28)$$

The corresponding Kirchhoff stress and moment components (w.r.t. the reference configuration) follow as $\tau^{\alpha\beta} = J \sigma^{\alpha\beta}$ and $M_0^{\alpha\beta} = J M^{\alpha\beta}$. The symmetric stress $\sigma^{\alpha\beta}$ appearing in Eqs. (26.1) and (28.1) is denoted *effective stress* by [Simo and Fox \(1989\)](#). It is generally not the same as the physical (Cauchy) stress

$$N^{\alpha\beta} = \sigma^{\alpha\beta} + b_{\gamma}^{\beta} M^{\gamma\alpha}, \quad (29)$$

that appears in the equilibrium equation. Only for pure membranes or flat shells $\sigma^{\alpha\beta} = N^{\alpha\beta}$. Given $N^{\alpha\beta}$, the surface tension and the deviatoric membrane stresses are given by

$$\gamma = \frac{1}{2} N^{\alpha\beta} a_{\alpha\beta}, \quad \text{and} \quad N_{\text{dev}}^{\alpha\beta} = N^{\alpha\beta} - \gamma a^{\alpha\beta}. \quad (30)$$

In Secs. 3.1.1–3.1.7, several choices for Ψ_{mem} and Ψ_{bend} and their resulting stresses and moments are presented.

Remark 3.1: As pointed out in Remark 1.1, the employed shell formulation is based on a direct surface approach, for which the elastic energy density in Eq. (27) is an energy per surface area. Instead of providing this energy function directly, it can also be extracted from classical three-dimensional constitutive models. In that case, the 3D constitutive model is projected onto the surface via thickness integration, as

is briefly described subsequently (Duong et al., 2017). The in-plane components of the three-dimensional second Piola-Kirchhoff stress tensor $\tilde{\mathbf{S}}$ are

$$\tilde{\tau}^{\alpha\beta} = \mathbf{G}^\alpha \cdot \tilde{\mathbf{S}} \mathbf{G}^\beta, \quad (31)$$

where \mathbf{G}^α denotes the tangent vector of the shell layer at position $\mathbf{X} + \xi_0 \mathbf{N}$ (Duong et al., 2017), with thickness coordinate $\xi_0 \in [-T/2, T/2]$ and initial shell thickness T . The tensor $\tilde{\mathbf{S}}$ can then be taken from classical three-dimensional hyperelasticity and viscoelasticity models. The resulting stress and moment components of the shell then follow from the thickness integration (Duong et al., 2017)

$$\tau^{\alpha\beta} \approx \int_{-T/2}^{T/2} \tilde{\tau}^{\alpha\beta} d\xi_0, \quad \text{and} \quad M_0^{\alpha\beta} \approx - \int_{-T/2}^{T/2} \xi_0 \tilde{\tau}^{\alpha\beta} d\xi_0. \quad (32)$$

The numerical integration that is generally required here makes the projection approach less efficient than the direct surface approach.

3.1.1 Koiter membrane model

Given the membrane energy density of the Koiter model (Ciarlet, 2005; Sauer and Duong, 2017)

$$\Psi_{\text{mem}}(a_{\alpha\beta}) = \frac{1}{8} (a_{\alpha\beta} - A_{\alpha\beta}) c^{\alpha\beta\gamma\delta} (a_{\gamma\delta} - A_{\gamma\delta}), \quad (33)$$

with

$$c^{\alpha\beta\gamma\delta} = \Lambda A^{\alpha\beta} A^{\gamma\delta} + \mu (A^{\alpha\gamma} A^{\beta\delta} + A^{\alpha\delta} A^{\beta\gamma}), \quad (34)$$

the stresses follow from Eq. (28.1) as

$$\sigma^{\alpha\beta}(a_{\gamma\delta}) = \frac{1}{2J} c^{\alpha\beta\gamma\delta} (a_{\gamma\delta} - A_{\gamma\delta}) = \frac{1}{J} \left[\frac{\Lambda}{2} (I_1 - 2) a^{\alpha\beta} + \mu (A^{\alpha\gamma} a_{\gamma\delta} A^{\beta\delta} - a^{\alpha\beta}) \right]. \quad (35)$$

3.1.2 Neo-Hookean membrane model

Analogous to the classical three-dimensional Neo-Hookean material model, the Neo-Hookean membrane energy density is given by (Sauer and Duong, 2017)

$$\Psi_{\text{mem}}(a_{\alpha\beta}) = \frac{\Lambda}{4} (J^2 - 1 - 2 \ln J) + \frac{\mu}{2} (I_1 - 2 - 2 \ln J). \quad (36)$$

Its resulting stresses are

$$\sigma^{\alpha\beta}(a_{\gamma\delta}) = \frac{1}{J} \left[\frac{\Lambda}{2} (J^2 - 1) a^{\alpha\beta} + \mu (A^{\alpha\beta} - a^{\alpha\beta}) \right]. \quad (37)$$

Note that in this work, Λ may be taken as zero in Eq. (37), as it allows for an analytical solution of the evolution laws, see also Sec. 3.2.

3.1.3 Neo-Hookean membrane model with dilatational/deviatoric split

The membrane energy density in Eq. (36) does not properly split the energy into pure dilatational and deviatoric components. A proper split is achieved by the following membrane energy density (Sauer et al., 2017)

$$\Psi_{\text{mem}}(a_{\alpha\beta}) = \frac{K}{4} (J^2 - 1 - 2 \ln J) + \frac{\mu}{2} \left(\frac{I_1}{J} - 2 \right), \quad (38)$$

which yields the stresses

$$\sigma^{\alpha\beta}(a_{\gamma\delta}) = \frac{1}{J} \left[\frac{K}{2} (J^2 - 1) a^{\alpha\beta} + \frac{\mu}{2J} (2 A^{\alpha\beta} - I_1 a^{\alpha\beta}) \right]. \quad (39)$$

3.1.4 Incompressible Neo-Hookean membrane model

The classical 3D incompressible Neo-Hookean material model is described by the stress (Ogden, 1997)

$$\tilde{\boldsymbol{\sigma}} = \tilde{\mu} \tilde{\mathbf{B}} + q \mathbf{1}. \quad (40)$$

Here, $\tilde{\mu}$ denotes the 3D shear modulus and q is the Lagrange multiplier associated with the incompressibility constraint. For membranes and thin shells, $\tilde{\mathbf{B}} = \mathbf{B} + \lambda_3^2 (\mathbf{n} \otimes \mathbf{n})$ and $\tilde{\boldsymbol{\sigma}} = \boldsymbol{\sigma}/\tilde{t} + \sigma_{33} (\mathbf{n} \otimes \mathbf{n})$, where λ_3 denotes the out-of-plane stretch and \tilde{t} is the shell thickness.² Based on Eq. (40), the membrane stresses follow as (Sauer et al., 2014)

$$\sigma^{\alpha\beta}(a_{\gamma\delta}) = \frac{\mu}{J} \left(A^{\alpha\beta} - \frac{a^{\alpha\beta}}{J^2} \right). \quad (41)$$

3.1.5 Membranes with constant surface tension

A constant surface tension γ , see Eq. (30.1), can be imposed with the energy density (Sauer, 2016)

$$\Psi_{\text{mem}}(a_{\alpha\beta}) = \gamma J, \quad (42)$$

which yields the stresses

$$\sigma^{\alpha\beta}(a_{\gamma\delta}) = \gamma a^{\alpha\beta}. \quad (43)$$

3.1.6 Koiter bending model

Similar to Eq. (33), the Koiter model for bending is defined via (Ciarlet, 2005; Sauer and Duong, 2017)

$$\Psi_{\text{bend}}(b_{\alpha\beta}) = \frac{1}{2} (b_{\alpha\beta} - B_{\alpha\beta}) f^{\alpha\beta\gamma\delta} (b_{\gamma\delta} - B_{\gamma\delta}), \quad (44)$$

with for instance $f^{\alpha\beta\gamma\delta} = c/2 (A^{\alpha\gamma} A^{\beta\delta} + A^{\alpha\delta} A^{\beta\gamma})$, where c is the bending modulus. The resulting moment components follow from Eq. (28.2) as

$$M^{\alpha\beta}(b_{\gamma\delta}) = \frac{1}{J} f^{\alpha\beta\gamma\delta} (b_{\gamma\delta} - B_{\gamma\delta}). \quad (45)$$

3.1.7 Helfrich bending model

The Helfrich bending energy density is given by (Helfrich, 1973; Sauer and Duong, 2017)

$$\Psi_{\text{bend}}(a_{\alpha\beta}, b_{\alpha\beta}) = J \left(k (H - H_0)^2 + k^* \kappa \right), \quad (46)$$

which leads to the stresses

$$\sigma^{\alpha\beta}(a_{\gamma\delta}, b_{\gamma\delta}) = \left(k (H - H_0)^2 - \kappa^* \kappa \right) a^{\alpha\beta} - 2k (H - H_0) b^{\alpha\beta}, \quad (47)$$

and moment components

$$M^{\alpha\beta}(a_{\gamma\delta}, b_{\gamma\delta}) = \left(k (H - H_0) + 2k^* H \right) a^{\alpha\beta} - k^* b^{\alpha\beta}, \quad (48)$$

with material parameters k and k^* , and the so-called spontaneous curvature H_0 , which can be used to impose an initial stress-free mean curvature. Note that in this work, k^* is taken as zero in Eqs. (46)–(48).

²A tilde is placed on the current thickness to distinguish it from the time t .

3.2 Surface viscoelasticity

In order to model viscoelastic material behavior, a generalized viscoelastic solid as shown by the rheological model in Fig. 2 is considered. It is composed of one branch containing a spring

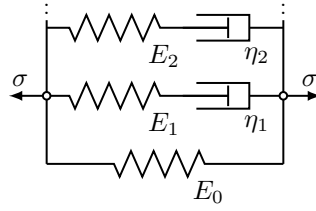


Figure 2: Surface rheology: Generalized viscoelastic solid. Here, E_{\bullet} denotes the Young's modulus of a spring element, and η_{\bullet} refers to the damping coefficient of a dashpot element.

element ('elastic branch'), and several Maxwell branches that contain a spring and dashpot element. For simplicity, here, only one Maxwell branch is considered, such that the total stresses are given by

$$\sigma^{\alpha\beta}(a^{\gamma\delta}, \hat{a}^{\gamma\delta}) = \sigma_0^{\alpha\beta}(a^{\gamma\delta}) + \sigma_1^{\alpha\beta}(\hat{a}^{\gamma\delta}), \quad (49)$$

where $\sigma_0^{\alpha\beta}$ are the stresses in the elastic branch, and $\sigma_1^{\alpha\beta}$ are the stresses in the Maxwell branch. Due to the multiplicative split of the surface deformation gradient and the resulting additive split of the strains, the strains in the spring and dashpot element of a Maxwell branch are not equal. But the stresses are equal, i.e.

$$\sigma_{1(\text{el})}^{\alpha\beta}(\hat{a}^{\gamma\delta}) = \sigma_{1(\text{in})}^{\alpha\beta}(\hat{a}^{\gamma\delta}, \dot{\hat{a}}^{\gamma\delta}). \quad (50)$$

Eq. (50) resembles three generally nonlinear ODEs for the components $\hat{a}^{\gamma\delta}$. The indices '(el)' and '(in)' refer to the spring and dashpot element of a Maxwell branch, respectively.³ Once $\hat{a}^{\gamma\delta}$ is determined, the stresses $\sigma_1^{\alpha\beta}(\hat{a}^{\gamma\delta})$ in Eq. (49) can be computed, and the total stresses $\sigma^{\alpha\beta}(a^{\gamma\delta}, \hat{a}^{\gamma\delta})$ are then used in the weak form, see Eq. (26.1).

A simple shear viscosity model for the inelastic stresses is given by (Sauer et al., 2019)

$$\sigma_{1(\text{in})}^{\alpha\beta}(\dot{\hat{a}}^{\gamma\delta}) = -\frac{1}{J_{\text{el}}} \eta_s \dot{\hat{a}}^{\alpha\beta}, \quad (51)$$

where $\eta_s \geq 0$ denotes the in-plane shear viscosity. Note that the model in Eq. (51) causes both shear and dilatation as the example in Sec. 5.1.1 shows. This is due to the fact that it leads to nonzero surface tension γ , see Eq. (30.1). Another simple viscosity model is given by (Sauer et al., 2019)

$$\sigma_{1(\text{in})}^{\alpha\beta}(\dot{\hat{a}}^{\gamma\delta}) = \frac{1}{J_{\text{el}}} \eta_s \dot{J}_{\text{in}} \hat{a}^{\alpha\beta}, \quad (52)$$

with $\eta_s \geq 0$. In general, Eq. (52) leads to nonzero shear stresses, such that the model is not purely dilatational.

In all cases, the dissipated energy can be computed via

$$\mathcal{D} = \int_0^t \int_{\mathcal{S}} \sigma_1^{\alpha\beta} \dot{\epsilon}_{\alpha\beta}^{\text{in}} da dt. \quad (53)$$

³As the elastic and inelastic stresses are equal in the Maxwell model, the indices '(el)' and '(in)' can be omitted. But they are kept here in order to emphasize that these are the stresses in the spring and dashpot elements.

Given Eq. (51) and Maxwell stresses $\sigma_{1(\text{el})}^{\alpha\beta}$, Eq. (50) can be rewritten in the form

$$\dot{\hat{a}}^{\alpha\beta} = -\frac{J_{\text{el}}}{\eta_{\text{s}}} \sigma_{1(\text{el})}^{\alpha\beta} (\hat{a}^{\gamma\delta}), \quad (54)$$

with the initial condition $\hat{a}^{\alpha\beta}|_{t=0} = A^{\alpha\beta}$. In analogy to Eq. (28.1), the Maxwell stresses $\hat{\sigma}_{1(\text{el})}^{\alpha\beta}$ follow from an energy density $\hat{\Psi}_{\text{mem}}(\hat{a}_{\alpha\beta}, a_{\alpha\beta})$, i.e.

$$\hat{\sigma}_{1(\text{el})}^{\alpha\beta} = \frac{\partial \hat{\Psi}_{\text{mem}}}{\partial \varepsilon_{\alpha\beta}^{\text{el}}} = \frac{\partial \hat{\Psi}_{\text{mem}}}{\partial \varepsilon_{\alpha\beta}}, \quad (55)$$

where the elastic energy density $\hat{\Psi}_{\text{mem}}(\hat{a}_{\alpha\beta}, a_{\alpha\beta})$ follows analogously to the membrane energy densities presented in Sec. 3.1, see also Sauer et al. (2019). The stresses $\hat{\sigma}_{1(\text{el})}^{\alpha\beta}$ can then be referred to the current surface via $\sigma_{1(\text{el})}^{\alpha\beta} = 1/J_{\text{el}} \hat{\sigma}_{1(\text{el})}^{\alpha\beta}$.

Remark 3.2: To obtain the elastic energy density $\hat{\Psi}_{\text{el}}$ from one of the energy densities Ψ_{el} presented in Sec. 3.1, the variables $A_{\alpha\beta}$ and $B_{\alpha\beta}$ need to be replaced by $\hat{a}_{\alpha\beta}$ and $\hat{b}_{\alpha\beta}$. Thus, $\hat{\Psi}_{\text{el}}$ will be dependent on $\hat{a}_{\alpha\beta}$, $\hat{b}_{\alpha\beta}$, $a_{\alpha\beta}$, and $b_{\alpha\beta}$. In contrast, Ψ_{el} is expressed in terms of $A_{\alpha\beta}$, $B_{\alpha\beta}$, $a_{\alpha\beta}$, and $b_{\alpha\beta}$.

In general, time integration schemes are needed to solve the evolution laws in Eq. (54), which are discussed in Sec. 4.4. In some special cases, however, the ODEs in Eq. (54) can be solved analytically. For instance, using the Neo-Hookean material model from Eq. (37) with $K = 0$ for the Maxwell branch, the ODEs simplify to

$$\dot{\hat{a}}^{\alpha\beta} = \frac{\mu_1}{\eta_{\text{s}}} (a^{\alpha\beta} - \hat{a}^{\alpha\beta}), \quad (56)$$

where the contravariant surface metric generally depends on time, i.e. $a^{\alpha\beta} = a^{\alpha\beta}(t)$. Eq. (56) resembles three independent, linear, first-order, inhomogeneous ODEs, which can be solved analytically for specific choices of $a^{\alpha\beta}(t)$, e.g. see the numerical examples in Secs. 5.2 and 5.4.

In analogy to Eq. (49), the total moment components for the generalized viscoelastic solid with one Maxwell branch are⁴

$$M^{\alpha\beta}(\hat{b}_{\gamma\delta}, \hat{b}_{\gamma\delta}) = M_{(0)}^{\alpha\beta}(b_{\gamma\delta}) + M_{(1)}^{\alpha\beta}(\hat{b}_{\gamma\delta}). \quad (57)$$

Similar to the stress equality condition for membrane viscosity in Eq. (50), bending viscosity requires that the moments in the spring and dashpot element of the Maxwell branch, see Fig. 2, are equal, i.e.

$$M_{(1)(\text{el})}^{\alpha\beta}(\hat{b}_{\gamma\delta}) = M_{(1)(\text{in})}^{\alpha\beta}(\hat{b}_{\gamma\delta}, \dot{\hat{b}}_{\gamma\delta}), \quad (58)$$

where ‘(1)’ refers to the *first* Maxwell branch. In analogy to Eq. (51), a simple model for the moment components in the dashpot element is (Sauer et al., 2019)

$$M_{\alpha\beta}^{(1),(\text{in})}(\dot{\hat{b}}_{\gamma\delta}) = \frac{\eta_{\text{b}}}{J_{\text{el}}} \dot{\hat{b}}_{\alpha\beta}, \quad (59)$$

with $\eta_{\text{b}} \geq 0$. Combining Eqs. (58)–(59), the evolution laws can be written as

$$\dot{\hat{b}}_{\alpha\beta} = \frac{J_{\text{el}}}{\eta_{\text{b}}} M_{\alpha\beta}^{(1)(\text{el})}(\hat{b}_{\gamma\delta}), \quad (60)$$

⁴Here, the brackets in the index are used in order to distinguish the moments in the elastic branch, $M_{(0)}^{\alpha\beta}$, from the moments components w.r.t. the reference configuration, $M_0^{\alpha\beta}$, see also Eq. (28.2).

with initial condition $\hat{b}_{\alpha\beta}|_{t=0} = B_{\alpha\beta}$. In analogy to Eq. (28.2), the Maxwell moments $\hat{M}_{1(\text{el})}^{\alpha\beta}$ follow from a bending energy density $\hat{\Psi}_{\text{bend}}(\hat{a}_{\alpha\beta}, \hat{b}_{\alpha\beta}, a_{\alpha\beta}, b_{\alpha\beta})$, i.e.

$$\hat{M}_{1(\text{el})}^{\alpha\beta} = \frac{\partial \hat{\Psi}_{\text{bend}}}{\partial \kappa_{\alpha\beta}^{\text{el}}} = \frac{\partial \hat{\Psi}_{\text{bend}}}{\partial \kappa_{\alpha\beta}}, \quad (61)$$

where a material model from Sec. 3.1 can be chosen for $\hat{\Psi}_{\text{bend}}(\hat{a}_{\alpha\beta}, \hat{b}_{\alpha\beta}, a_{\alpha\beta}, b_{\alpha\beta})$ (by replacing $A_{\alpha\beta}$ with $\hat{a}_{\alpha\beta}$ and $B_{\alpha\beta}$ with $\hat{b}_{\alpha\beta}$, see also Remark 3.2). Eq. (61) can then be referred to the current surface via $M_{1(\text{el})}^{\alpha\beta} = 1/J_{\text{el}} \hat{M}_{1(\text{el})}^{\alpha\beta}$. Note that in case of the Koiter bending model from Eq. (45), Eq. (60) leads to the evolution laws

$$\dot{\hat{b}}_{\alpha\beta} = \frac{c_1}{\eta_b} (b_{\alpha\beta} - \hat{b}_{\alpha\beta}), \quad (62)$$

which resembles three independent linear, first-order, inhomogeneous ODEs, similar to Eq. (56). For specific choices of $b_{\alpha\beta}(t)$, these ODEs are analytically solvable, e.g. see the numerical examples in Secs. 5.3–5.4. If no analytical solution is possible, numerical time integration needs to be used to solve the evolution laws, which is discussed in Sec. 4.4.

4 Computational formulation

This section briefly summarizes isogeometric surface discretizations in Sec. 4.1 and a corresponding computational formulation for modeling thin shells in Secs. 4.2–4.3, following Duong et al. (2017). Sec. 4.4 presents the numerical treatment for viscoelastic shells together with a time integration scheme for the evolution laws. The linearization within the finite element framework is discussed in Sec. 4.5 and a summary of the governing equations is provided in Sec. 4.6.

4.1 Isogeometric surface discretization

The solution of the weak form of thin shells in Eqs. (25)–(26) requires C^1 -continuous surface discretizations. Isogeometric analysis (IGA), proposed by Hughes et al. (2005), provides such surface discretizations, while offering many additional advantages. The basis functions of IGA are based on splines. Fig. 3a visualizes these spline basis functions for cubic order ($p = 3$) and knot vector $\Xi = [0, 0, 0, 0, 0.25, 0.5, 0.75, 1, 1, 1, 1]$. Each basis function spans over $p+1$ elements, which is different from standard finite element methods based on Lagrangian basis functions.

For two parametric directions, as required for the surface description presented in Sec. 2.1, the basis functions follow from the tensor product of the basis functions in each parametric dimension. In order to embed isogeometric analysis into a standard finite element code, the Bézier extraction operator of Borden et al. (2011) can be used. For a given element Ω^e , there are n spline basis functions that have support on Ω^e , i.e. that are non-vanishing on this element. The NURBS (Non-Uniform Rational B-Splines) basis functions $\{N_A\}_{A=1}^n$ on Ω^e at the parametric coordinate (ξ, η) are given by

$$N_A(\xi, \eta) = \frac{w_A \hat{N}_A(\xi, \eta)}{\sum_{\tilde{A}=1}^n w_{\tilde{A}} \hat{N}_{\tilde{A}}(\xi, \eta)}, \quad (63)$$

with weights w_A and B-spline basis functions $\{\hat{N}_A\}_{A=1}^n$. This B-spline basis is mapped to a Bézier basis, which does not span over multiple elements. Cubic Bézier polynomials $B_{i,p}$

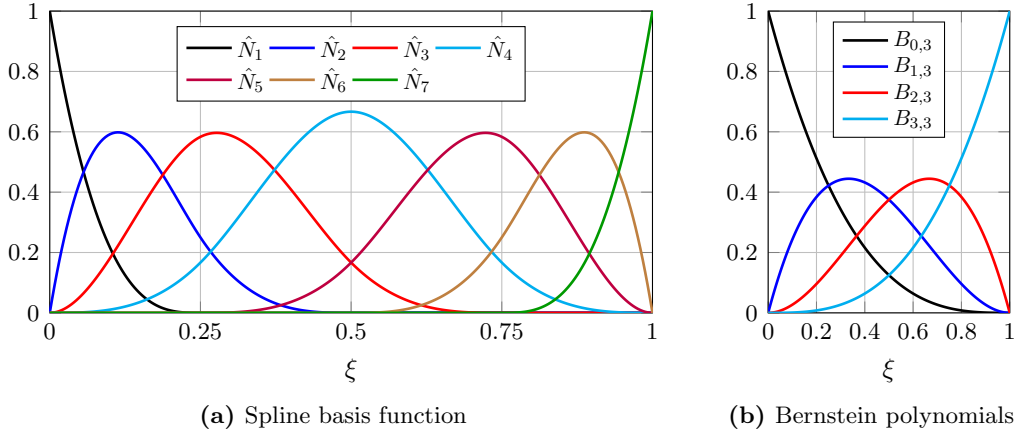


Figure 3: Isogeometric discretization: (a) Cubic spline basis functions \hat{N}_A for the knot vector $\Xi = [0, 0, 0, 0, 0.25, 0.5, 0.75, 1, 1, 1, 1]$ and (b) cubic Bernstein polynomials $B_{i,p}$ ($i = 0, \dots, p$).

($i = 0, \dots, p$) are illustrated in Fig. 3b. Considering the Bézier extraction operators \mathbf{C}_ξ^e and \mathbf{C}_η^e for element Ω^e in ξ - and η -direction, respectively, yields the B-spline basis functions

$$\hat{\mathbf{N}}^e(\xi, \eta) = \mathbf{C}_\xi^e \mathbf{B}(\xi) \otimes \mathbf{C}_\eta^e \mathbf{B}(\eta). \quad (64)$$

In Eq. (64), $\hat{\mathbf{N}}^e$ is of size $n \times 1$ and contains the basis functions \hat{N}_A , $A = 1, \dots, n$. The Bézier extraction operators are of size $n \times n$, and \mathbf{B} is of size $n \times 1$ and contains the Bernstein polynomials in the corresponding parametric direction. Note that instead of Bézier extraction, also Lagrange extraction can be used (Schillinger et al., 2016).

4.2 Discretization of the primary field

Given are the n_e spline basis functions on parametric element Ω^e with global indices i_1, \dots, i_{n_e} . The surface representation is then given by

$$\mathbf{X} \approx \mathbf{X}^h = \mathbf{N}^e \mathbf{X}_e, \quad \text{and} \quad \mathbf{x} \approx \mathbf{x}^h = \mathbf{N}^e \mathbf{x}_e, \quad (65)$$

for the reference and current surface, respectively. Here, the shape function array is

$$\mathbf{N}^e := [N_{i_1} \mathbf{1}, N_{i_2} \mathbf{1}, \dots, N_{i_{n_e}} \mathbf{1}], \quad (66)$$

with dimension $3 \times 3n_e$. The (3×3) -identity matrix is denoted $\mathbf{1}$ and the element-level vectors for the nodal displacements are denoted \mathbf{X}_e and \mathbf{x}_e . Analogously to Eq. (65), the variations of the nodal displacements on element Ω^e are

$$\delta \mathbf{X}^h = \mathbf{N}^e \delta \mathbf{X}_e, \quad \text{and} \quad \delta \mathbf{x}^h = \mathbf{N}^e \delta \mathbf{x}_e. \quad (67)$$

The discretized covariant tangent vectors, see also Eq. (1.1), follow as

$$\mathbf{A}_\alpha^h = \mathbf{N}_{,\alpha}^e \mathbf{X}_e, \quad \text{and} \quad \mathbf{a}_\alpha^h = \mathbf{N}_{,\alpha}^e \mathbf{x}_e, \quad (68)$$

with $\mathbf{N}_{,\alpha}^e = \partial \mathbf{N}^e / \partial \xi^\alpha$. The discretized surface normals \mathbf{N}^h and \mathbf{n}^h follow in analogy to Eq. (1.2). The metric and curvature tensor components are then given by

$$A_{\alpha\beta}^h = \mathbf{X}_e^T (\mathbf{N}_{,\alpha}^e)^T \mathbf{N}_{,\beta}^e \mathbf{X}_e, \quad \text{and} \quad B_{\alpha\beta}^h = \mathbf{N}^h \cdot \mathbf{N}_{,\alpha\beta}^e \mathbf{X}_e, \quad (69)$$

and

$$a_{\alpha\beta}^h = \mathbf{x}_e^T (\mathbf{N}_{,\alpha}^e)^T \mathbf{N}_{,\beta}^e \mathbf{x}_e, \quad \text{and} \quad b_{\alpha\beta}^h = \mathbf{n}^h \cdot \mathbf{N}_{,\alpha\beta}^e \mathbf{x}_e. \quad (70)$$

Eqs. (69)–(70) can then be used to compute the discretized contravariant surface metrics, $[A_h^{\alpha\beta}] = [A_{\alpha\beta}^h]^{-1}$ and $[a_h^{\alpha\beta}] = [a_{\alpha\beta}^h]^{-1}$. In analogy, the discretized variations of the surface metric and curvature are given by

$$\delta a_{\alpha\beta}^h = \delta \mathbf{x}_e^T \left((\mathbf{N}_{,\alpha}^e)^T \mathbf{N}_{,\beta}^e + (\mathbf{N}_{,\beta}^e)^T \mathbf{N}_{,\alpha}^e \right) \mathbf{x}_e, \quad \text{and} \quad \delta b_{\alpha\beta}^h = \delta \mathbf{x}_e^T (\mathbf{N}_{,\alpha\beta}^e)^T \mathbf{n}^h, \quad (71)$$

with

$$\mathbf{N}_{,\alpha\beta}^e := \mathbf{N}_{,\alpha\beta}^e - \Gamma_{\alpha\beta}^\gamma \mathbf{N}_{,\gamma}^e. \quad (72)$$

Here, the discretized Christoffel symbols of the second kind on \mathcal{S} are

$$\Gamma_{\alpha\beta}^\gamma = \mathbf{x}_e^T (\mathbf{N}_{,\alpha\beta}^e)^T a_h^{\gamma\delta} \mathbf{N}_{,\delta}^e \mathbf{x}_e. \quad (73)$$

Note that subsequently, the superscript ‘h’ may be omitted for notational simplicity.

Since the evolution laws for membrane and bending viscosity, see Eqs. (54) and (60), are purely temporal, no spatial discretization is required for $\hat{a}^{\alpha\beta}$ and $\hat{b}_{\alpha\beta}$. Thus, $\hat{a}^{\alpha\beta}$ and $\hat{b}_{\alpha\beta}$ can be treated as history variables that are evolved and stored at each quadrature point. This effectively eliminates them from the set of unknowns leading to a dependency of $\hat{a}^{\alpha\beta}$ and $\hat{b}_{\alpha\beta}$ on the primary unknown \mathbf{x} that affects the linearization, see also Sec. 4.5.

4.3 Discretized mechanical weak form

Inserting the discretization from above into Eqs. (25)–(26) yields the discretized mechanical weak form

$$\delta \mathbf{x}^T [\mathbf{f}_{\text{int}} - \mathbf{f}_{\text{ext}}] = 0, \quad \forall \delta \mathbf{x} \in \mathcal{U}^h, \quad (74)$$

with the finite-dimensional space $\mathcal{U}^h \subset \mathcal{U}$, and the global force vectors \mathbf{f}_{int} and \mathbf{f}_{ext} . These are assembled from their element-level contributions

$$\begin{aligned} \mathbf{f}_{\text{int}}^e &:= \int_{\Omega^e} \sigma^{\alpha\beta} (\mathbf{N}_{,\alpha}^e)^T \mathbf{a}_\beta^h da + \int_{\Omega^e} M^{\alpha\beta} (\mathbf{N}_{,\alpha\beta}^e)^T \mathbf{n}^h da, \quad \text{and} \\ \mathbf{f}_{\text{ext}}^e &:= \int_{\Omega^e} (\mathbf{N}^e)^T p \mathbf{n}^h da + \int_{\Omega^e} (\mathbf{N}^e)^T f^\alpha \mathbf{a}_\alpha^h da, \end{aligned} \quad (75)$$

where Ω^e denotes the domain of element e in the current configuration. In $\mathbf{f}_{\text{ext}}^e$, the boundary loads \mathbf{T} and \mathbf{M} acting on $\partial\mathcal{S}$ are assumed to be zero. The extension to boundary loads can be found in [Duong et al. \(2017\)](#). The computation of the stresses $\sigma^{\alpha\beta}$ and moments $M^{\alpha\beta}$ is outlined in Sec. 3.

From Eq. (74) follows the equation of motion at the free nodes (where no Dirichlet boundary conditions are prescribed)

$$\mathbf{f}(\mathbf{x}) = \mathbf{f}_{\text{int}}(\mathbf{x}) - \mathbf{f}_{\text{ext}}(\mathbf{x}) = \mathbf{0}, \quad (76)$$

where \mathbf{x} is the global unknown, similar to the element-level unknowns \mathbf{x}_e .

4.4 Solution of the evolution laws

In Sec. 3, ODEs for $\hat{a}^{\alpha\beta}$ and $\hat{b}_{\alpha\beta}$ are derived, see Eqs. (54) and (60). In general, they need to be solved numerically as no analytical solution exists. The temporal integration of $\hat{a}^{\alpha\beta}$ based on Eq. (54) is described in Sec. 4.4.1, and the numerical treatment of $\hat{b}_{\alpha\beta}$ is described in Sec. 4.4.2.

4.4.1 Membrane material models

Given all quantities at time step n and the time step size $\Delta t_{n+1} := t_{n+1} - t_n$, Eq. (54) needs to be solved for $\hat{a}_{n+1}^{\alpha\beta}$. Here, an implicit/backward Euler method is employed, such that the ODEs in Eq. (54) reduce to the nonlinear algebraic equations

$$\hat{\mathbf{g}}_s^{\alpha\beta}(\hat{a}_{n+1}^{\gamma\delta}) := \frac{\hat{a}_{n+1}^{\alpha\beta} - \hat{a}_n^{\alpha\beta}}{\Delta t_{n+1}} + \frac{J_{\text{el},n+1}}{\eta_s} \sigma_{1(\text{el})}^{\alpha\beta}(\hat{a}_{n+1}^{\gamma\delta}) = 0, \quad (77)$$

which need to be solved for $\hat{a}_{n+1}^{\alpha\beta}$. The initial condition is $\hat{a}_{n+1}^{\alpha\beta}|_{t=0} = A^{\alpha\beta}$. Eq. (77) contains four equations, which need to be solved for the four unknowns $\hat{a}_{n+1}^{\alpha\beta}$. As $\hat{a}^{12} = \hat{a}^{21}$, the unknown \hat{a}^{21} and the corresponding equation $\hat{\mathbf{g}}_s^{21} = 0$ can be eliminated. Thus, there remain three equations and unknowns, which are arranged in the vectors

$$\hat{\mathbf{g}}_s := \begin{bmatrix} \hat{\mathbf{g}}_s^{11} \\ \hat{\mathbf{g}}_s^{12} \\ \hat{\mathbf{g}}_s^{22} \end{bmatrix} = \mathbf{0}, \quad \text{and} \quad \hat{\mathbf{a}} := \begin{bmatrix} \hat{a}^{11} \\ \hat{a}^{12} \\ \hat{a}^{22} \end{bmatrix}. \quad (78)$$

In general, it is not possible to solve Eq. (78.1) analytically, and thus a local Newton-Raphson iteration is used. Using Taylor expansion, Eq. (78.1) is approximated around $\hat{\mathbf{a}}_{n+1}|_i$ (where i denotes the i 'th Newton-Raphson step) by

$$\hat{\mathbf{g}}_s|_{i+1} \approx \hat{\mathbf{g}}_s|_i + \frac{\partial \hat{\mathbf{g}}_s}{\partial \hat{\mathbf{a}}_{n+1}} \Big|_i \Delta \hat{\mathbf{a}}_{n+1}|_{i+1} = \mathbf{0}, \quad (79)$$

where

$$\frac{\partial \hat{\mathbf{g}}_s}{\partial \hat{\mathbf{a}}_{n+1}} = \begin{bmatrix} \partial \hat{\mathbf{g}}_s^{11} / \partial \hat{a}_{n+1}^{11} & \partial \hat{\mathbf{g}}_s^{11} / \partial \hat{a}_{n+1}^{12} + \partial \hat{\mathbf{g}}_s^{11} / \partial \hat{a}_{n+1}^{21} & \partial \hat{\mathbf{g}}_s^{11} / \partial \hat{a}_{n+1}^{22} \\ \partial \hat{\mathbf{g}}_s^{12} / \partial \hat{a}_{n+1}^{11} & \partial \hat{\mathbf{g}}_s^{12} / \partial \hat{a}_{n+1}^{12} + \partial \hat{\mathbf{g}}_s^{12} / \partial \hat{a}_{n+1}^{21} & \partial \hat{\mathbf{g}}_s^{12} / \partial \hat{a}_{n+1}^{22} \\ \partial \hat{\mathbf{g}}_s^{22} / \partial \hat{a}_{n+1}^{11} & \partial \hat{\mathbf{g}}_s^{22} / \partial \hat{a}_{n+1}^{12} + \partial \hat{\mathbf{g}}_s^{22} / \partial \hat{a}_{n+1}^{21} & \partial \hat{\mathbf{g}}_s^{22} / \partial \hat{a}_{n+1}^{22} \end{bmatrix}. \quad (80)$$

Note that the sum in the second column of Eq. (80) occurs because the variable \hat{a}^{21} is eliminated, as mentioned above. Provided the starting guess $\hat{\mathbf{a}}_{n+1}|_0 = \hat{\mathbf{a}}_n$, the iteration ($i = 0, 1, 2, \dots$)

$$\text{solve} \quad \frac{\partial \hat{\mathbf{g}}_s(\hat{\mathbf{a}}_{n+1})}{\partial \hat{\mathbf{a}}_{n+1}} \Big|_i \Delta \hat{\mathbf{a}}_{n+1}|_{i+1} = -\hat{\mathbf{g}}_s(\hat{\mathbf{a}}_{n+1})|_i \quad \text{for} \quad \Delta \hat{\mathbf{a}}_{n+1}|_{i+1}, \quad (81)$$

$$\text{update} \quad \hat{\mathbf{a}}_{n+1}|_{i+1} = \hat{\mathbf{a}}_{n+1}|_i + \Delta \hat{\mathbf{a}}_{n+1}|_{i+1},$$

is repeated until convergence is obtained. Convergence is monitored by checking if

$$\left\| \Delta \hat{\mathbf{a}}_{n+1}|_{i+1} \right\|_2 \leq 10^{-10}. \quad (82)$$

Subsequently, the algebraic equations following from Eq. (77) are specified for all the membrane material models of Sec. 3. The index ' $n+1$ ' is omitted for notational simplicity in the subsequent sections. Every quantity without index ' n ' is evaluated at the current time step.

4.4.1.1 Koiter membrane model

Given the material model from Eq. (33),⁵ Eq. (77) becomes

$$\hat{\mathbf{g}}_s^{\alpha\beta}(\hat{a}^{\gamma\delta}) = \frac{\hat{a}^{\alpha\beta} - \hat{a}_n^{\alpha\beta}}{\Delta t} + \frac{\Lambda_1}{2\eta_s} (I_1^{\text{el}} - 2) \hat{a}^{\alpha\beta} + \frac{\mu_1}{\eta_s} (\hat{a}^{\alpha\gamma} a_{\gamma\delta} \hat{a}^{\beta\delta} - \hat{a}^{\alpha\beta}) = 0. \quad (83)$$

⁵with $A_{\alpha\beta}$ replaced by $\hat{a}_{\alpha\beta}$, see also Remark 3.2

4.4.1.2 Neo-Hookean membrane model

Considering the material model from Eq. (36) with $\Lambda = 0$,⁵ Eq. (77) becomes

$$\hat{g}_s^{\alpha\beta}(\hat{a}^{\gamma\delta}) = \frac{\hat{a}^{\alpha\beta} - \hat{a}_n^{\alpha\beta}}{\Delta t} + \frac{\mu_1}{\eta_s} (\hat{a}^{\alpha\beta} - a^{\alpha\beta}) = 0. \quad (84)$$

This is a linear model that can be solved directly for $\hat{a}^{\alpha\beta}$ (without using Eq. (81)) giving

$$\hat{a}^{\alpha\beta} = \frac{\eta_s \hat{a}_n^{\alpha\beta} + \mu_1 \Delta t a^{\alpha\beta}}{\eta_s + \mu_1 \Delta t}. \quad (85)$$

4.4.1.3 Neo-Hookean membrane model with dilatational/deviatoric split

For the material model from Eq. (38),⁵ Eq. (77) becomes

$$\hat{g}_s^{\alpha\beta}(\hat{a}^{\gamma\delta}) = \frac{\hat{a}^{\alpha\beta} - \hat{a}_n^{\alpha\beta}}{\Delta t} + \frac{K_1}{2\eta_s} (J_{\text{el}}^2 - 1) a^{\alpha\beta} + \frac{\mu_1}{2\eta_s J_{\text{el}}} (2\hat{a}^{\alpha\beta} - I_1^{\text{el}} a^{\alpha\beta}) = 0. \quad (86)$$

4.4.1.4 Incompressible Neo-Hookean membrane model

For the material model from Eq. (41),⁵ Eq. (77) becomes

$$\hat{g}_s^{\alpha\beta}(\hat{a}^{\gamma\delta}) = \frac{\hat{a}^{\alpha\beta} - \hat{a}_n^{\alpha\beta}}{\Delta t} + \frac{\mu_1}{\eta_s} \left(\hat{a}^{\alpha\beta} - \frac{a^{\alpha\beta}}{J_{\text{el}}^2} \right) = 0. \quad (87)$$

4.4.1.5 Membranes with constant surface tension

Considering the material model from Eq. (42),⁵ Eq. (77) becomes

$$\hat{g}_s^{\alpha\beta}(\hat{a}^{\gamma\delta}) = \frac{\hat{a}^{\alpha\beta} - \hat{a}_n^{\alpha\beta}}{\Delta t} + \frac{\hat{\gamma}}{\eta_s} J_{\text{el}} a^{\alpha\beta} = 0, \quad (88)$$

where $\hat{\gamma}$ denotes the prescribed surface tension w.r.t. the intermediate configuration.

4.4.2 Bending material models

The numerical time integration of the evolution laws for bending viscosity follows in analogy to the presented scheme for the evolution laws for membrane viscosity. In analogy to Eq. (77), the ODEs in Eq. (60) reduce to the nonlinear algebraic equations

$$\hat{g}_{\alpha\beta}^{\text{b}}(\hat{b}_{\gamma\delta}) := \frac{\hat{b}_{\alpha\beta} - \hat{b}_{\alpha\beta}^n}{\Delta t} - \frac{J_{\text{el}}}{\eta_{\text{b}}} M_{\alpha\beta}^{(1)(\text{el})}(\hat{b}_{\gamma\delta}) = 0, \quad (89)$$

with initial condition $\hat{b}_{\alpha\beta}|_{t=0} = B_{\alpha\beta}$.

4.4.2.1 Koiter bending model

The algebraic equations, see Eq. (89),⁶ for the material model from Eq. (44) become

$$\hat{\mathbf{g}}_{\alpha\beta}^{\text{b}}(\hat{b}_{\gamma\delta}) = \frac{\hat{b}_{\alpha\beta} - \hat{b}_{\alpha\beta}^n}{\Delta t} + \frac{c_1}{\eta_{\text{b}}} (\hat{b}_{\alpha\beta} - b_{\alpha\beta}) = 0. \quad (90)$$

This is also a linear model that can be directly solved for $\hat{b}_{\alpha\beta}$, similar to Eq. (85).

4.4.2.2 Helfrich bending model

For the material model from Eq. (46) with $k^* = 0$,^{5,6} Eqs. (77) and (89) become

$$\hat{\mathbf{g}}_{\text{s}}^{\alpha\beta}(\hat{a}^{\gamma\delta}) = \frac{\hat{a}^{\alpha\beta} - \hat{a}_n^{\alpha\beta}}{\Delta t} + \frac{k_1 J_{\text{el}}}{\eta_{\text{b}}} \left[(H - \hat{H})^2 a^{\alpha\beta} - 2(H - \hat{H}) b^{\alpha\beta} \right] = 0, \quad (91)$$

and

$$\hat{\mathbf{g}}_{\alpha\beta}^{\text{b}}(\hat{b}_{\gamma\delta}) = \frac{\hat{b}_{\alpha\beta} - \hat{b}_{\alpha\beta}^n}{\Delta t} - \frac{k_1 J_{\text{el}}}{\eta_{\text{b}}} (H - \hat{H}) a_{\alpha\beta} = 0. \quad (92)$$

The derivatives of all these material models, which are required in Eq. (80), are reported in Appendix A.2.

Remark 4.1: For coupled membrane and bending viscosity, iteration (81) has to be performed for the unknowns $\hat{a}^{\alpha\beta}$ and $\hat{b}_{\alpha\beta}$ simultaneously. The linear equation system in Eq. (81.1) then becomes

$$\begin{bmatrix} \partial \hat{\mathbf{g}}_{\text{s}}(\hat{\mathbf{a}}_{n+1}, \hat{\mathbf{b}}_{n+1}) / \partial \hat{\mathbf{a}}_{n+1} & \partial \hat{\mathbf{g}}_{\text{s}}(\hat{\mathbf{a}}_{n+1}, \hat{\mathbf{b}}_{n+1}) / \partial \hat{\mathbf{b}}_{n+1} \\ \partial \hat{\mathbf{g}}^{\text{b}}(\hat{\mathbf{a}}_{n+1}, \hat{\mathbf{b}}_{n+1}) / \partial \hat{\mathbf{a}}_{n+1} & \partial \hat{\mathbf{g}}^{\text{b}}(\hat{\mathbf{a}}_{n+1}, \hat{\mathbf{b}}_{n+1}) / \partial \hat{\mathbf{b}}_{n+1} \end{bmatrix}_i \begin{bmatrix} \Delta \hat{\mathbf{a}}_{n+1} \\ \Delta \hat{\mathbf{b}}_{n+1} \end{bmatrix}_{i+1} = - \begin{bmatrix} \hat{\mathbf{g}}_{\text{s}}(\hat{\mathbf{a}}_{n+1}, \hat{\mathbf{b}}_{n+1}) \\ \hat{\mathbf{g}}_{\text{b}}(\hat{\mathbf{a}}_{n+1}, \hat{\mathbf{b}}_{n+1}) \end{bmatrix}_i, \quad (93)$$

where the vector $\hat{\mathbf{b}}$ arranges the terms $\hat{b}_{\alpha\beta}$ analogously to Eq. (78.2). For example, the discretized evolution laws for the Helfrich model, see Eqs. (91)–(92), lead to coupled membrane and bending viscosity, see also Eqs. (133)–(134).

Remark 4.2: Examining Eq. (85) shows that the absolute value of the factor in front of $\hat{a}_n^{\alpha\beta}$ is $\eta_{\text{s}} / (\eta_{\text{s}} + \mu_1 \Delta t)$, which is smaller to one and thus, the method is stable. For the explicit Euler scheme, this factor would be $|(\eta_{\text{s}} - \mu_1 \Delta t) / \eta_{\text{s}}|$, which might become larger to one, such that the method is not stable. Thus, the implicit Euler scheme is used in this work.

Remark 4.3: The presented formulation of membrane viscosity leads to ODEs for the intermediate surface metric $\hat{a}^{\alpha\beta}$. For some discretizations, e.g. based on unstructured splines, solving for $\hat{a}^{\alpha\beta}$ might lead to numerical ill-conditioning. For instance, at the extraordinary points of an unstructured spline sphere (Toshniwal et al., 2017), the parametrization becomes singular, i.e. one tangent vector \mathbf{a}_{α} approaches $\mathbf{0}$. The computation of the inverse $[a^{\alpha\beta}] = [a_{\alpha\beta}]^{-1}$ then might lead to numerical ill-conditioning. The same problem pertains to the intermediate surface metric $\hat{a}^{\alpha\beta}$. In order to resolve this issue, the ODEs for $\hat{a}^{\alpha\beta}$ may be reformulated, e.g. as ODEs for I_1^{el} , J_{in} and J_{el} , but also other options could be possible, for instance based on the Cauchy-Green tensor \mathbf{C}_{el} .

4.5 Solution of the nonlinear equation system

The nonlinear equation system in Eq. (76) is solved using a global Newton-Raphson iteration. This scheme requires the linearization of the force vector in Eq. (76). This leads to the element-level stiffness matrix $\mathbf{k}^e := \mathbf{k}_{\tau\tau}^e + \mathbf{k}_{\tau M}^e + \mathbf{k}_{M\tau}^e + \mathbf{k}_{MM}^e + \mathbf{k}_{\tau}^e + \mathbf{k}_M^e$ with the element-level material

⁶with $B_{\alpha\beta}$ replaced by $\hat{b}_{\alpha\beta}$, see also Remark 3.2

stiffness matrices

$$\begin{aligned} \mathbf{k}_{\tau\tau}^e &:= \int_{\Omega_0^e} c^{\alpha\beta\gamma\delta} (\mathbf{N}_{;\alpha}^e)^\top (\mathbf{a}_\beta \otimes \mathbf{a}_\gamma) \mathbf{N}_{;\delta}^e dA, & \mathbf{k}_{\tau M}^e &:= \int_{\Omega_0^e} d^{\alpha\beta\gamma\delta} (\mathbf{N}_{;\alpha}^e)^\top (\mathbf{a}_\beta \otimes \mathbf{n}) \mathbf{N}_{;\gamma\delta}^e dA, \\ \mathbf{k}_{M\tau}^e &:= \int_{\Omega_0^e} e^{\alpha\beta\gamma\delta} (\mathbf{N}_{;\alpha\beta}^e)^\top (\mathbf{n} \otimes \mathbf{a}_\gamma) \mathbf{N}_{;\delta}^e dA, & \mathbf{k}_{MM}^e &:= \int_{\Omega_0^e} f^{\alpha\beta\gamma\delta} (\mathbf{N}_{;\alpha\beta}^e)^\top (\mathbf{n} \otimes \mathbf{n}) \mathbf{N}_{;\gamma\delta}^e dA, \end{aligned} \quad (94)$$

and the element-level geometric stiffness matrices

$$\mathbf{k}_\tau^e := \int_{\Omega_0^e} (\mathbf{N}_{;\alpha}^e)^\top \tau^{\alpha\beta} \mathbf{N}_{;\beta}^e dA, \quad \text{and} \quad \mathbf{k}_M^e := \mathbf{k}_{M1}^e + \mathbf{k}_{M2}^e + (\mathbf{k}_{M2}^e)^\top, \quad (95)$$

with

$$\begin{aligned} \mathbf{k}_{M1}^e &:= - \int_{\Omega_0^e} b_{\alpha\beta} M_0^{\alpha\beta} a^{\gamma\delta} (\mathbf{N}_{;\gamma}^e)^\top (\mathbf{n} \otimes \mathbf{n}) \mathbf{N}_{;\delta}^e dA, \quad \text{and} \\ \mathbf{k}_{M2}^e &:= - \int_{\Omega_0^e} M_0^{\alpha\beta} (\mathbf{N}_{;\gamma}^e)^\top (\mathbf{n} \otimes \mathbf{a}^\gamma) \mathbf{N}_{;\alpha\beta}^e dA, \end{aligned} \quad (96)$$

see [Duong et al. \(2017\)](#) for more details and for the linearization of the external element-level force vector $\mathbf{f}_{\text{ext}}^e$ in Eq. (75.2). In Eq. (94), the material tangents

$$c^{\alpha\beta\gamma\delta} = 2 \frac{\partial \tau^{\alpha\beta}}{\partial a_{\gamma\delta}}, \quad d^{\alpha\beta\gamma\delta} = \frac{\partial \tau^{\alpha\beta}}{\partial b_{\gamma\delta}}, \quad e^{\alpha\beta\gamma\delta} = 2 \frac{\partial M_0^{\alpha\beta}}{\partial a_{\gamma\delta}}, \quad \text{and} \quad f^{\alpha\beta\gamma\delta} = \frac{\partial M_0^{\alpha\beta}}{\partial b_{\gamma\delta}}, \quad (97)$$

need to be defined for the employed material model. As the stresses and moments are composed of elastic and Maxwell components, see Eqs. (49) and (57), the material tangents in Eq. (97) will also be composed of the two contributions

$$\tilde{c}^{\alpha\beta\gamma\delta} = \tilde{c}_0^{\alpha\beta\gamma\delta} + \tilde{c}_1^{\alpha\beta\gamma\delta}, \quad \tilde{c} = c, d, e, f, \quad (98)$$

where again the index ‘0’ refers to the elastic branch and ‘1’ refers to the Maxwell branch. The Maxwell material tangents $\tilde{c}_1^{\alpha\beta\gamma\delta}$ in Eq. (98) are derived in [Appendix A.3](#).

Remark 4.4: In [Sauer et al. \(2019\)](#), the variables $\hat{a}_{\alpha\beta}$ and $\hat{b}_{\alpha\beta}$ are assumed to be independent variables from $a_{\alpha\beta}$ and $b_{\alpha\beta}$. In this work here, the unknowns $\hat{a}_{\alpha\beta}$ and $\hat{b}_{\alpha\beta}$ are locally eliminated by solving Eqs. (54) and (60) at each quadrature point, see [Sec. 4.4](#). This elimination makes $\hat{a}_{\alpha\beta}$ and $\hat{b}_{\alpha\beta}$ a function of $a_{\alpha\beta}$ and $b_{\alpha\beta}$, which leads to additional derivatives in the linearization that are not appearing in the theory of [Sauer et al. \(2019\)](#).

4.6 Summary of the computational formulation for viscoelastic shells

A concise summary of the presented computational formulation for viscoelastic shells is given in [Table 1](#).

5 Numerical examples

This section presents several numerical examples that illustrate viscoelastic behavior of shells. In [Sec. 5.1](#), typical viscoelastic behavior is investigated on two-dimensional square membranes. The implementation of membrane, bending, and coupled membrane and bending viscosity is then verified in [Secs. 5.2–5.4](#). In [Sec. 5.5](#), a viscoelastic Scordelis-Lo roof is investigated to illustrate inhomogeneous deformations. [Sec. 5.6](#) shows that the presented formulation is also capable of modeling boundary viscoelasticity of 3D bodies. For all examples in this section, the

Table 1: Summary of the computational formulation for viscoelastic shells

<p>The governing nonlinear equation system for the shell deformation is</p> $\mathbf{f}(\mathbf{x}) = \mathbf{f}_{\text{int}}(\mathbf{x}) - \mathbf{f}_{\text{ext}}(\mathbf{x}) = \mathbf{0},$ <p>which is assembled from the element-level contributions</p> $\mathbf{f}_{\text{int}}^e := \int_{\Omega^e} \sigma^{\alpha\beta} \mathbf{N}_{,\alpha}^T \mathbf{a}_{\beta}^h da + \int_{\Omega^e} M^{\alpha\beta} \mathbf{N}_{;\alpha\beta}^T \mathbf{n}^h da, \quad \text{and}$ $\mathbf{f}_{\text{ext}}^e := \int_{\Omega^e} \mathbf{N}^T p \mathbf{n}^h da + \int_{\Omega^e} \mathbf{N}^T f^\alpha \mathbf{a}_{\alpha}^h da.$ <p>The stresses and moments (considering one Maxwell branch) are given by</p> $\sigma^{\alpha\beta} = \sigma_0^{\alpha\beta} (a^{\gamma\delta}) + \sigma_1^{\alpha\beta} (\hat{a}^{\gamma\delta}), \quad \text{and} \quad M^{\alpha\beta} = M_{(0)}^{\alpha\beta} (b^{\gamma\delta}) + M_{(1)}^{\alpha\beta} (\hat{b}^{\gamma\delta}).$ <p>Here, $\sigma_0^{\alpha\beta}$, $\sigma_1^{\alpha\beta} = \sigma_{1(\text{el})}^{\alpha\beta}$, $M_{(0)}^{\alpha\beta}$, and $M_{(1)}^{\alpha\beta} = M_{(1)(\text{el})}^{\alpha\beta}$ follow from a specific choice of the elastic energy density, see Sec. 3.1 for examples. The Maxwell stress $\sigma_1^{\alpha\beta}$ and moment $M_{(1)}^{\alpha\beta}$ follow from the conditions in Eqs. (50) and (58). For the simple shear viscosity models in Eqs. (51) and (59), the evolution laws for $\hat{a}^{\alpha\beta}$ and $\hat{b}_{\alpha\beta}$ are given by</p> $\dot{\hat{a}}^{\alpha\beta} = -\frac{J_{\text{el}}}{\eta_s} \sigma_{1(\text{el})}^{\alpha\beta} (\hat{a}^{\gamma\delta}), \quad \text{and} \quad \dot{\hat{b}}_{\alpha\beta} = \frac{J_{\text{el}}}{\eta_b} M_{\alpha\beta}^{(1)(\text{el})} (\hat{b}_{\gamma\delta}),$ <p>with initial conditions $\hat{a}^{\alpha\beta} _{t=0} = A^{\alpha\beta}$ and $\hat{b}_{\alpha\beta} _{t=0} = B_{\alpha\beta}$. The resulting ODEs are solved with the implicit Euler scheme, which leads to the temporal discretized nonlinear equations</p> $\hat{\mathbf{g}}_s^{\alpha\beta} (\hat{a}^{\gamma\delta}) := \frac{\hat{a}^{\alpha\beta} - \hat{a}_n^{\alpha\beta}}{\Delta t} + \frac{J_{\text{el}}}{\eta_s} \sigma_{1(\text{el})}^{\alpha\beta} (\hat{a}^{\gamma\delta}) = 0, \quad \text{and}$ $\hat{\mathbf{g}}_{\alpha\beta}^b (\hat{b}_{\gamma\delta}) := \frac{\hat{b}_{\alpha\beta} - \hat{b}_{\alpha\beta}^n}{\Delta t} - \frac{J_{\text{el}}}{\eta_b} M_{\alpha\beta}^{(1)(\text{el})} (\hat{b}_{\gamma\delta}) = 0,$ <p>which are solved with a local Newton-Raphson method, see Eq. (81). To solve $\mathbf{f}(\mathbf{x}) = \mathbf{0}$, a global Newton-Raphson method is employed. The required stiffness matrix is</p> $\mathbf{k}^e := \mathbf{k}_{\tau\tau}^e + \mathbf{k}_{\tau M}^e + \mathbf{k}_{M\tau}^e + \mathbf{k}_{MM}^e + \mathbf{k}_{\tau}^e + \mathbf{k}_M^e,$ <p>with the individual terms given in Eqs. (94)–(96). The material tangents in the material stiffness matrices are computed from</p> $\tilde{c}^{\alpha\beta\gamma\delta} = \tilde{c}_0^{\alpha\beta\gamma\delta} + \tilde{c}_1^{\alpha\beta\gamma\delta}, \quad \tilde{c} = c, d, e, f,$ <p>where the index ‘0’ refers to the elastic branch and ‘1’ refers to the Maxwell branch. The material tangent $\tilde{c}_1^{\alpha\beta\gamma\delta}$ is derived in Appendix A.3 for various material models.</p>

surface is discretized by bi-quadratic NURBS, if not stated otherwise. Numerical integration on the bi-unit parent element is performed using Gaussian quadrature with $(p+1) \times (q+1)$ quadrature points, which represents a very conservative approach. Here, p and q refer to the polynomial orders of the surface discretization in the two parametric directions. To post-process the surface quantities $\hat{a}_{\alpha\beta}$ and $\hat{b}_{\alpha\beta}$ at any point on the surface, an L^2 -projection is employed to map these values from the quadrature point level to the control point level. All quantities in this section are non-dimensionalized by the introduction of a reference length L_0 , time T_0 , and stiffness μ_0 , K_0 , or c_0 . For all examples, the shear viscosity model from Eq. (51) is employed.

5.1 2D viscoelastic membrane

The first examples study two-dimensional viscoelasticity of an initially square membrane to demonstrate typical viscoelastic behavior, such as stress relaxation, creep, and strain rate dependence. Fig. 4 shows the two setups that are used in this section to model pure shear and pure dilatation. The black crosses in the figures mark the positions where the surface quantities are evaluated for visualization. Since the deformations are homogeneous, a single finite element is used for the computation, if not stated otherwise.

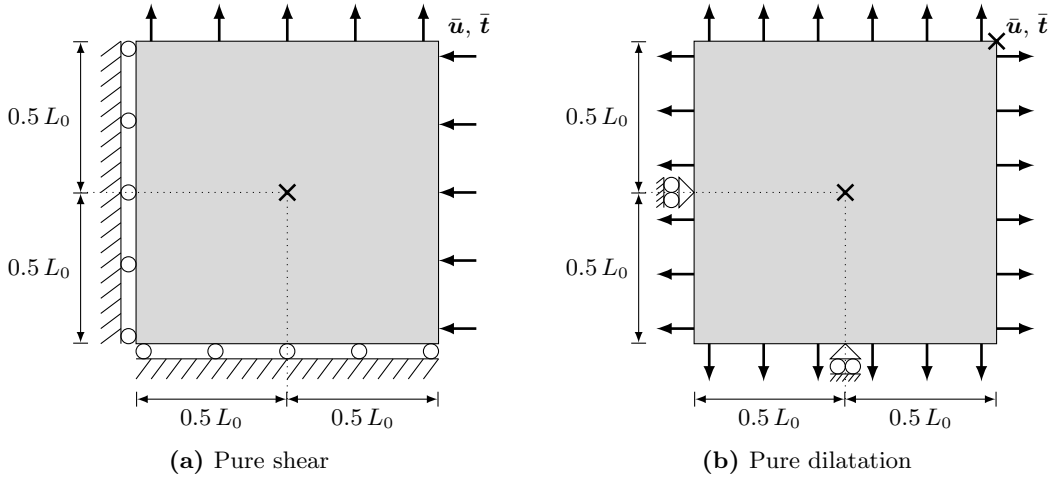


Figure 4: 2D viscoelastic membrane: Geometry, loading and boundary conditions for (a) pure shear and (b) pure dilatation. The black crosses mark the positions where surface quantities are evaluated.

5.1.1 Stress relaxation

First, the setup in Fig. 4a is considered and the Neo-Hookean material model is employed for both the elastic and Maxwell branch, see Eq. (38). The material parameters in the elastic branch are $\mu = 3\mu_0$ and $K = 0$; the ones in the Maxwell branch are $\mu_1 = \mu$ and $K_1 \in \{0, \mu/3\}$. The end time is $t_{\text{end}} = 5T_0$ and the constant time step size is chosen as $\Delta t = 0.1T_0$.

On the top edge, the displacement profile as shown in Fig. 5a is imposed, which leads to the stretch $\lambda_y = 1 + \bar{u}/L_0$. On the right edge, the stretch $\lambda_x = 1/\lambda_y$ is imposed to ensure pure shear.

The resulting stress σ_2^2 ,⁷ which is composed of elastic and Maxwell stresses, is shown over time in Fig. 5b for three different values of the in-plane shear viscosity η_s and the purely elastic case. The stress exhibits jumps whenever there is a jump of the imposed displacement. In the viscoelastic case, the magnitude of the stress is higher because the Maxwell stress is added to the total stress, see Eq. (49). Over time, the Maxwell stress relaxes such that the elastic stress level is approached. In Fig. 6, the invariants I_1 and I_1^{el} from Eqs. (9.1) and (21) are visualized over time. For $K_1 = 0$, the elastic invariant I_1^{el} is monotonically increasing. In contrast, if K_1 is not vanishing, I_1^{el} decreases to its initial value. This happens faster for lower values of η_s . This behavior happens because the employed shear viscosity model from Eq. (51) is not a pure shear model. Instead, it causes both shear and dilatation.

⁷ $\sigma_\beta^\alpha = \sigma^{\alpha\gamma} a_{\gamma\beta}$

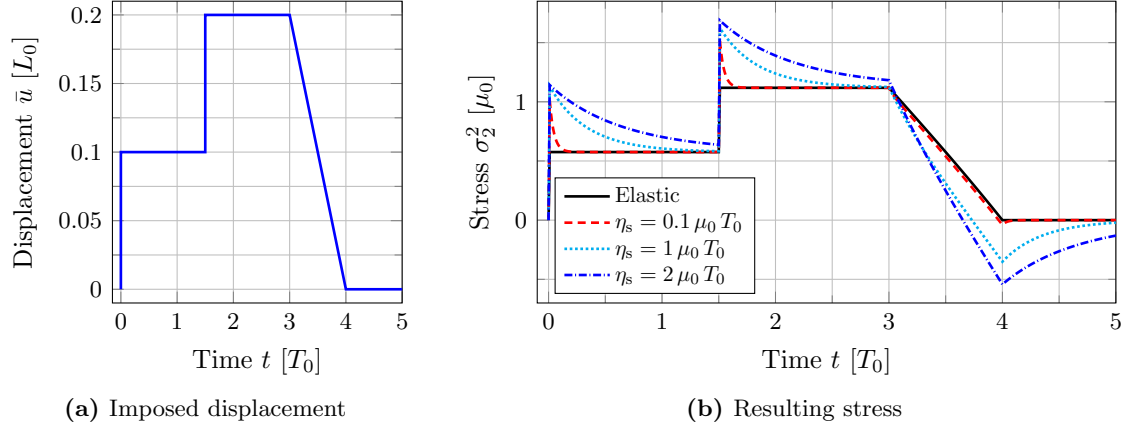


Figure 5: 2D viscoelastic membrane: Stress relaxation for pure shear (according to Fig. 4a).

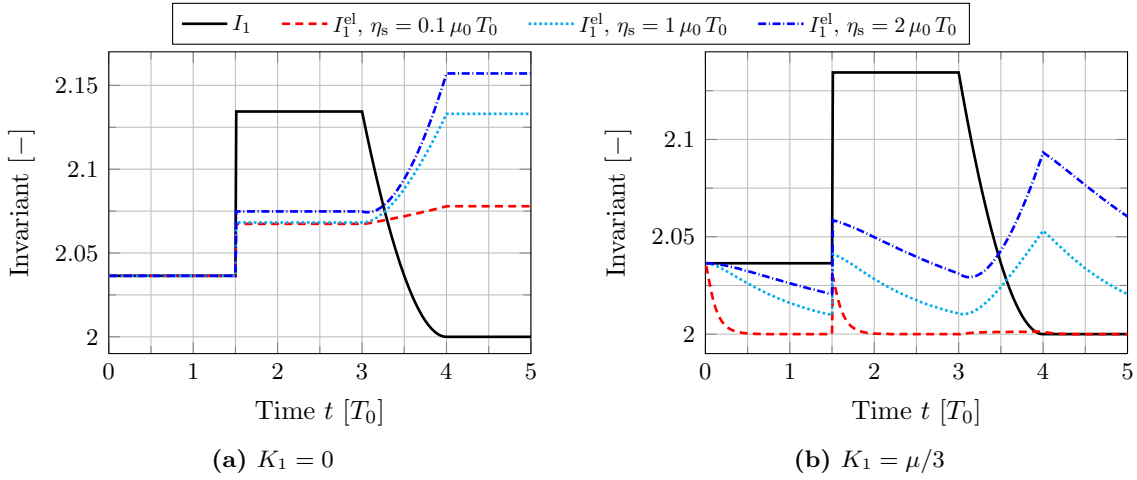
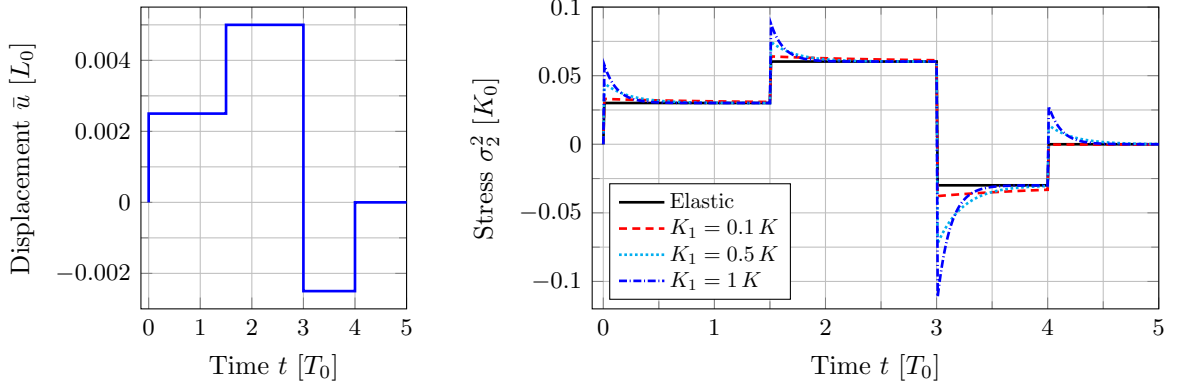


Figure 6: 2D viscoelastic membrane: Stress relaxation for pure shear: First invariant for the imposed displacement profile from Fig. 5a and two different areal bulk moduli K_1 .

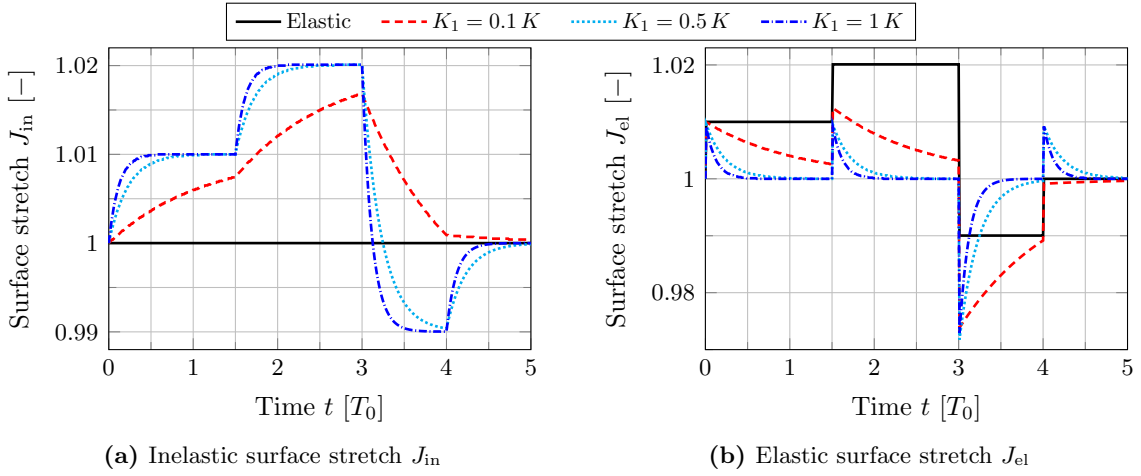
Next, pure dilatation is considered, see Fig. 4b, and the Koiter material model is employed, see Eq. (33). The material parameters in the elastic branch are $\mu = 0$ and $\Lambda = K = 3K_0$; the ones in the Maxwell branch are $\mu_1 = 0$, $\Lambda_1 = K_1$, and $\eta_s = 0.33 K_0 T_0$. The time stepping is the same as in the previous example. The displacement profile from Fig. 7a is imposed, and the surface quantities are evaluated at the center of the sheet, see Fig. 4b. The resulting stress σ_2^2 is shown in Fig. 7b, which exhibits similar behavior as in the previous example. For larger values of K_1 , the total stress is larger and the relaxation time decreases. The inelastic and elastic surface stretches, J_{in} and J_{el} , respectively, are visualized in Fig. 8. For larger values of K_1 , the inelastic surface stretch is also larger, whereas the elastic surface stretch decreases. Note that the total surface stretch $J = J_{\text{in}} J_{\text{el}}$ is equal to J_{el} in the purely elastic case.

5.1.2 Creep

Second, creep under pure dilatation (according to Fig. 4b) is considered using the Neo-Hookean material model from Eq. (38) with material parameters $\mu = 3\mu_0$, $K = \mu$, $\mu_1 = \mu$ and $K_1 = K$. The end time is $t_{\text{end}} = 5T_0$ and the constant time step size is chosen as $\Delta t = 0.1T_0$. Fig. 9a shows the imposed traction profile. The surface quantities are evaluated at the top right corner of the membrane, see the top right cross in Fig. 4b. Fig. 9b shows the resulting vertical displacement for different values of the in-plane shear viscosity η_s . A jump of the imposed

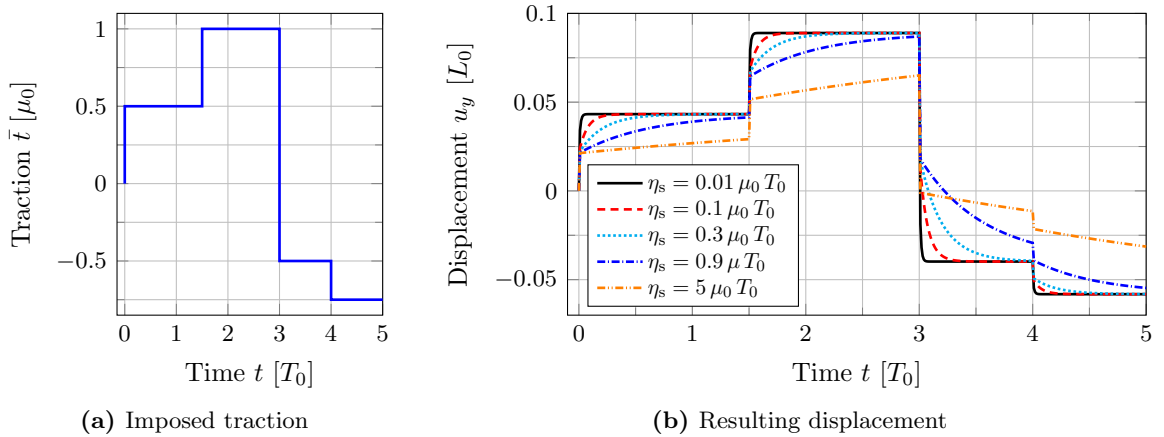


(a) Imposed displacement (b) Resulting stress
Figure 7: 2D viscoelastic membrane: Stress relaxation for pure dilatation (according to Fig. 4b).



(a) Inelastic surface stretch J_{in} (b) Elastic surface stretch J_{el}
Figure 8: 2D viscoelastic membrane: Stress relaxation for pure dilatation: Surface stretches for the imposed displacement profile from Fig. 7a. Note that the total surface stretch $J = J_{in} J_{el}$ is equal to J_{el} in the purely elastic case.

traction leads to an instantaneous elastic response, i.e. a jump of the displacement. Over time, the displacement magnitude increases further, which is known as creep.



(a) Imposed traction (b) Resulting displacement
Figure 9: 2D viscoelastic membrane: Creep for pure dilatation (according to Fig. 4b).

5.1.3 Strain rate dependence

Third, the setup in Fig. 4a is used again to show the influences of different strain rates and cyclic loading. The Neo-Hookean material model from Eq. (38) is used with $K_1 = \mu_1 = \mu = 1 \mu_0$, $K = 0$, and the in-plane shear viscosity is set to $\eta_s = 0.25 \mu_0 T_0$. The imposed displacement over time is given by the function

$$\bar{u}_y(t) = 0.25 L_0 \sin(\omega t), \quad (99)$$

with excitation frequency ω . At first, the time span $t \in [0, \pi/\omega]$ is considered such that only one loading-unloading cycle is computed. The time step size is constant and 500 time steps are used. Fig. 10 shows the total, elastic, and Maxwell stress over the displacement. In the elastic case, the stress-displacement curve is identical for loading and unloading, see Fig. 10b. But in the viscoelastic case, these curves are not coinciding. Instead, the unloading occurs at lower stress than the loading, which can be seen for both the total stress in Fig. 10a and the Maxwell stress in Fig. 10c. This indicates that energy is dissipated during the loading-unloading cycle, which is further studied in the next section. Fig. 10 shows that with increasing excitation frequency, and thus with increasing strain rate, the Maxwell stress is larger. Further, for very low and very high strain rates, the loading and unloading curves come closer to each other such that less energy is dissipated.

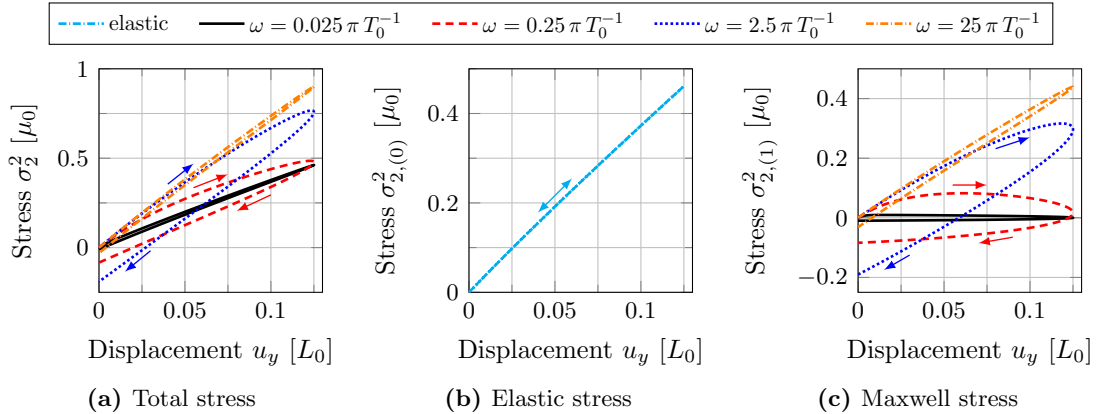


Figure 10: 2D viscoelastic membrane: Strain rate dependence for one loading-unloading cycle. The Maxwell branch exhibits hysteresis – the loading and unloading curves do not coincide.

5.1.4 Cyclic loading

Fourth, the same setup as in Sec. 5.1.3 with the displacement profile from Eq. (99) is considered, but the time span is now extended to $t \in [0, 20 \pi/\omega]$, such that ten loading-unloading cycles occur. For this, 10,000 time steps are used. The resulting stress-displacement curves are shown in Fig. 11 for three different excitation frequencies ω and $\eta_s = 1 \mu_0 T_0$. Note that the first loading-unloading cycle is slightly offset from the following cycles as the first one starts at zero stress, whereas the next ones start at non-vanishing stress. The areas within the hystereses are an indicator for the dissipated energy. This energy decreases for very low or very high excitation frequencies. Note that the shown results exhibit nonlinear and non-symmetric behavior in compression and tension. Fig. 12 shows the dissipated energy, see Eq. (53), over the excitation frequencies for three different values of η_s . For each setup, there exists an excitation frequency where the dissipation is maximum.

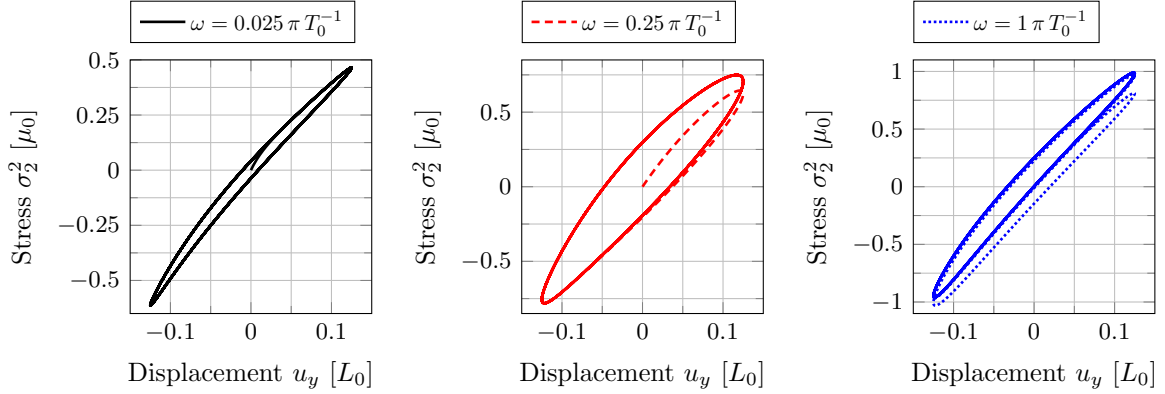


Figure 11: 2D viscoelastic membrane: Hystereses for cyclic loading and different excitation frequencies.

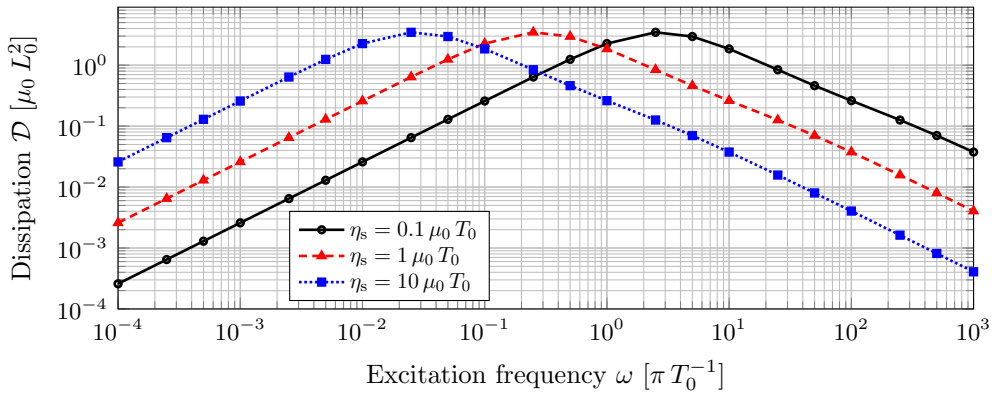


Figure 12: 2D viscoelastic membrane: Dissipation \mathcal{D} , see Eq. (53), over the excitation frequency ω for cyclic loading.

5.2 Inflated membrane balloon

This section deals with the inflation of a viscoelastic spherical rubber balloon, similar to the elastic counterpart considered in Sauer et al. (2014). This example is used to verify the formulation and implementation for membrane viscosity as an analytical solution for this problem can be derived. The finite element model is shown in Fig. 13a. Only a quarter of the sphere is used for the simulation and appropriate boundary conditions are provided to prevent rigid body motion and to maintain the symmetry of the inflating balloon across the gray marked planes. The bold black lines mark the patch interfaces between the four patches, of which the quarter mesh is composed. The finite element mesh contains $6m^2$ elements, where $2m$ ($m = 1, 2, \dots$) denotes the number of elements along the equator of the quarter sphere. The initial and current radii are denoted R and r , respectively. Likewise, the initial thickness is denoted T , while the current thickness is denoted \tilde{t} . As shown subsequently, the pressure initially increases but later decreases. Thus, the finite element computation is performed by imposing the enclosed volume V instead of the pressure p , see Sauer et al. (2014) for more details. The prescribed stretch λ as a function of time t is chosen as

$$\lambda(t) = \exp\left(\frac{t}{\tau_\lambda}\right), \quad (100)$$

with the characteristic time

$$\tau_\lambda := \frac{t_{\text{end}}}{\ln(\lambda_{\text{end}})}, \quad (101)$$

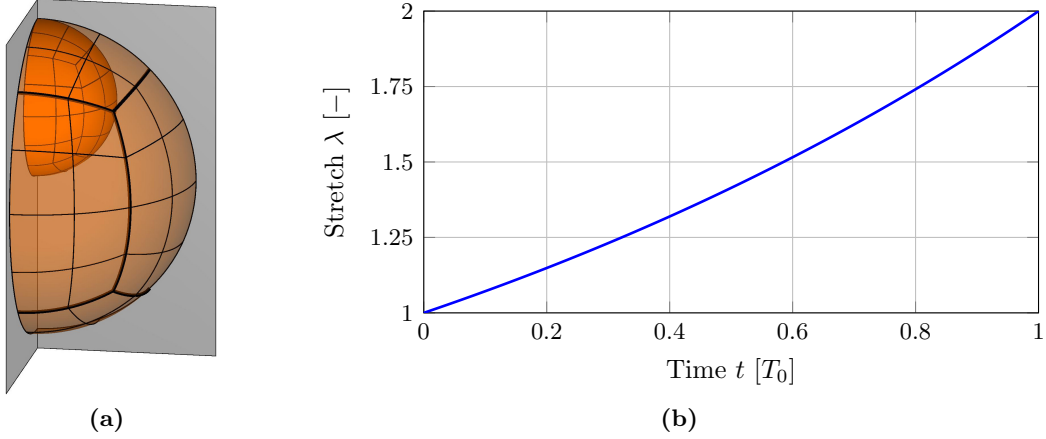


Figure 13: Inflated membrane balloon: (a) Initial and deformed configuration (with the bold black lines marking patch interfaces) and (b) imposed stretch over time for $t_{\text{end}} = 1 T_0$ and $\lambda_{\text{end}} = 2$, see Eq. (100).

where t_{end} denotes the end time and λ_{end} denotes the final stretch, see Fig. 13b. The choice for $\lambda(t)$ in Eq. (100) allows for an analytical solution. The resulting volume is then given by

$$V(t) = \exp\left(\frac{3t}{\tau_\lambda}\right) V_0, \quad (102)$$

where the relation $V = \lambda^3 V_0$ with initial volume V_0 has been used. For this example, λ_{end} is set to 2, such that the final volume is $V(t_{\text{end}}) = 8 V_0$. The elastic behavior of the rubber membrane is described by the incompressible Neo-Hookean material model from Eq. (41), and the elastic energy in the Maxwell branch is given by Eq. (36) with $\Lambda = 0$.

In analogy to Eq. (49), the total pressure p can be decomposed into the contributions

$$p(t) = p_{\text{el}}(t) + p_{\text{visc}}(t), \quad (103)$$

where $p_{\text{el}}(t)$ is the pressure function coming from the elastic branch, and $p_{\text{visc}}(t)$ is the one from the Maxwell branch. These two contributions $p_\bullet(t)$ are derived in detail in Appendix B.1, and they are given by

$$p_{\text{el}}(t) = \frac{2\mu}{R} \left(\frac{1}{\lambda} - \frac{1}{\lambda^7} \right) = \frac{2\mu}{R} \left(\left(\frac{V_0}{V} \right)^{\frac{1}{3}} - \left(\frac{V_0}{V} \right)^{\frac{7}{3}} \right). \quad (104)$$

and

$$p_{\text{visc}}(t) = \frac{2\mu_1}{R} \left(\frac{1}{\lambda} - \frac{1}{\lambda^3 \hat{a}_{\text{ev}}} \right), \quad (105)$$

and

$$\hat{a}_{\text{ev}}(t) := \frac{\mu_1 \tau_\lambda \exp(-2t/\tau_\lambda) - 2\eta_s \exp(-\mu_1 t/\eta_s)}{\mu_1 \tau_\lambda - 2\eta_s}. \quad (106)$$

First, the convergence of the model with respect to mesh and time step size refinement is investigated. For this, the pressure error

$$\epsilon_p := \frac{|p_{\text{num}}(t_{\text{end}}) - p_{\text{ana}}(t_{\text{end}})|}{p_{\text{ana}}(t_{\text{end}})}, \quad (107)$$

is defined. The parameters used for the convergence study are $\mu_1 = \mu$, $\eta_s = 0.1 \mu T_0$, and $t_{\text{end}} = 1 T_0$. The time step size Δt is chosen to be constant in $[0, t_{\text{end}}]$. Fig. 14 clearly shows

that the dominating error stems from the time step size, and not from the finite element mesh. Beyond $m \geq 2$, an increase of the number of elements for fixed Δt does not lead to a further decrease of the error. As the deformation in this example is homogeneous, even a small number of elements is sufficient to accurately capture it. In contrast, the error decreases linearly with a decrease of the time step size Δt . This convergence rate is also the expected rate for the employed implicit Euler scheme. As the mesh $m = 2$ is sufficient to accurately capture the deformation, this mesh is used for all subsequent balloon examples.

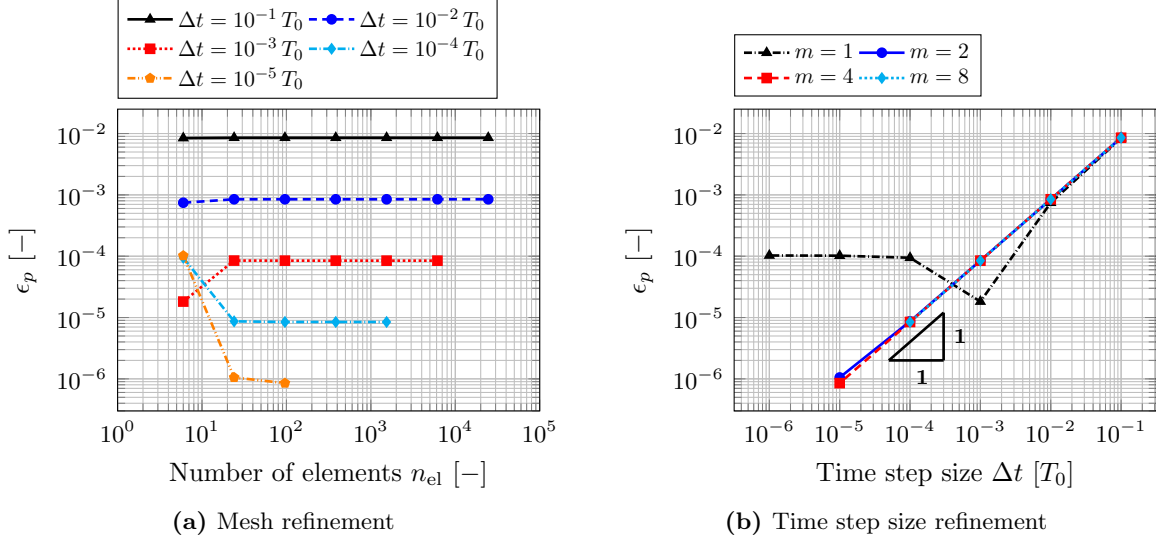


Figure 14: Inflated membrane balloon: Convergence of the pressure error ϵ_p , see Eq. (107), over mesh and time step size refinement.

Second, the $p(t)$ relation is shown over a logarithmic time axis in Fig. 15a for different values of the in-plane shear viscosity η_s and fixed $\mu_1 = \mu$, and in Fig. 15b for different values of the stiffness ratio $\chi_1 := \mu_1/\mu$ and fixed $\eta_s = 0.5 \mu T_0$. The end time is fixed to $t_{\text{end}} = 1 T_0$ and 1,000 time steps are used. The strong nonlinear behavior is captured accurately by the numerical results as Fig. 15 shows. For increasing values of η_s or χ_1 , the magnitude of the pressure increases. The location of the maximum pressure also shifts when those parameters are varied.

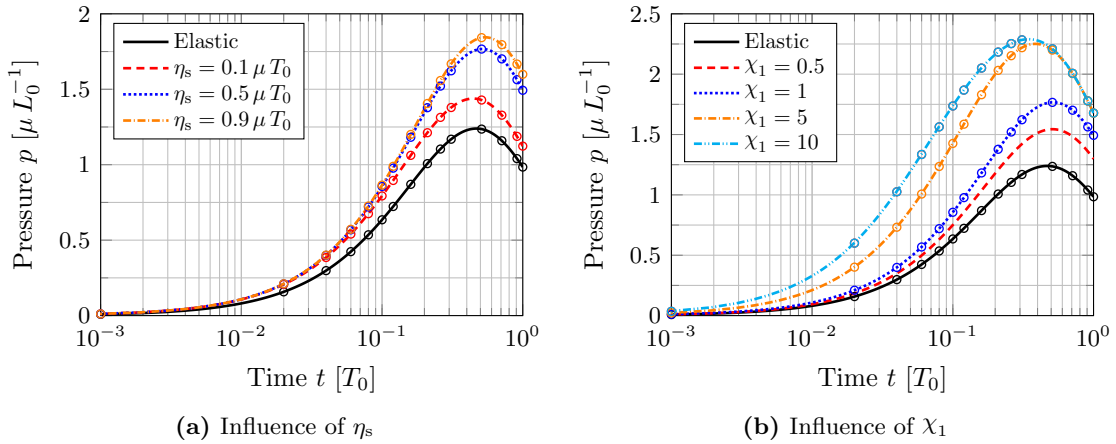


Figure 15: Inflated membrane balloon: Influence of the in-plane shear viscosity η_s and stiffness ratio $\chi_1 := \mu_1/\mu$ on the pressure p . The circles mark the numerical results at various snapshots in time, while the lines show the corresponding analytical results.

Third, the effect of the loading rate is investigated. For this, the end time t_{end} is varied in Eq. (101), while the parameters $\eta_s = 0.5 \mu T_0$ and $\chi_1 = 1$ are fixed. For the temporal integration, 1,000 time steps are used. As shown in Fig. 16a, the total pressure decreases for increasing t_{end} , and the maximum is shifted to later times. The dissipation \mathcal{D} , see Eq. (53), is visualized in Fig. 16b for three different values of the in-plane shear viscosity. For each value of η_s , there exists one characteristic time τ_λ , see Eq. (101), for which the dissipation is maximal.

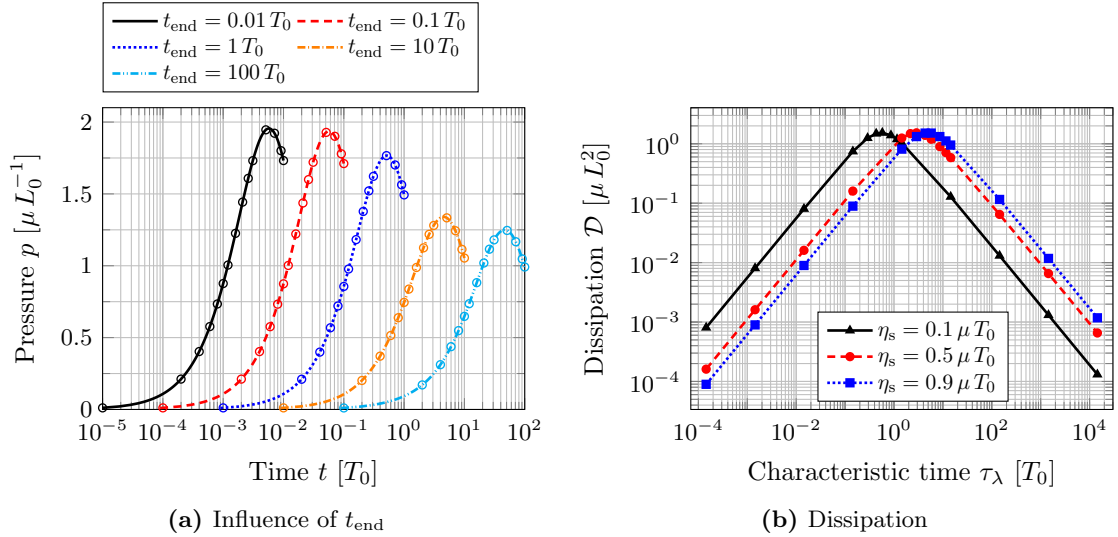


Figure 16: Inflated membrane balloon: (a) Influence of the end time t_{end} on the pressure p . Here, the circles mark the numerical results at various snapshots in time, while the lines mark the corresponding analytical results. (b) Dissipation \mathcal{D} , see Eq. (53), over the characteristic time τ_λ defined in Eq. (101).

5.3 Pure bending of a flat strip

This section presents the pure bending of an initially flat shell to verify the formulation for viscoelastic bending. The geometry, boundary and loading conditions are shown in Fig. 17. At the left and right edge, a distributed bending moment M is applied. Additionally, a displacement is applied on the right edge and a pressure acts on the whole structure. This loading combination ensures that the initially flat sheet is bent into a curved sheet with curvature κ_2 , but not stretched, i.e. the surface stretches are exactly $\lambda_1 = \lambda_2 = 1$.⁸ The curvature is related to the radius r of the deformed shell via $\kappa_2 = 1/r$. The membrane response in the elastic branch is based on the Neo-Hookean model from Eq. (36), and the bending response in the elastic and Maxwell branch is based on the Koiter bending model from Eq. (44).

Choosing the applied moment

$$M(t) = M_v t, \quad (108)$$

with constant loading rate M_v , the sheet becomes stretch-free for the imposed displacement and pressure

$$\bar{u}_y(t) = -\left(S - \frac{2}{\kappa_2(t)} \sin\left(\frac{S \kappa_2(t)}{2}\right)\right), \quad \text{and} \quad p(t) = -\left((c + c_1) \kappa_2(t)^3 - c_1 \kappa_2(t)^2 \kappa_2^{\text{in}}(t)\right), \quad (109)$$

⁸According to thin shell theory, there is a high-order coupling between curvatures and stretches; see, for example, Sauer and Duong (2017).

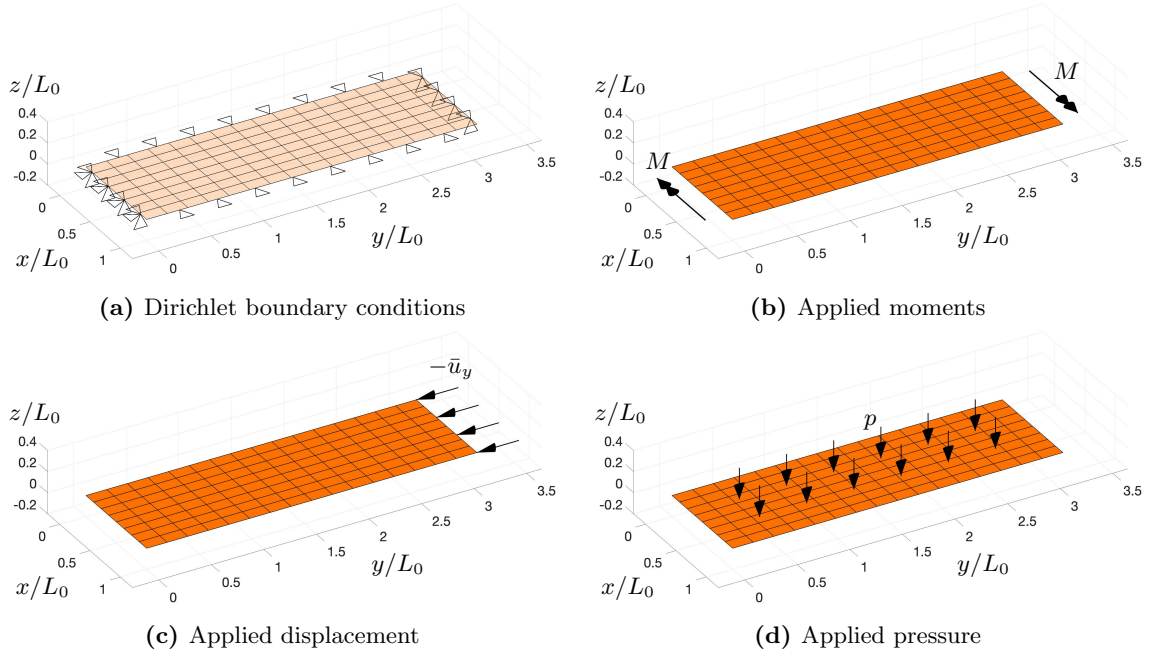


Figure 17: Pure bending of a flat strip: Setup including Dirichlet boundary conditions and three different external loads that are simultaneously applied.

where $S = \pi$ denotes the length of the sheet in y -direction. Eq. (108) is a chosen rate that allows for an analytical solution as shown in Appendix B.2. The displacement $\bar{u}_y(t)$ in Eq. (109.1) is chosen such that a perfect circular arc is obtained for any given curvature $\kappa_2(t)$. The pressure $p(t)$ in Eq. (109.2) is required to equilibriate the structure, and it follows from the well-known formula for thin-walled cylindrical pressure vessels, which requires $p(t) = N_2^2(t)/r(t) = N_2^2(t) \kappa_2(t)$, where N_2^2 denotes the in-plane stress component in y -direction. The derivation of the latter is provided in Appendix B.2. This problem can be solved analytically, which leads to the curvatures

$$\kappa_2^{\text{in}}(t) = \frac{M_v \tau_b}{c} \left(e^{-t/\tau_b} + \frac{t}{\tau_b} - 1 \right), \quad (110)$$

with the characteristic time

$$\tau_b := \frac{\eta_b (c + c_1)}{c c_1}, \quad (111)$$

and

$$\kappa_2(t) = \frac{M(t) + c_1 \kappa_2^{\text{in}}(t)}{c + c_1}, \quad (112)$$

see Appendix B.2. The loading rate M_v in Eq. (108) is chosen in a way, such that the final curvature is equal to $\kappa_2^{\text{end}} := \kappa_2(t_{\text{end}})$. Using Eqs. (108) and (110)–(112), this leads to the constant loading rate

$$M_v := \frac{c + c_1}{t_{\text{end}} + \frac{c_1 \tau_b}{c} \tilde{\kappa}_{2,\text{end}}^{\text{in}}}, \quad (113)$$

where $\kappa_2^{\text{in}}(t_{\text{end}}) := M_v \tilde{\kappa}_{2,\text{end}}^{\text{in}}$ with $\tilde{\kappa}_{2,\text{end}}^{\text{in}} := \tau_b (\exp(-t_{\text{end}}/\tau_b) + t_{\text{end}}/\tau_b - 1)/c$.

First, the convergence with respect to the two relative curvature errors

$$\epsilon_\kappa := \frac{|\kappa_{2,\text{num}}(t_{\text{end}}) - \kappa_{2,\text{ana}}(t_{\text{end}})|}{\kappa_{2,\text{ana}}(t_{\text{end}})}, \quad \text{and} \quad \epsilon_\kappa^{\text{in}} := \frac{|\kappa_{2,\text{num}}^{\text{in}}(t_{\text{end}}) - \kappa_{2,\text{ana}}^{\text{in}}(t_{\text{end}})|}{\kappa_{2,\text{ana}}^{\text{in}}(t_{\text{end}})}, \quad (114)$$

is investigated. The chosen parameters are $\mu = 10 L_0^2/c$, $\Lambda = 5 L_0^2/c$, $c = c_1$, $\eta_b = 0.5 c T_0$, $t_{\text{end}} = 1 T_0$, and $\kappa_2^{\text{end}} = 0.5$, such that $\tau_b = 1 T_0$. Fig. 18 shows that the errors converge linearly with an increase of the number of elements and a decrease of the time step size.

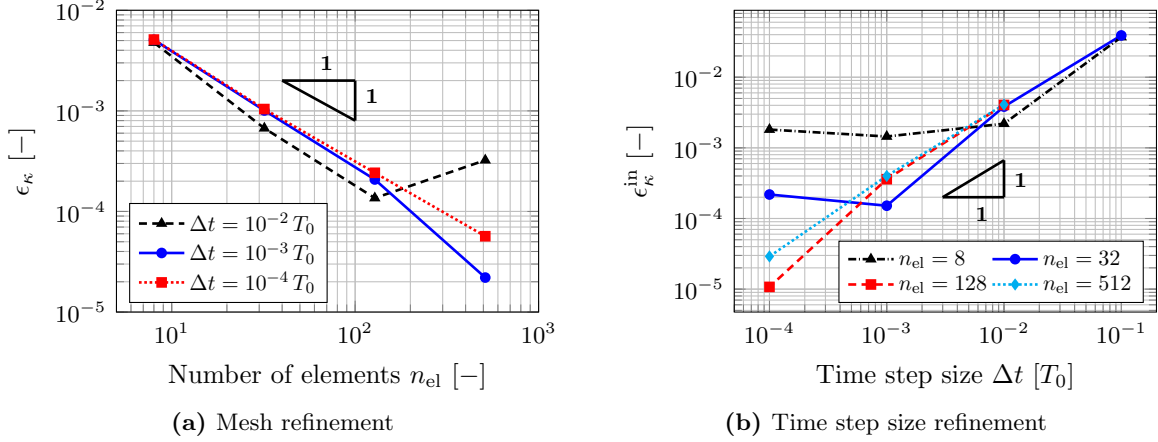


Figure 18: Pure bending of a flat strip: Convergence of the relative curvature errors, see Eq. (114), over mesh and time step size refinement.

Fig. 19 shows the deformed surface at various snapshots in time for the parameters $\mu = 10 L_0^2/c$, $\Lambda = 5 L_0^2/c$, $c = c_1$, $\eta_b = 0.5 c T_0$, $t_{\text{end}} = 1 T_0$, $\kappa_2^{\text{end}} = 1$, and $\tau_b = 1 T_0$. The surfaces are colored with the relative curvature error ϵ_κ . The maximum error of the surface stretches $|\lambda_1 - 1|$ and $|\lambda_2 - 1|$ over all time steps are of order $\mathcal{O}(10^{-3})$, which indicates that the chosen boundary and loading conditions in Fig. 17 work well to obtain stretch-free bending deformations. The relative curvature error is of the same magnitude. At $t = t_{\text{end}}$, the sheet is deformed into a half circle exhibiting large bending deformations. The applied loads over time are visualized in Fig. 20 for this example.

Fig. 21 shows the total and inelastic curvatures, κ_2 and κ_2^{in} , respectively, over time for different values of η_b . While the total curvature is not influenced significantly by η_b , the curvature of the intermediate configuration shows a strong dependency on η_b . For smaller values of η_b , the inelastic curvature increases, i.e. the intermediate surface is bent more.

5.4 Inflated spherical shell

This section considers a similar example as in Sec. 5.2, but here, also bending resistance is considered. The setup is the same as in Fig. 13 and the parameters $\lambda_{\text{end}} = 4^{1/3}$ and $t_{\text{end}} = 1 T_0$ are used, see also Eq. (101). The final volume is thus four times as large compared to the initial volume, i.e. $V(t_{\text{end}}) = 4 V_0$. The employed thin shell formulation requires C^1 -continuity of the numerical discretization, such that patch constraints need to be enforced along the marked patch interfaces Γ in Fig. 13a. A detailed derivation for the enforcement of patch constraints is provided in Paul et al. (2020a). Here, the Lagrange multiplier method with element-wise constant interpolation is employed to enforce the constraint

$$\mathbf{g}_n^{\text{planar}} = \mathbf{n} - \tilde{\mathbf{n}} = \mathbf{0}, \quad \forall \mathbf{x} \in \Gamma, \quad (115)$$

along the patch interfaces Γ . Here, \mathbf{n} and $\tilde{\mathbf{n}}$ denote the two surface normals of the elements adjacent to Γ . Further, the symmetry across the gray marked symmetry planes is enforced by the constraint in Eq. (115). In that case, $\tilde{\mathbf{n}}$ denotes the normal of the symmetry plane.

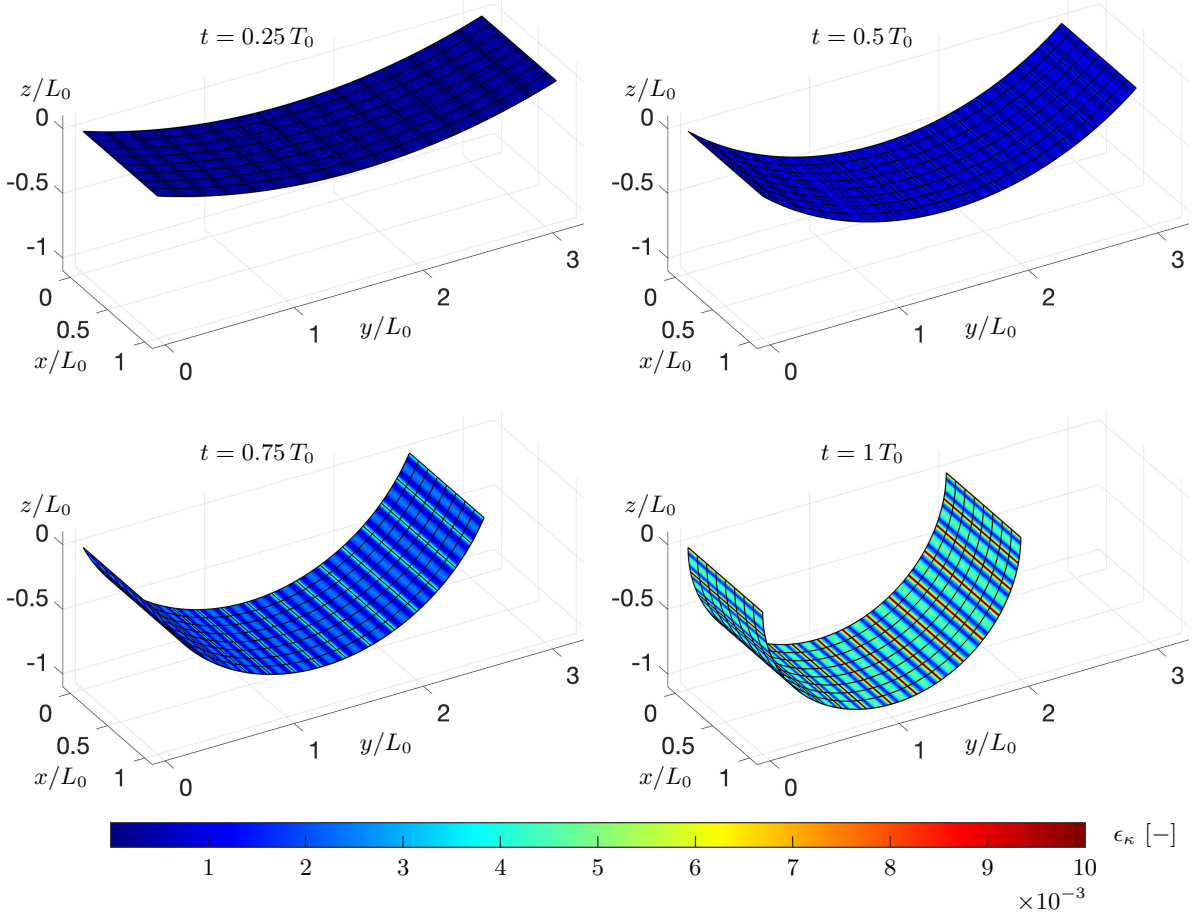


Figure 19: Pure bending of a flat strip: Deformed surfaces at various snapshots in time colored by the relative curvature error ϵ_κ see Eq. (114.1).

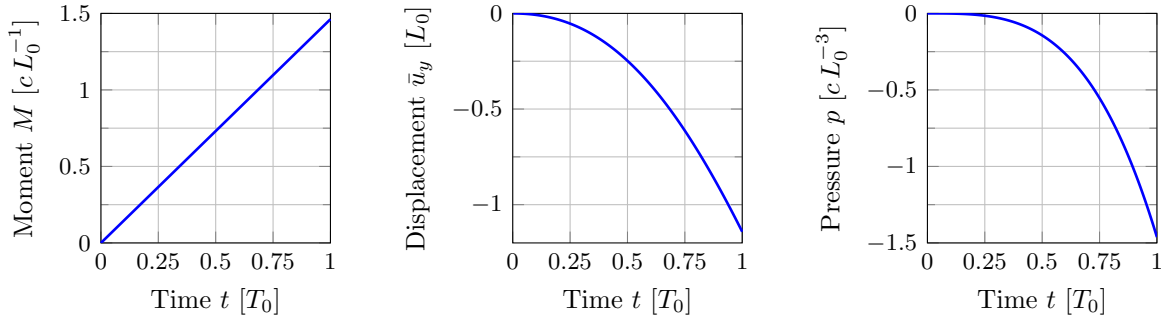


Figure 20: Pure bending of a flat strip: Imposed loads over time, see also Fig. 17.

In the elastic branch, the membrane energy density is given by the incompressible Neo-Hookean material model from Eq. (41), and the bending energy density is given by the Helfrich model from Eq. (46). For the Maxwell branch, the Neo-Hookean model from Eq. (36) with $\Lambda = 0$ and Koiter bending model from Eq. (44) are employed.

Similar to Sec. 5.2, the pressure is composed of two contributions, i.e.

$$p(t) = p_{\text{el}}(t) + p_{\text{visc}}(t), \quad (116)$$

where $p_{\text{el}}(t)$ is the pressure function coming from the elastic branch, and $p_{\text{visc}}(t)$ is the one from the Maxwell branch. These two contributions $p_\bullet(t)$ are derived in detail in Appendix B.3, and

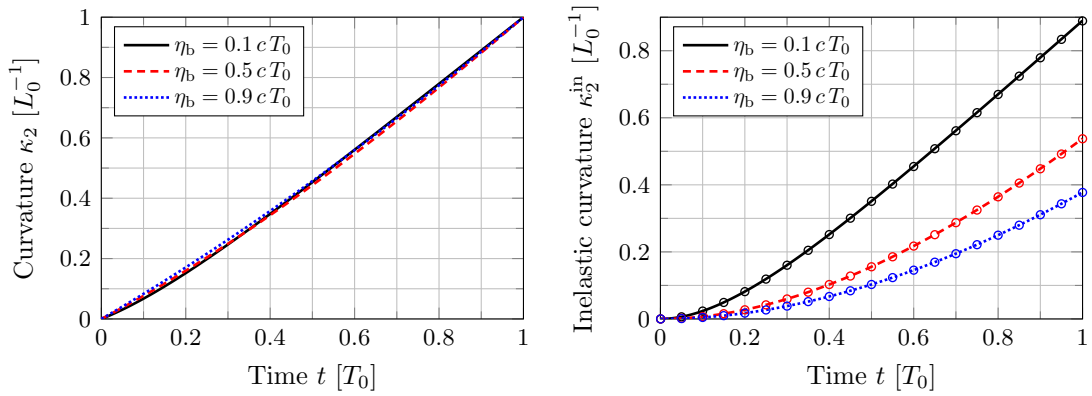


Figure 21: Pure bending of a flat strip: Influence of the parameter η_b on the total and inelastic curvatures, κ_2 and κ_2^{in} , respectively. The circles mark the numerical results at various snapshots in time, while the lines show the corresponding analytical results. Given κ_2 and κ_2^{in} , the elastic curvature follows from $\kappa_2 = \kappa_2^{\text{el}} + \kappa_2^{\text{in}}$, which is a consequence of Eq. (22).

they are given by

$$p_{\text{el}}(t) = \frac{2}{R^3} \left[\mu R \left(\frac{1}{\lambda} - \frac{1}{\lambda^7} \right) + k \left(\frac{H_0 R}{\lambda^2} + \frac{H_0^2 R^2}{\lambda} \right) \right]. \quad (117)$$

and

$$p_{\text{visc}}(t) = \frac{2}{R^3} \left[\mu_1 R^2 \left(\frac{1}{\lambda} - \frac{1}{\lambda^3 \hat{a}_{\text{ev}}} \right) + c_1 \hat{a}_{\text{ev}} \left(\frac{1}{\lambda} - \frac{\hat{b}_{\text{ev}}}{\lambda^2} \right) \right], \quad (118)$$

with $\hat{a}_{\text{ev}}(t)$ given in Eq. (106) and $\hat{b}_{\text{ev}}(t)$ given by

$$\hat{b}_{\text{ev}}(t) := \frac{c_1 \tau_\lambda \exp(t/\tau_\lambda) + \eta_b \exp(-c_1 t/\eta_s)}{\eta_b + c_1 \tau_\lambda}. \quad (119)$$

First, the convergence of the model with respect to time step size refinement is investigated. The parameters are $\mu = 5 k/R^2$, $\mu_1 = \mu$, $c_1 = k$, $k^* = 0$, $\eta_s = 0.5 \mu_0 T_0$, $\eta_b = 0.5 k T_0$, $H_0 = 1/R$, and $t_{\text{end}} = 1 T_0$. Fig. 22 shows the convergence of the pressure error ϵ_p , see Eq. (107), over the time step size Δt . As expected for the implicit Euler scheme, the error decreases linearly with decreasing time step size. There is no significant difference between the considered meshes for $m \geq 2$, such that the mesh $m = 2$ is used for the subsequent examples.

For the subsequent results, the parameters as given above are used if not stated otherwise. The time step size is set to $\Delta t = 10^{-3} T_0$. Fig. 23 shows the resulting pressure over time relation for different values of η_s and η_b , and two different values of $H_0 \in \{0, 1/R\}$. With increasing η_s and decreasing η_b , the total pressure increases. Further, the pressure is larger for $H_0 = 1/R$ than for $H_0 = 0$.

5.5 Sagging Scordelis-Lo roof

This section presents a viscoelastic shell that exhibits inhomogeneous deformations. The geometry, loading and boundary conditions are visualized in Fig. 24. The setup corresponds to the Scordelis-Lo roof (Macneal and Harder, 1985).

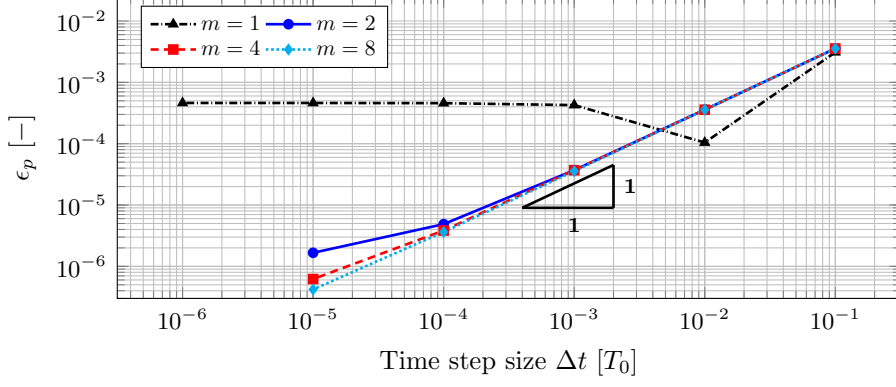


Figure 22: Inflated spherical shell: Convergence of the pressure error ϵ_p , see Eq. (107), over time step size refinement.

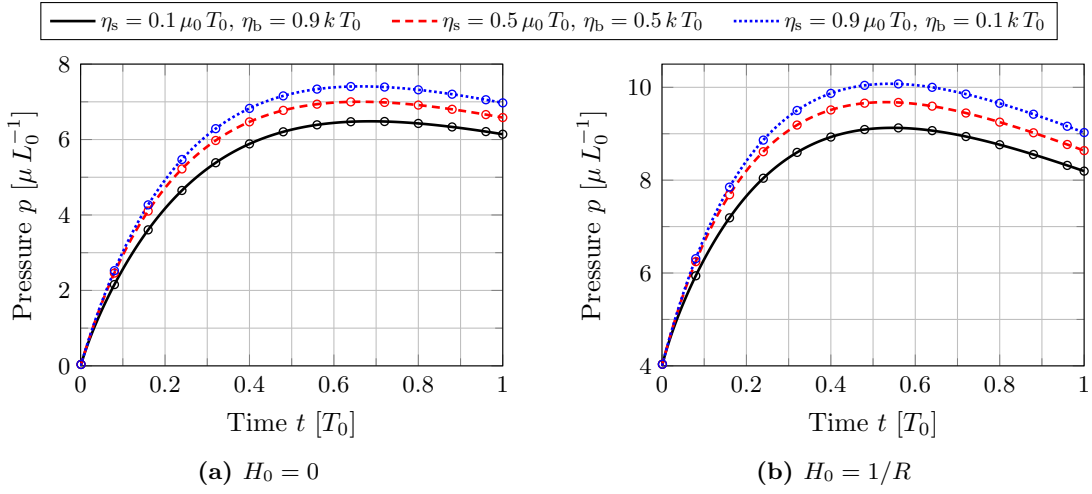


Figure 23: Inflated spherical shell: Influence of the in-plane shear viscosity η_s and out-of-plane viscosity η_b on the pressure p for two different values of H_0 . The circles mark the numerical results at various snapshots in time, while the lines show the corresponding analytical results.

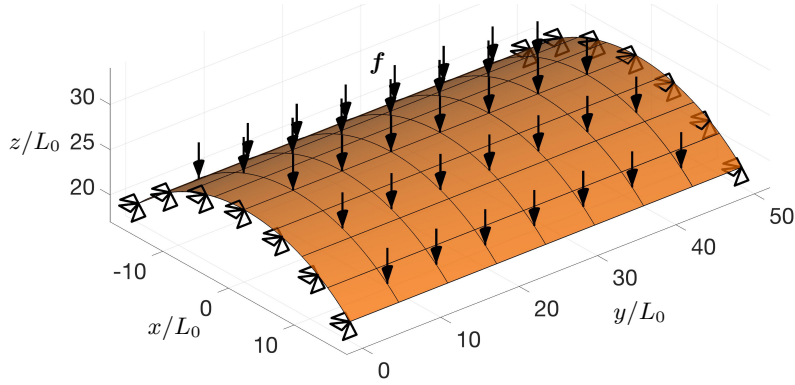


Figure 24: Sagging Scordelis-Lo roof: Geometry, loading and boundary conditions.

The following time-dependent load is applied

$$\mathbf{f}(t) = f_v(t) \begin{bmatrix} 0 \\ 0 \\ -1 \end{bmatrix}, \quad \text{where} \quad f_v(t) := \frac{1}{25} \begin{cases} \frac{f_0}{t_0} t, & t \leq t_0 \\ f_0, & t > t_0 \end{cases}, \quad (120)$$

with $t_0 = 10 T_0$ and $f_0 = 1 \mu_0 / L_0$. The Neo-Hookean material model from Eq. (38) is used

for the membrane response in the elastic and Maxwell branches, and the Koiter model from Eq. (44) is employed for the bending response in both branches. For the elastic case, the

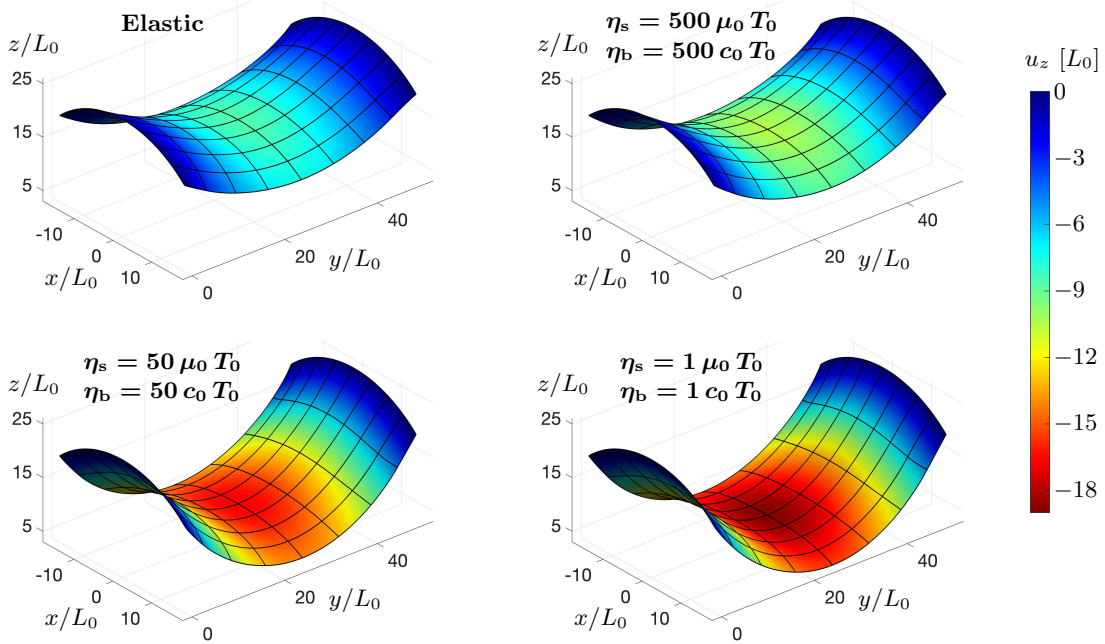


Figure 25: Sagging Scordelis-Lo roof: Final deformation for the elastic and viscoelastic case for three different values of η_s and η_b . The surfaces are colored by the vertical displacement u_z .

material parameters $\mu = 10 \mu_0$, $K = 10 \mu_0$, $c = 10 \mu_0 L_0^2$, and $\mu_1 = K_1 = c_1 = 0$ are used. For the viscoelastic case, the material parameters $\mu = 2 \mu_0$, $K = 2 \mu_0$, $c = 2 \mu_0 L_0^2$, $\mu_1 = 8 \mu_0$, $K_1 = 8 \mu_0$, and $c_1 = 8 \mu_0 L_0^2$ are used. Further, $c_0 := \mu_0 L_0^2$. The finite element mesh is constructed from 8 elements in each direction, the end time is $t_{\text{end}} = 50 T_0$, and 1,000 time steps are used.

The deformed structure is visualized in Fig. 25 for the elastic and viscoelastic case using different values for η_s and η_b . As shown, the creep is considerably larger for smaller η_s and η_b .

Fig. 26 shows the vertical displacement u_z and the surface stretch J over time. There are large creep deformations, which happen faster for smaller values of η_s and η_b . The decomposition of the surface stretch into its inelastic and elastic components, see Eqs. (19)–(20), is visualized in Fig. 27.

In Fig. 28, the intermediate mean curvature \hat{H} and mean curvature H are shown over time. The curvature is larger for smaller values of η_s and η_b , which can also be seen in Fig. 25, e.g. the creep deformations are larger for small η_s and η_b in the given time span $t \in [0, t_{\text{end}}]$.

5.6 Cube encased by a viscoelastic surface

This section highlights that the presented formulation for viscoelastic shells can be applied to model boundary viscoelasticity of 3D bodies without any further modifications. The finite element connectivity automatically enforces the coupling between bulk and surface elements and their constitutive behavior. For this, a cube with side length $2 L_0$ is encased with a viscoelastic surface. Only one eighth of the geometry is modeled by exploiting the symmetry of the problem and the mesh is *a priori* refined towards the sharp edges, see Fig. 29. A similar example is considered by Dortdivanlioglu and Javili (2021). In total, 512 hexahedral elements and 192

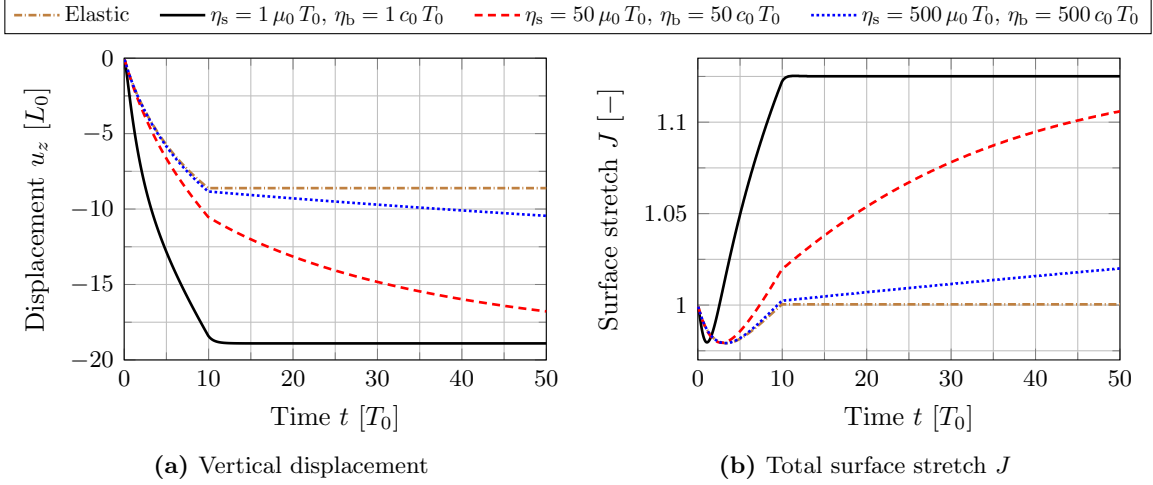


Figure 26: Sagging Scordelis-Lo roof: (a) Vertical displacements and (b) surface stretches for different values of η_s and η_b over time, measured at the center of the structure.

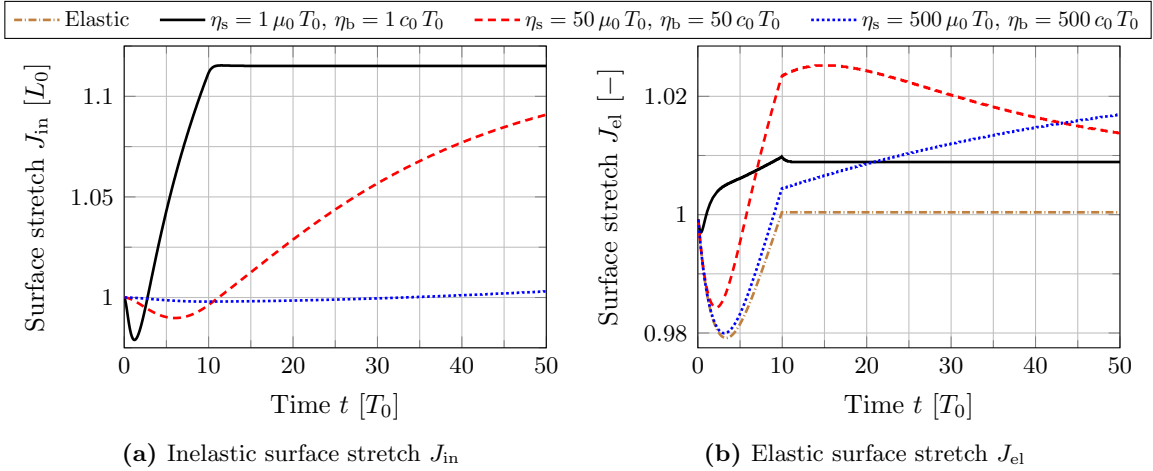


Figure 27: Sagging Scordelis-Lo roof: (a) Inelastic and (b) elastic surface stretches for different values of η_s and η_b over time, measured at the center of the structure. The total surface stretch, shown in Fig. 26b, satisfies $J = J_{in} J_{el}$.

quadrilateral elements are used to discretize the eighth cube and its encasing surface, respectively. Both are discretized by quadratic NURBS shape functions. The material behavior of the bulk material is modeled by a Neo-Hookean material model with elastic energy density and stresses

$$\tilde{\Psi} = \frac{\tilde{\Lambda}}{2} (\ln \tilde{J})^2 + \frac{\tilde{\mu}}{2} (\tilde{I}_1 - 3 - 2 \ln \tilde{J}), \quad \text{and} \quad \tilde{\boldsymbol{\sigma}} = \frac{\tilde{\Lambda}}{\tilde{J}} \ln \tilde{J} + \frac{\tilde{\mu}}{\tilde{J}} (\tilde{\mathbf{B}} + \tilde{\mathbf{I}}). \quad (121)$$

Here, $\tilde{\mathbf{I}}$ is the full identity in 3D, $\tilde{\mathbf{B}}$ is the left Cauchy-Green tensor in 3D, and \tilde{I}_1 and \tilde{J} are the invariants of $\tilde{\mathbf{B}}$. A tilde is added to avoid confusion with the corresponding surface quantities presented in Sec. 2.2. The material parameters for the bulk are $\tilde{\Lambda} = 5 \tilde{\Lambda}_0$ and $\tilde{\mu} = 5 \tilde{\Lambda}_0$. The elastic energy density in the elastic branch is given by Eq. (42) with prescribed surface tension γ . Since this model provides no deviatoric surface stiffness, the second part of Eq. (38) with $\mu = 1 \tilde{\Lambda}_0 L_0$ is added for numerical stabilization. For the Maxwell branch, the spring element from Fig. 2 is omitted, such that the constitutive model resembles a Kelvin model with $\hat{a}_{\alpha\beta} = a_{\alpha\beta}$, $J_{in} = J$, and $J_{el} = 1$. The dashpot is chosen to follow model (52), which in this special case is a pure dilatational model that requires no evolution laws and can be directly computed using $\dot{J} \approx (J - J_n)/\Delta t$, where J_n denotes the surface stretch from the previous time

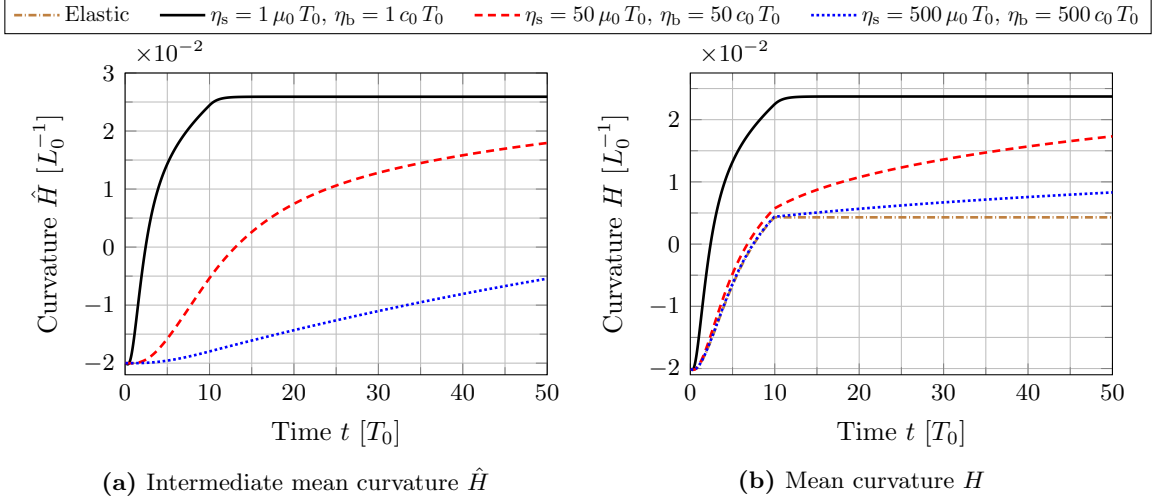


Figure 28: Sagging Scordelis-Lo roof: (a) Intermediate mean curvature and (b) mean curvature for different values of η_s and η_b over time, measured at the center of the structure.

step. The surface tension is imposed over time as

$$\gamma(t) = \gamma_0 \begin{cases} t/(2.5 T_0), & t \leq 2.5 T_0 \\ 1, & t > 2.5 T_0 \end{cases}. \quad (122)$$

The end time is $t_{\text{end}} = 10 T_0$ and 2,500 time steps are used for the temporal integration.

Fig. 29 shows the deformed geometry at t_{end} for different values of γ_0 and fixed $\eta_s = 1 \tilde{\Lambda}_0 L_0 T_0$. Energetically, a sphere is the optimal geometry for constant surface tension. Thus, for larger prescribed surface tension, the bulk deforms more into a spherical shape. Due to the stiffness of the bulk material, not a perfect sphere is obtained, but the sharp edges and corners are smoothed out.

The displacement norm $\|\mathbf{u}\|_2 = \|\mathbf{x} - \mathbf{X}\|_2$ over time is plotted in Fig. 30a for different values of the in-plane shear viscosity η_s and fixed $\gamma_0 = 5 \tilde{\Lambda}_0 L_0$, and in Fig. 30b for different values of the surface tension γ_0 and fixed $\eta_s = 1 \tilde{\Lambda}_0 L_0 T_0$. Fig. 30a shows creep behavior, which becomes more pronounced for increasing η_s . Fig. 30b shows that larger values of the surface tension lead to larger deformations, see also Fig. 29.

6 Conclusion

This work presents a computational formulation to model isotropic finite strain viscoelasticity for membranes, thin shells, and boundaries of 3D bodies. The material behavior is modeled based on the generalized viscoelastic solid, for which a multiplicative split of the surface deformation gradient is employed. The implementation of membrane and bending viscosity is verified by several numerical examples and ideal convergence rates are obtained in all cases. The chosen examples capture large deformations and standard viscoelasticity behavior of thin shells, as well as boundary viscoelasticity of 3D bodies.

This work demonstrates that the previously developed multiplicative split of the surface deformation gradient works robustly and accurately in finite strain computations. The employed direct surface formulation and its decomposition of the elastic energy density into membrane and bending parts makes the constitutive modeling more flexible. For example, one can consider

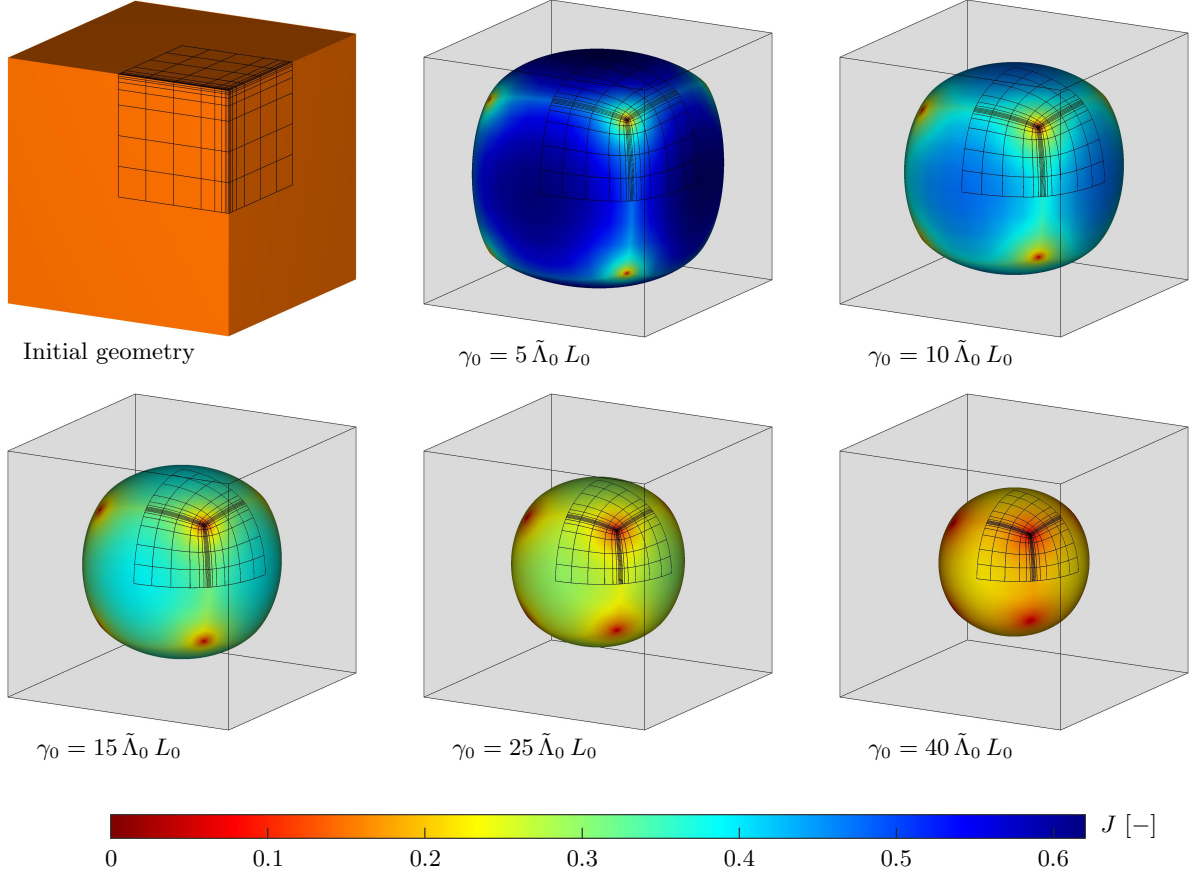


Figure 29: Cube encased by a viscoelastic surface: Deformed cubes at t_{end} for different values of the imposed surface tension γ_0 , colored by the surface stretch J , see Eq. (9.2).

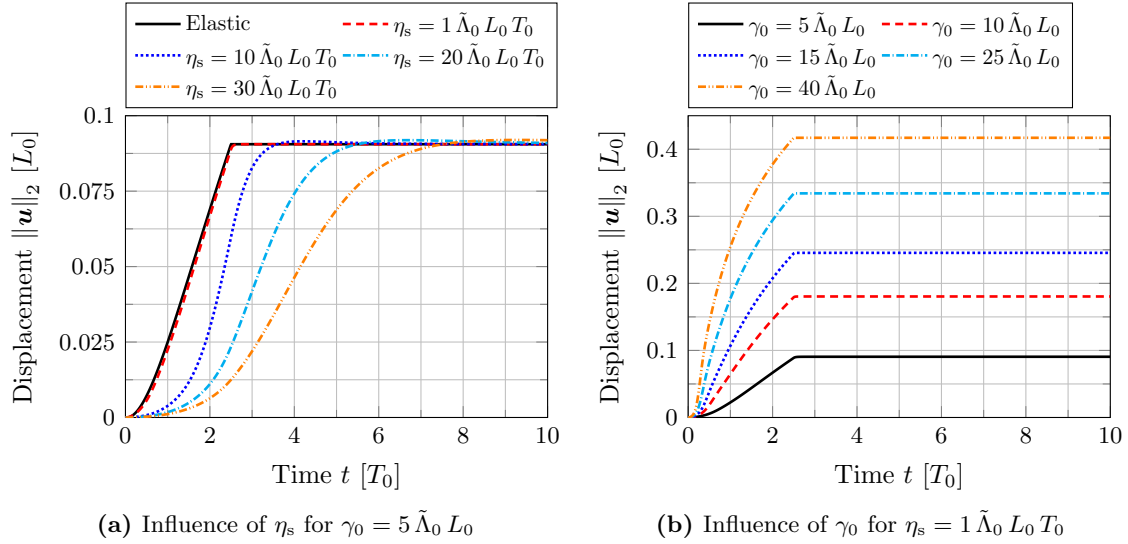


Figure 30: Cube encased by a viscoelastic surface: Displacement norm $\|\mathbf{u}\|_2$ for different values of the in-plane shear viscosity η_s and surface tension γ_0 , measured at the central point of the top surface.

viscous material behavior only for membrane deformations but not for bending, or vice versa. At the same time, the formulation allows to use known 3D material models. The presented formulation also allows to describe boundary viscoelasticity of 3D bodies. Thus, the proposed formulation unifies boundary, membrane and shell viscoelasticity. The use of rotation-free fi-

nite elements and isogeometric shape functions increases efficiency and accuracy in comparison to classical FE discretizations. This increase is greatest when used in conjunction with direct surface-based constitutive models such as are provided here.

In order to avoid problems stemming from ill-conditioned parametrizations noted in Remark 4.3, the ODEs for $\hat{a}^{\alpha\beta}$ can be reformulated, e.g. as ODEs for I_1^{el} , J_{in} , and J_{el} . Also, constant area for the inelastic deformation can be enforced by coupling the evolution laws to the constraint $J_{\text{in}} = 1$, which can be directly plugged into the ODEs to eliminate one of them, or enforced by a Lagrange multiplier approach, for instance.

As the viscoelastic framework introduces a time scale, the quasi-static shell framework can also be extended to incorporate inertia, e.g. to investigate the influence of the viscous effects and inertia on each other. Further, temperature can be introduced in the formulation in order to model the change of temperature as a cause of dissipation. The elastic and viscoelastic material properties can then also be dependent on the temperature.

Acknowledgments

The authors acknowledge funding by the Deutsche Forschungsgemeinschaft (DFG, German Research Foundation) – 333849990/GRK2379 (IRTG Modern Inverse Problems). Simulations were partly performed with computing resources granted by RWTH Aachen University under project rwth0917.

Appendix

A Linearization

A.1 Auxiliary derivatives

For the linearization in Appendix A.2, the derivatives of Eqs. (20.1), (21) and (24.1) w.r.t. $\hat{a}^{\alpha\beta}$ and $\hat{b}_{\alpha\beta}$ are required. They are given by

$$\frac{\partial I_1^{\text{el}}}{\partial \hat{a}^{\alpha\beta}} = a_{\alpha\beta}, \quad \frac{\partial J_{\text{el}}}{\partial \hat{a}^{\alpha\beta}} = \frac{1}{2} J_{\text{el}} \hat{a}_{\alpha\beta}, \quad \frac{\partial \hat{H}}{\partial \hat{a}^{\alpha\beta}} = \frac{1}{2} \hat{b}_{\alpha\beta}, \quad \text{and} \quad \frac{\partial \hat{H}}{\partial \hat{b}_{\alpha\beta}} = \frac{1}{2} \hat{a}^{\alpha\beta}, \quad (123)$$

where $\partial(\det[\hat{a}^{\alpha\beta}])/\partial t = \det[\hat{a}^{\alpha\beta}] \hat{a}_{\gamma\delta} \dot{\hat{a}}^{\gamma\delta}$ has been used.

For the linearization of the stresses in the Maxwell branch, see Appendix A.3, the derivatives of J_{el} , J_{in} , and I_1^{el} w.r.t. $a_{\gamma\delta}$ are required, see Eqs. (20)–(21). They are given by

$$\frac{\partial I_1^{\text{el}}}{\partial a_{\gamma\delta}} = \hat{a}^{\gamma\delta} + \frac{\partial \hat{a}^{\epsilon\zeta}}{\partial a_{\gamma\delta}} a_{\epsilon\zeta}, \quad (124)$$

and

$$\begin{aligned}
\frac{\partial J_{\text{in}}}{\partial a_{\gamma\delta}} &= \frac{\partial J_{\text{in}}}{\partial \hat{a}^{\epsilon\zeta}} \frac{\partial \hat{a}^{\epsilon\zeta}}{\partial a_{\gamma\delta}} = \frac{1}{\sqrt{\det[A_{\alpha\beta}]}} \frac{\partial}{\partial \hat{a}^{\epsilon\zeta}} \left(\frac{1}{\sqrt{\det[\hat{a}^{\alpha\beta}]}} \right) \frac{\partial \hat{a}^{\epsilon\zeta}}{\partial a_{\gamma\delta}} \\
&= -\frac{1}{2} \frac{1}{\sqrt{\det[A_{\alpha\beta}]}} \frac{1}{(\sqrt{\det[\hat{a}^{\alpha\beta}]})^{3/2}} \frac{\partial}{\partial \hat{a}^{\epsilon\zeta}} \left(\det[\hat{a}^{\alpha\beta}] \right) \frac{\partial \hat{a}^{\epsilon\zeta}}{\partial a_{\gamma\delta}} \\
&= -\frac{1}{2} J_{\text{in}} \hat{a}_{\epsilon\zeta} \frac{\partial \hat{a}^{\epsilon\zeta}}{\partial a_{\gamma\delta}},
\end{aligned} \tag{125}$$

as $\partial(\det[\hat{a}^{\alpha\beta}])/\partial \hat{a}^{\epsilon\zeta} = \det[\hat{a}^{\alpha\beta}] \hat{a}_{\epsilon\zeta}$. Likewise,

$$\begin{aligned}
\frac{\partial J_{\text{el}}}{\partial a_{\gamma\delta}} &= \sqrt{\det[\hat{a}^{\alpha\beta}]} \frac{\partial(\sqrt{\det[a_{\alpha\beta}]})}{\partial a_{\gamma\delta}} + \sqrt{\det[a_{\alpha\beta}]} \frac{\partial(\sqrt{\det[\hat{a}^{\alpha\beta}]})}{\partial a_{\gamma\delta}} \\
&= \frac{1}{2} \frac{\sqrt{\det[\hat{a}^{\alpha\beta}]}}{\sqrt{\det[a_{\alpha\beta}]}} \frac{\partial(\det[a_{\alpha\beta}])}{\partial a_{\gamma\delta}} + \frac{1}{2} \frac{\sqrt{\det[a_{\alpha\beta}]}}{\sqrt{\det[\hat{a}^{\alpha\beta}]}} \frac{\partial(\det[\hat{a}^{\alpha\beta}])}{\partial \hat{a}^{\epsilon\zeta}} \frac{\partial \hat{a}^{\epsilon\zeta}}{\partial a_{\gamma\delta}} \\
&= \frac{1}{2} J_{\text{el}} a^{\gamma\delta} + \frac{1}{2} J_{\text{el}} \hat{a}_{\epsilon\zeta} \frac{\partial \hat{a}^{\epsilon\zeta}}{\partial a_{\gamma\delta}},
\end{aligned} \tag{126}$$

as $\partial(\det[a_{\alpha\beta}])/\partial a_{\gamma\delta} = \det[a_{\alpha\beta}] a^{\gamma\delta}$. The derivatives of the mean curvature \hat{H} , see Eq. (24.1), w.r.t. $a_{\gamma\delta}$ and $b_{\gamma\delta}$ are given by

$$\frac{\partial \hat{H}}{\partial a_{\gamma\delta}} = \frac{1}{2} \left(\frac{\partial \hat{a}^{\epsilon\zeta}}{\partial a_{\gamma\delta}} \hat{b}_{\epsilon\zeta} + \hat{a}^{\epsilon\zeta} \frac{\partial \hat{b}_{\epsilon\zeta}}{\partial a_{\gamma\delta}} \right), \quad \text{and} \quad \frac{\partial \hat{H}}{\partial b_{\gamma\delta}} = \frac{1}{2} \left(\frac{\partial \hat{a}^{\epsilon\zeta}}{\partial b_{\gamma\delta}} \hat{b}_{\epsilon\zeta} + \hat{a}^{\epsilon\zeta} \frac{\partial \hat{b}_{\epsilon\zeta}}{\partial b_{\gamma\delta}} \right). \tag{127}$$

For the derivatives in Eqs. (124)–(127), the derivatives of $\hat{a}^{\epsilon\zeta}$ and $\hat{b}_{\epsilon\zeta}$ w.r.t. $a_{\gamma\delta}$ and $b_{\gamma\delta}$ need to be computed, due to the elimination noted in Remark 4.4. The derivation of these derivatives depends on the employed material model and is presented in Appendix A.3. Further, the following derivatives are used in the subsequent sections (Sauer, 2018)

$$\begin{aligned}
a^{\alpha\beta\gamma\delta} &:= \frac{\partial a^{\alpha\beta}}{\partial a_{\gamma\delta}} = -\frac{1}{2} (a^{\alpha\gamma} a^{\beta\delta} + a^{\alpha\delta} a^{\beta\gamma}), \\
\hat{a}^{\alpha\beta\gamma\delta} &:= \frac{\partial \hat{a}^{\alpha\beta}}{\partial \hat{a}_{\gamma\delta}} = -\frac{1}{2} (\hat{a}^{\alpha\gamma} \hat{a}^{\beta\delta} + \hat{a}^{\alpha\delta} \hat{a}^{\beta\gamma}), \quad \text{and} \\
b^{\alpha\beta\gamma\delta} &:= \frac{\partial b^{\alpha\beta}}{\partial a_{\gamma\delta}} = -\frac{1}{2} (a^{\alpha\gamma} b^{\beta\delta} + b^{\alpha\gamma} a^{\beta\delta} + a^{\alpha\delta} b^{\beta\gamma} + b^{\alpha\delta} a^{\beta\gamma}),
\end{aligned} \tag{128}$$

from which $\partial b^{\alpha\beta}/\partial b_{\gamma\delta} = -a^{\alpha\beta\gamma\delta}$ follows.

A.2 Linearization for the implicit Euler scheme

For the time integration of the evolution laws based on the implicit Euler scheme, the derivatives in Eq. (80) are required for the different material models. Subsequently, those derivatives are reported.

A.2.1 Koiter membrane model

The derivative of Eq. (83) w.r.t. $\hat{a}^{\alpha\beta}$ is given by

$$\frac{\partial \hat{\mathbf{g}}_{\text{s}}^{\alpha\beta}}{\partial \hat{a}^{\gamma\delta}} = \frac{1}{\Delta t} \delta_{\gamma}^{\alpha} \delta_{\delta}^{\beta} + \frac{\Lambda_1}{2 \eta_{\text{s}}} \left(\hat{a}^{\alpha\beta} a_{\gamma\delta} + (I_1^{\text{el}} - 2) \delta_{\gamma}^{\alpha} \delta_{\delta}^{\beta} \right) + \frac{\mu_1}{\eta_{\text{s}}} \left(a_{\delta\epsilon} (\delta_{\gamma}^{\alpha} \hat{a}^{\beta\epsilon} + \delta_{\gamma}^{\beta} \hat{a}^{\alpha\epsilon}) - \delta_{\gamma}^{\alpha} \delta_{\delta}^{\beta} \right), \tag{129}$$

with Kronecker delta δ_β^α .

A.2.2 Neo-Hookean membrane model with dilatational/deviatoric split

The derivative of Eq. (86) w.r.t. $\hat{a}^{\alpha\beta}$ is given by

$$\frac{\partial \hat{\mathbf{g}}_s^{\alpha\beta}}{\partial \hat{a}^{\gamma\delta}} = \frac{1}{\Delta t} \delta_\gamma^\alpha \delta_\delta^\beta + \frac{K_1}{2\eta_s} J_{\text{el}}^2 a^{\alpha\beta} \hat{a}_{\gamma\delta} + \frac{\mu_1}{2\eta_s J_{\text{el}}} \left(2 \delta_\gamma^\alpha \delta_\delta^\beta - a^{\alpha\beta} a_{\gamma\delta} - \hat{a}^{\alpha\beta} \hat{a}_{\gamma\delta} + \frac{1}{2} I_1^{\text{el}} a^{\alpha\beta} \hat{a}_{\gamma\delta} \right), \quad (130)$$

with $[\hat{a}_{\alpha\beta}] = [\hat{a}^{\alpha\beta}]^{-1}$ and Kronecker delta δ_β^α .

A.2.3 Incompressible Neo-Hookean membrane model

The derivative of Eq. (87) w.r.t. $\hat{a}^{\gamma\delta}$ is given by

$$\frac{\partial \hat{\mathbf{g}}_s^{\alpha\beta}}{\partial \hat{a}^{\gamma\delta}} = \frac{1}{\Delta t} \delta_\gamma^\alpha \delta_\delta^\beta + \frac{\mu_1}{\eta_s} \left(\delta_\gamma^\alpha \delta_\delta^\beta + \frac{a^{\alpha\beta}}{J_{\text{el}}^2} \hat{a}_{\gamma\delta} \right), \quad (131)$$

with $[\hat{a}_{\alpha\beta}] = [\hat{a}^{\alpha\beta}]^{-1}$ and Kronecker delta δ_β^α .

A.2.4 Membranes with constant surface tension

The derivative of Eq. (88) w.r.t. $\hat{a}^{\gamma\delta}$ is given by

$$\frac{\partial \hat{\mathbf{g}}_s^{\alpha\beta}}{\partial \hat{a}^{\gamma\delta}} = \frac{1}{\Delta t} \delta_\gamma^\alpha \delta_\delta^\beta + \frac{\hat{\gamma}}{2\eta_s} J_{\text{el}} a^{\alpha\beta} \hat{a}_{\gamma\delta}, \quad (132)$$

with $[\hat{a}_{\alpha\beta}] = [\hat{a}^{\alpha\beta}]^{-1}$ and Kronecker delta δ_β^α .

A.2.5 Helfrich bending model

The derivatives of Eqs. (91)–(92) w.r.t. $\hat{a}^{\gamma\delta}$ and $\hat{b}_{\gamma\delta}$ are given by

$$\begin{aligned} \frac{\partial \hat{\mathbf{g}}_s^{\alpha\beta}}{\partial \hat{a}^{\gamma\delta}} &= \frac{1}{\Delta t} \delta_\gamma^\alpha \delta_\delta^\beta + \frac{k_1 J_{\text{el}}}{\eta_s} \left[\left(\frac{1}{2} \Delta H^2 a^{\alpha\beta} - \Delta H b^{\alpha\beta} \right) \hat{a}_{\gamma\delta} - \left(\Delta H a^{\alpha\beta} - b^{\alpha\beta} \right) \hat{b}_{\gamma\delta} \right], \\ \frac{\partial \hat{\mathbf{g}}_s^{\alpha\beta}}{\partial \hat{b}_{\gamma\delta}} &= -\frac{k_1 J_{\text{el}}}{\eta_s} \left(\Delta H a^{\alpha\beta} - b^{\alpha\beta} \right) \hat{a}^{\gamma\delta}, \end{aligned} \quad (133)$$

and

$$\begin{aligned} \frac{\partial \hat{\mathbf{g}}_{\alpha\beta}^{\text{b}}}{\partial \hat{a}^{\gamma\delta}} &= -\frac{k_1 J_{\text{el}}}{\eta_b} a_{\alpha\beta} \left(\Delta H \hat{a}_{\gamma\delta} - \hat{b}_{\gamma\delta} \right), \\ \frac{\partial \hat{\mathbf{g}}_{\alpha\beta}^{\text{b}}}{\partial \hat{b}_{\gamma\delta}} &= \frac{1}{\Delta t} \delta_\gamma^\alpha \delta_\delta^\beta + \frac{k_1 J_{\text{el}}}{2\eta_b} a_{\alpha\beta} \hat{a}^{\gamma\delta}, \end{aligned} \quad (134)$$

with $[\hat{a}_{\alpha\beta}] = [\hat{a}^{\alpha\beta}]^{-1}$, Kronecker delta δ_β^α , and $\Delta H := H - \hat{H}$.

A.3 Linearization for the finite element method

Subsequently, the additional contributions in the tangent matrices, see Eqs. (97)–(98), coming from the Maxwell branch are derived for the employed material models.

A.3.1 Koiter membrane model

Given the stresses in Eq. (35),⁹ the contribution in the linearized weak form is

$$\begin{aligned}
c_1^{\alpha\beta\gamma\delta} &= 2 \frac{\partial \tau_{1(\text{el})}^{\alpha\beta}}{\partial a_{\gamma\delta}} \\
&= \Lambda_1 \frac{\partial J_{\text{in}}}{\partial a_{\gamma\delta}} (I_1^{\text{el}} - 2) \hat{a}^{\alpha\beta} + \Lambda_1 J_{\text{in}} \left(\frac{\partial I_1^{\text{el}}}{\partial a_{\gamma\delta}} \hat{a}^{\alpha\beta} + (I_1^{\text{el}} - 2) \frac{\partial \hat{a}^{\alpha\beta}}{\partial a_{\gamma\delta}} \right) \\
&\quad + 2 \mu_1 \frac{\partial J_{\text{in}}}{\partial a_{\gamma\delta}} (\hat{a}^{\alpha\epsilon} a_{\epsilon\zeta} \hat{a}^{\beta\zeta} - \hat{a}^{\alpha\beta}) \\
&\quad + 2 \mu_1 J_{\text{in}} \left(\frac{\partial \hat{a}^{\alpha\epsilon}}{\partial a_{\gamma\delta}} a_{\epsilon\zeta} \hat{a}^{\beta\zeta} + \frac{1}{2} (\hat{a}^{\alpha\gamma} \hat{a}^{\beta\delta} + \hat{a}^{\alpha\delta} \hat{a}^{\beta\gamma}) + \hat{a}^{\alpha\epsilon} a_{\epsilon\zeta} \frac{\partial \hat{a}^{\beta\zeta}}{\partial a_{\gamma\delta}} - \frac{\partial \hat{a}^{\alpha\beta}}{\partial a_{\gamma\delta}} \right).
\end{aligned} \tag{135}$$

Still, the derivative $\partial \hat{a}^{\alpha\beta} / \partial a_{\gamma\delta}$ needs to be found to evaluate Eq. (135). For this, the nonlinear equations in Eq. (83), which need to be solved for $\hat{a}^{\alpha\beta}$ within the element routine at each quadrature point and each time step, need to be differentiated w.r.t. $a_{\gamma\delta}$. The auxiliary arrays

$$\hat{\mathbf{a}}_{\text{con}} := \begin{bmatrix} \hat{a}^{11} \\ \hat{a}^{12} \\ \hat{a}^{21} \\ \hat{a}^{22} \end{bmatrix}, \quad \hat{\mathbf{a}}_{\text{co}} := \begin{bmatrix} \hat{a}_{11} \\ \hat{a}_{12} \\ \hat{a}_{21} \\ \hat{a}_{22} \end{bmatrix}, \quad \mathbf{a}_{\text{con}} := \begin{bmatrix} a^{11} \\ a^{12} \\ a^{21} \\ a^{22} \end{bmatrix}, \quad \text{and} \quad \mathbf{a}_{\text{co}} := \begin{bmatrix} a_{11} \\ a_{12} \\ a_{21} \\ a_{22} \end{bmatrix}, \tag{136}$$

are defined to simplify the notation. The required derivatives $\partial \hat{a}^{\alpha\beta} / \partial a_{\gamma\delta}$ can then be extracted from the (4×4) -matrix

$$\frac{\partial \hat{\mathbf{a}}_{\text{con}}}{\partial \mathbf{a}_{\text{co}}} = \begin{bmatrix} \partial \hat{a}^{11} / \partial a_{11} & \partial \hat{a}^{11} / \partial a_{12} & \partial \hat{a}^{11} / \partial a_{21} & \partial \hat{a}^{11} / \partial a_{22} \\ \partial \hat{a}^{12} / \partial a_{11} & \partial \hat{a}^{12} / \partial a_{12} & \partial \hat{a}^{12} / \partial a_{21} & \partial \hat{a}^{12} / \partial a_{22} \\ \partial \hat{a}^{21} / \partial a_{11} & \partial \hat{a}^{21} / \partial a_{12} & \partial \hat{a}^{21} / \partial a_{21} & \partial \hat{a}^{21} / \partial a_{22} \\ \partial \hat{a}^{22} / \partial a_{11} & \partial \hat{a}^{22} / \partial a_{12} & \partial \hat{a}^{22} / \partial a_{21} & \partial \hat{a}^{22} / \partial a_{22} \end{bmatrix}, \tag{137}$$

which follows from the solution of

$$\left[\left(\frac{\eta_s}{\Delta t} - \mu_1 + \frac{\Lambda_1}{2} (I_1^{\text{el}} - 2) \right) \mathbf{I}_4 + \frac{\Lambda_1}{2} \hat{\mathbf{a}}_{\text{con}} \mathbf{a}_{\text{co}}^{\text{T}} + \mu_1 \tilde{\mathbf{C}} \right] \frac{\partial \hat{\mathbf{a}}_{\text{con}}}{\partial \mathbf{a}_{\text{co}}} = -\frac{\Lambda_1}{2} \hat{\mathbf{a}}_{\text{con}} \hat{\mathbf{a}}_{\text{con}}^{\text{T}} + \mu_1 \frac{\partial \hat{\mathbf{a}}_{\text{con}}}{\partial \hat{\mathbf{a}}_{\text{co}}}, \tag{138}$$

where \mathbf{I}_4 denotes the (4×4) -identity matrix. The derivative $\partial \hat{\mathbf{a}}_{\text{con}} / \partial \hat{\mathbf{a}}_{\text{co}}$ follows from Eq. (128.2) and it is arranged in analogy to Eq. (137). The matrix $\tilde{\mathbf{C}}$ is given by

$$\tilde{\mathbf{C}} := \begin{bmatrix} 2 c_1^1 & 2 c_2^1 & 0 & 0 \\ c_1^2 & c_2^2 & c_1^1 & c_2^1 \\ c_1^2 & c_2^2 & c_1^1 & c_2^1 \\ 0 & 0 & 2 c_1^2 & 2 c_2^2 \end{bmatrix}, \tag{139}$$

with $c_\gamma^\alpha := \hat{a}^{\alpha\beta} a_{\beta\gamma}$.

⁹with the modifications mentioned in Remark 3.2

Remark A.1: Note that the computation of the derivatives $\partial\hat{a}^{\alpha\beta}/\partial a_{\gamma\delta}$ can become more efficient by exploiting the symmetries of $\hat{a}^{\alpha\beta}$ and $a_{\alpha\beta}$, e.g. $\hat{a}^{12} = \hat{a}^{21}$ and $a_{12} = a_{21}$. The (4×4) -matrix in Eq. (137) can then be reduced to a (3×3) -matrix, such that also the dimension of the linear system of equations in Eq. (138) decreases.

A.3.2 Neo-Hookean membrane model

Considering the stresses in Eq. (37) with $\Lambda = 0$,⁹ the corresponding linearization is

$$c_1^{\alpha\beta\gamma\delta} = 2 \frac{\partial\tau_{1(\text{el})}^{\alpha\beta}}{\partial a_{\gamma\delta}} = 2\mu_1 \left[\frac{\partial J_{\text{in}}}{\partial a_{\gamma\delta}} (\hat{a}^{\alpha\beta} - a^{\alpha\beta}) + J_{\text{in}} \left(\frac{\partial\hat{a}^{\alpha\beta}}{\partial a_{\gamma\delta}} - a^{\alpha\beta\gamma\delta} \right) \right], \quad (140)$$

where

$$\frac{\partial\hat{a}^{\alpha\beta}}{\partial a_{\gamma\delta}} = \frac{\mu_1 \Delta t}{\eta_s + \mu_1 \Delta t} a^{\alpha\beta\gamma\delta}, \quad (141)$$

see also Eq. (85). Note that if $\eta_s/\Delta t \rightarrow 0$, the derivative in Eq. (141) approaches $a^{\alpha\beta\gamma\delta}$, and for $\eta_s/\Delta t \rightarrow \infty$ it approaches zero.

A.3.3 Neo-Hookean membrane model with dilatational/deviatoric split

Given the stress in Eq. (39),⁹ the contribution in the linearized weak form is

$$\begin{aligned} c_1^{\alpha\beta\gamma\delta} = 2 \frac{\partial\tau_{1(\text{el})}^{\alpha\beta}}{\partial a_{\gamma\delta}} &= K_1 \left[\frac{\partial J_{\text{in}}}{\partial a_{\gamma\delta}} (J_{\text{el}}^2 - 1) a^{\alpha\beta} + 2J \frac{\partial J_{\text{el}}}{\partial a_{\gamma\delta}} a^{\alpha\beta} + J_{\text{in}} (J_{\text{el}}^2 - 1) a^{\alpha\beta\gamma\delta} \right] \\ &+ \mu_1 \left[-\frac{J_{\text{in}}}{J_{\text{el}}^2} \frac{\partial J_{\text{el}}}{\partial a_{\gamma\delta}} (2\hat{a}^{\alpha\beta} - I_1^{\text{el}} a^{\alpha\beta}) + \frac{1}{J_{\text{el}}} \frac{\partial J_{\text{in}}}{\partial a_{\gamma\delta}} (2\hat{a}^{\alpha\beta} - I_1^{\text{el}} a^{\alpha\beta}) \right. \\ &\left. + \frac{J_{\text{in}}}{J_{\text{el}}} \left(2 \frac{\partial\hat{a}^{\alpha\beta}}{\partial a_{\gamma\delta}} - \frac{\partial I_1^{\text{el}}}{\partial a_{\gamma\delta}} a^{\alpha\beta} - I_1^{\text{el}} a^{\alpha\beta\gamma\delta} \right) \right]. \end{aligned} \quad (142)$$

Still, the derivative $\partial\hat{a}^{\alpha\beta}/\partial a_{\gamma\delta}$ needs to be found to evaluate Eq. (142). For this, the nonlinear equations from Eq. (86), which need to be solved for $\hat{a}^{\alpha\beta}$ in the element routine at each quadrature point and each time step, need to be differentiated w.r.t. $a_{\gamma\delta}$. Similar to Eq. (138), the required derivatives $\partial\hat{a}^{\alpha\beta}/\partial a_{\gamma\delta}$ can be extracted from the (4×4) -matrix $\partial\hat{\mathbf{a}}_{\text{con}}/\partial\mathbf{a}_{\text{co}}$, see Eq. (137), which follows from the solution of

$$\begin{aligned} &\left[\left(\frac{2\eta_s}{\Delta t} + \frac{2\mu_1}{J_{\text{el}}} \right) \mathbf{I}_4 + \left(K_1 J_{\text{el}}^2 + \frac{\mu_1 I_1^{\text{el}}}{2J_{\text{el}}} \right) \mathbf{a}_{\text{con}} \hat{\mathbf{a}}_{\text{co}}^{\text{T}} - \frac{\mu_1}{J_{\text{el}}} \left(\hat{\mathbf{a}}_{\text{con}} \hat{\mathbf{a}}_{\text{co}}^{\text{T}} + \mathbf{a}_{\text{con}} \mathbf{a}_{\text{co}}^{\text{T}} \right) \right] \frac{\partial\hat{\mathbf{a}}_{\text{con}}}{\partial\mathbf{a}_{\text{co}}} \\ &= -K_1 \left(J_{\text{el}}^2 \mathbf{a}_{\text{con}} \mathbf{a}_{\text{co}}^{\text{T}} + (J_{\text{el}}^2 - 1) \frac{\partial\mathbf{a}_{\text{con}}}{\partial\mathbf{a}_{\text{co}}} \right) \\ &\quad + \frac{\mu_1}{J_{\text{el}}} \left(\mathbf{a}_{\text{con}} \hat{\mathbf{a}}_{\text{con}}^{\text{T}} + I_1^{\text{el}} \frac{\partial\mathbf{a}_{\text{con}}}{\partial\mathbf{a}_{\text{co}}} + \hat{\mathbf{a}}_{\text{con}} \mathbf{a}_{\text{con}}^{\text{T}} - \frac{I_1^{\text{el}}}{2} \mathbf{a}_{\text{con}} \mathbf{a}_{\text{co}}^{\text{T}} \right), \end{aligned} \quad (143)$$

where \mathbf{I}_4 denotes the (4×4) -identity matrix. The derivative $\partial\mathbf{a}_{\text{con}}/\partial\mathbf{a}_{\text{co}}$ follows from Eq. (128.1) and it is arranged in analogy to Eq. (137).

A.3.4 Incompressible Neo-Hookean membrane model

Given the stresses in Eq. (41),⁹ the contribution in the linearized weak form is

$$c_1^{\alpha\beta\gamma\delta} = 2 \frac{\partial \tau_1^{\alpha\beta}}{\partial a_{\gamma\delta}} = 2 \mu_1 \left[\frac{\partial J_{\text{in}}}{\partial a_{\gamma\delta}} \left(\hat{a}^{\alpha\beta} - \frac{a^{\alpha\beta}}{J_{\text{el}}^2} \right) + J_{\text{in}} \left(\frac{\partial \hat{a}^{\alpha\beta}}{\partial a_{\gamma\delta}} - \frac{a^{\alpha\beta\gamma\delta}}{J_{\text{el}}^2} + 2 \frac{a^{\alpha\beta}}{J_{\text{el}}^3} \frac{\partial J_{\text{el}}}{\partial a_{\gamma\delta}} \right) \right]. \quad (144)$$

The required derivative $\partial \hat{a}^{\alpha\beta} / \partial a_{\gamma\delta}$ is extracted from the (4×4) -matrix $\partial \hat{\mathbf{a}}_{\text{con}} / \partial \mathbf{a}_{\text{co}}$, see Eq. (137), which follows from the solution of

$$\left[\left(\frac{\eta_s}{\Delta t} + \mu_1 \right) \mathbf{I}_4 + \frac{\mu_1}{J_{\text{el}}^2} \mathbf{a}_{\text{con}} \hat{\mathbf{a}}_{\text{co}}^{\text{T}} \right] \frac{\partial \hat{\mathbf{a}}_{\text{con}}}{\partial \mathbf{a}_{\text{co}}} = \frac{\mu_1}{J_{\text{el}}^2} \left(\frac{\partial \mathbf{a}_{\text{con}}}{\partial \mathbf{a}_{\text{co}}} - \mathbf{a}_{\text{con}} \mathbf{a}_{\text{con}}^{\text{T}} \right), \quad (145)$$

where \mathbf{I}_4 denotes the (4×4) -identity matrix. The derivative $\partial \mathbf{a}_{\text{con}} / \partial \mathbf{a}_{\text{co}}$ follows from Eq. (128.1) and it is arranged in analogy to Eq. (137).

A.3.5 Membranes with constant surface tension

Given the stresses in Eq. (43),⁹ the contribution in the linearized weak form is

$$c_1^{\alpha\beta\gamma\delta} = 2 \frac{\partial \tau_1^{\alpha\beta}}{\partial a_{\gamma\delta}} = \hat{\gamma} J (a^{\alpha\beta} a^{\gamma\delta} + 2 a^{\alpha\beta\gamma\delta}). \quad (146)$$

A.3.6 Koiter bending model

For the moment components given in Eq. (45),⁹ the material tangent is given by

$$f_1^{\alpha\beta\gamma\delta} = \frac{\partial M_{0(1)(\text{el})}^{\alpha\beta}}{\partial b_{\gamma\delta}} = J_{\text{in}} \hat{f}^{\alpha\beta\gamma\delta} \frac{\eta_b}{\eta_b + c_1 \Delta t}, \quad (147)$$

as the derivative $\partial \hat{b}_{\alpha\beta} / \partial b_{\gamma\delta}$ follows in analogy to Eq. (141).

A.3.7 Helfrich bending model

Given the stress and moment components in Eqs. (47)–(48) with $k^* = 0$,⁹ the material tangents in Eq. (97) follow as

$$\begin{aligned} c_1^{\alpha\beta\gamma\delta} &= 2 k_1 J \left(\left(\frac{1}{2} \Delta H^2 a^{\alpha\beta} - \Delta H b^{\alpha\beta} \right) a^{\gamma\delta} \right. \\ &\quad \left. + \left(\Delta H a^{\alpha\beta} - b^{\alpha\beta} \right) \Delta H_a^{\gamma\delta} + \Delta H^2 a^{\alpha\beta\gamma\delta} - 2 \Delta H b^{\alpha\beta\gamma\delta} \right), \\ d_1^{\alpha\beta\gamma\delta} &= k_1 J \left(\left(\Delta H a^{\alpha\beta} - b^{\alpha\beta} \right) \Delta H_b^{\gamma\delta} + 2 \Delta H a^{\alpha\beta\gamma\delta} \right), \\ e_1^{\alpha\beta\gamma\delta} &= k_1 J \left(\Delta H a^{\alpha\beta} a^{\gamma\delta} + \Delta H_a^{\gamma\delta} a^{\alpha\beta} + 2 \Delta H a^{\alpha\beta\gamma\delta} \right), \\ f_1^{\alpha\beta\gamma\delta} &= \frac{k_1 J}{2} \Delta H_b^{\gamma\delta} a^{\alpha\beta}, \end{aligned} \quad (148)$$

where $\Delta H := H - \hat{H}$ and

$$\Delta H_a^{\gamma\delta} := -b^{\gamma\delta} - \frac{\partial \hat{a}^{\epsilon\zeta}}{\partial a_{\gamma\delta}} \hat{b}_{\epsilon\zeta} - \hat{a}^{\epsilon\zeta} \frac{\partial \hat{b}_{\epsilon\zeta}}{\partial a_{\gamma\delta}}, \quad \text{and} \quad \Delta H_b^{\gamma\delta} := a^{\gamma\delta} - \frac{\partial \hat{a}^{\epsilon\zeta}}{\partial b_{\gamma\delta}} \hat{b}_{\epsilon\zeta} - \hat{a}^{\epsilon\zeta} \frac{\partial \hat{b}_{\epsilon\zeta}}{\partial b_{\gamma\delta}}. \quad (149)$$

Still, the derivatives of $\hat{a}^{\epsilon\zeta}$ and $\hat{b}_{\epsilon\zeta}$ w.r.t. $a_{\gamma\delta}$ and $b_{\gamma\delta}$ are required. For this, the nonlinear algebraic equations from Eqs. (91)–(92) are differentiated w.r.t. $a_{\gamma\delta}$ and $b_{\gamma\delta}$. In analogy to Eq. (136), the auxiliary arrays

$$\hat{\mathbf{b}}_{\text{con}} := \begin{bmatrix} \hat{b}^{11} \\ \hat{b}^{12} \\ \hat{b}^{21} \\ \hat{b}^{22} \end{bmatrix}, \quad \hat{\mathbf{b}}_{\text{co}} := \begin{bmatrix} \hat{b}_{11} \\ \hat{b}_{12} \\ \hat{b}_{21} \\ \hat{b}_{22} \end{bmatrix}, \quad \mathbf{b}_{\text{con}} := \begin{bmatrix} b^{11} \\ b^{12} \\ b^{21} \\ b^{22} \end{bmatrix}, \quad \text{and} \quad \mathbf{b}_{\text{co}} := \begin{bmatrix} b_{11} \\ b_{12} \\ b_{21} \\ b_{22} \end{bmatrix}, \quad (150)$$

are defined to simplify the notation. The required derivatives are then obtained by solving

$$\begin{bmatrix} \partial \hat{\mathbf{g}}_s / \partial \mathbf{a}_{\text{co}} \\ \partial \hat{\mathbf{g}}_s / \partial \mathbf{b}_{\text{co}} \\ \partial \hat{\mathbf{g}}^b / \partial \mathbf{a}_{\text{co}} \\ \partial \hat{\mathbf{g}}^b / \partial \mathbf{b}_{\text{co}} \end{bmatrix} = \mathbf{0}, \quad (151)$$

for the unknown derivatives. The resulting linear equation system is given by

$$\begin{bmatrix} \mathbf{A}_{11} & \mathbf{0} & \mathbf{A}_{13} & \mathbf{0} \\ \mathbf{0} & \mathbf{A}_{22} & \mathbf{0} & \mathbf{A}_{24} \\ \mathbf{A}_{31} & \mathbf{0} & \mathbf{A}_{33} & \mathbf{0} \\ \mathbf{0} & \mathbf{A}_{42} & \mathbf{0} & \mathbf{A}_{44} \end{bmatrix} \begin{bmatrix} \partial \hat{\mathbf{a}}_{\text{con}} / \partial \mathbf{a}_{\text{co}} \\ \partial \hat{\mathbf{a}}_{\text{con}} / \partial \mathbf{b}_{\text{co}} \\ \partial \hat{\mathbf{b}}_{\text{co}} / \partial \mathbf{a}_{\text{co}} \\ \partial \hat{\mathbf{b}}_{\text{co}} / \partial \mathbf{b}_{\text{co}} \end{bmatrix} = \begin{bmatrix} \mathbf{r}_1 \\ \mathbf{r}_2 \\ \mathbf{r}_3 \\ \mathbf{r}_4 \end{bmatrix}, \quad (152)$$

with the (4×4) -tangent matrix blocks

$$\begin{aligned} \mathbf{A}_{11} &:= \frac{\eta_s}{k_1 \Delta t J_{\text{el}}} \mathbf{I}_4 + \mathbf{c}_{\text{con}} \hat{\mathbf{a}}_{\text{co}}^{\text{T}} - \mathbf{d}_{\text{con}} \hat{\mathbf{b}}_{\text{co}}^{\text{T}}, & \mathbf{A}_{13} &:= -\mathbf{d}_{\text{con}} \hat{\mathbf{a}}_{\text{con}}^{\text{T}}, \\ \mathbf{A}_{22} &:= \frac{\eta_s}{k_1 \Delta t J_{\text{el}}} \mathbf{I}_4 - \mathbf{d}_{\text{con}} \hat{\mathbf{b}}_{\text{co}}^{\text{T}}, & \mathbf{A}_{24} &:= -\mathbf{d}_{\text{con}} \hat{\mathbf{a}}_{\text{con}}^{\text{T}}, \\ \mathbf{A}_{31} &:= -\frac{1}{2} \left(\Delta H \mathbf{a}_{\text{co}} \hat{\mathbf{a}}_{\text{co}}^{\text{T}} - \mathbf{a}_{\text{co}} \hat{\mathbf{b}}_{\text{co}}^{\text{T}} \right), & \mathbf{A}_{33} &:= \frac{\eta_b}{k_1 \Delta t J_{\text{el}}} \mathbf{I}_4 + \frac{1}{2} \mathbf{a}_{\text{co}} \hat{\mathbf{a}}_{\text{con}}^{\text{T}}, \\ \mathbf{A}_{42} &:= \frac{1}{2} \mathbf{a}_{\text{co}} \hat{\mathbf{b}}_{\text{co}}^{\text{T}}, & \mathbf{A}_{44} &:= \frac{\eta_b}{k_1 \Delta t J_{\text{el}}} \mathbf{I}_4 + \frac{1}{2} \mathbf{a}_{\text{co}} \hat{\mathbf{a}}_{\text{con}}^{\text{T}}, \end{aligned} \quad (153)$$

and the (4×4) -right-hand-side blocks

$$\begin{aligned} \mathbf{r}_1 &:= -\mathbf{c}_{\text{con}} \mathbf{a}_{\text{con}}^{\text{T}} + \mathbf{d}_{\text{con}} \mathbf{b}_{\text{con}}^{\text{T}} - \Delta H^2 \frac{\partial \mathbf{a}_{\text{con}}}{\partial \mathbf{a}_{\text{co}}} + 2 \Delta H \frac{\partial \mathbf{b}_{\text{con}}}{\partial \mathbf{b}_{\text{co}}}, \\ \mathbf{r}_2 &:= -\mathbf{d}_{\text{con}} \mathbf{a}_{\text{con}}^{\text{T}} + 2 \Delta H \frac{\partial \mathbf{b}_{\text{con}}}{\partial \mathbf{b}_{\text{co}}}, \\ \mathbf{r}_3 &:= \frac{1}{2} \Delta H \mathbf{a}_{\text{co}} \mathbf{a}_{\text{con}}^{\text{T}} - \frac{1}{2} \mathbf{a}_{\text{co}} \mathbf{b}_{\text{con}}^{\text{T}} + \Delta H \mathbf{I}_4, \\ \mathbf{r}_4 &:= \frac{1}{2} \mathbf{a}_{\text{co}} \mathbf{a}_{\text{con}}^{\text{T}}, \end{aligned} \quad (154)$$

where

$$\mathbf{c}_{\text{con}} := \frac{1}{2} \left(\Delta H^2 \mathbf{a}_{\text{con}} - 2 \Delta H \mathbf{b}_{\text{con}} \right), \quad \text{and} \quad \mathbf{d}_{\text{con}} := \Delta H \mathbf{a}_{\text{con}} - \mathbf{b}_{\text{con}}. \quad (155)$$

Here, the (4×4) -identity matrix is denoted \mathbf{I}_4 and the derivatives $\partial \mathbf{a}_{\text{con}} / \partial \mathbf{a}_{\text{co}}$, $\partial \mathbf{b}_{\text{con}} / \partial \mathbf{a}_{\text{co}}$ and $\partial \mathbf{b}_{\text{con}} / \partial \mathbf{b}_{\text{co}}$ follow from Eq. (128) and they are arranged in analogy to Eq. (137).

B Analytical solutions

B.1 Inflated membrane balloon

This appendix derives the analytical solution for the inflated spherical membrane example from Sec. 5.2, see also Eqs. (103)–(105). The two contributions $p_{\text{el}}(t)$ and $p_{\text{visc}}(t)$ are derived subsequently.

B.1.1 Pressure from the elastic branch

The elastic behavior of rubber can be described by the incompressible Neo-Hookean material model from Eq. (41). For the inflated balloon, the current radius r is related to the initial radius R via the stretch λ , i.e. $r = \lambda R$. As $d\mathbf{x} = \mathbf{F} d\mathbf{X}$, the surface deformation gradient becomes $\mathbf{F} = \lambda \mathbf{i}$. The left surface Cauchy-Green tensor then becomes $\mathbf{B} = \mathbf{F}\mathbf{F}^T = \lambda^2 \mathbf{i}$. The surface stretch, which is related to the area change, i.e. $da = J dA$, is given by $J = \lambda^2$. Finally, the incompressibility of the material results in the relation $\tilde{t} = T/J$ between the current and initial thickness.

Using these kinematic relations, Eq. (41), and the plane stress condition $\sigma_{33} = 0$, the stress tensor becomes

$$\tilde{\boldsymbol{\sigma}} = \frac{\boldsymbol{\sigma}}{\tilde{t}} + \sigma_{33} (\mathbf{n} \otimes \mathbf{n}) = \frac{1}{\tilde{t}} \frac{\mu}{J} \left(\mathbf{B} - \frac{\mathbf{i}}{J^2} \right) = \frac{1}{\tilde{t}} \frac{\mu}{\lambda^2} \left(\lambda^2 \mathbf{i} - \frac{\mathbf{i}}{\lambda^4} \right) = \frac{\mu}{\tilde{t}} \left(1 - \frac{1}{\lambda^6} \right) \mathbf{i}. \quad (156)$$

As derived in Needleman (1977), the in-plane normal stress in Eq. (156) is equal to $\tilde{\sigma} = p_{\text{el}} r/2/\tilde{t}$, which leads to the pressure-stretch or pressure-volume relation from Eq. (104). The surface tension, see Eq. (30.1), is then given by $\gamma = \mu(1 - \lambda^{-6})$.

B.1.2 Solution of the evolution laws

To determine the Maxwell stresses, the intermediate configuration needs to be fully specified. For this, the evolution laws

$$\dot{\hat{a}}^{\alpha\beta} + \frac{\mu_1}{\eta_s} \hat{a}^{\alpha\beta} = \frac{\mu_1}{\eta_s} a^{\alpha\beta}(t), \quad \hat{a}^{\alpha\beta}(t=0) = A^{\alpha\beta}, \quad (157)$$

need to be solved, see Eq. (56). Based on the kinematic relations

$$\hat{a}_{\alpha\beta} = J_{\text{in}} A_{\alpha\beta}, \quad \hat{a}^{\alpha\beta} = \frac{A^{\alpha\beta}}{J_{\text{in}}}, \quad a_{\alpha\beta} = J A_{\alpha\beta}, \quad a^{\alpha\beta} = \frac{A^{\alpha\beta}}{J}, \quad (158)$$

the contravariant surface metric can be written as $a^{\alpha\beta} = A^{\alpha\beta}/\lambda^2$. Thus, Eq. (157) represent linear, inhomogeneous, first-order ODEs, which are solved with variation of constants. The solution is composed of an homogeneous ('hom') and particular ('p') part, i.e.

$$\hat{a}^{\alpha\beta}(t) = \hat{a}_{\text{hom}}^{\alpha\beta}(t) + \hat{a}_{\text{p}}^{\alpha\beta}(t). \quad (159)$$

The homogeneous part is given by

$$\hat{a}_{\text{hom}}^{\alpha\beta}(t) = c_0^{\alpha\beta} \exp\left(-\frac{\mu_1}{\eta_s} t\right), \quad c_0^{\alpha\beta} = \text{const.} \quad (160)$$

The particular part is now assumed to take the form $\hat{a}_p^{\alpha\beta}(t) = c^{\alpha\beta}(t) \exp(-\mu_1/\eta_s t)$, where $c^{\alpha\beta}(t)$ denotes an unknown function. Plugging this $\hat{a}_p^{\alpha\beta}$ into the ODEs in Eq. (157) and applying some algebraic manipulations yields

$$\dot{c}^{\alpha\beta}(t) = \frac{\mu_1}{\eta_s} a^{\alpha\beta}(t) \exp\left(\frac{\mu_1}{\eta_s} t\right), \quad (161)$$

which resembles ODEs for the unknown $c^{\alpha\beta}(t)$. The solution is given by

$$c^{\alpha\beta}(t) = \int \frac{\mu_1}{\eta_s} a^{\alpha\beta}(\tilde{t}) \exp\left(\frac{\mu_1}{\eta_s} \tilde{t}\right) d\tilde{t} + c_1^{\alpha\beta}, \quad c_1^{\alpha\beta} = \text{const.} \quad (162)$$

Plugging the homogeneous and particular solution into Eq. (159) then results in the solution

$$\hat{a}^{\alpha\beta}(t) = \exp\left(-\frac{\mu_1}{\eta_s} t\right) \left[c_2^{\alpha\beta} + \frac{\mu_1}{\eta_s} \int_0^t a^{\alpha\beta}(\tilde{t}) \exp\left(\frac{\mu_1}{\eta_s} \tilde{t}\right) d\tilde{t} \right], \quad (163)$$

where the constant $c_2^{\alpha\beta} = A^{\alpha\beta}$ follows from the initial condition in Eq. (157). The integral in Eq. (163) can then be explicitly computed using $a^{\alpha\beta} = A^{\alpha\beta}/\lambda^2$ with $\lambda(t)$ given in Eq. (100). Defining $\hat{a}^{\alpha\beta}(t) := A^{\alpha\beta} \hat{a}_{\text{ev}}(t)$, with $\hat{a}_{\text{ev}}(t)$ given in Eq. (106), the intermediate surface metric is given as the initial surface metric multiplied with an evolution function.

B.1.3 Pressure from the Maxwell branch

For the Maxwell branch, the elastic energy density shown in Eq. (36) with $\Lambda = 0$ is considered. The resulting stresses are given in Eq. (37). Plugging the kinematic relations from Eq. (158) into the analytical solution for the contravariant surface metric in the intermediate configuration, $\hat{a}^{\alpha\beta}$, from Appendix B.1.2 yields

$$\frac{A^{\alpha\beta}}{J_{\text{in}}} = A^{\alpha\beta} \hat{a}_{\text{ev}}(t). \quad (164)$$

Multiplying Eq. (164) with the surface stretch J , eliminating $A^{\alpha\beta}$, and using $J = J_{\text{el}} J_{\text{in}}$ results in the required relation for the elastic surface stretch, i.e.

$$J_{\text{el}} = J \hat{a}_{\text{ev}}(t), \quad (165)$$

with $\hat{a}_{\text{ev}}(t)$ given in Eq. (106).

Based on the kinematic relations and the analytical solution for $\hat{a}^{\alpha\beta}$, the stresses in Eq. (37) become

$$\sigma_{1(\text{el})}^{\alpha\beta} = \frac{\mu_1}{J \hat{a}_{\text{ev}}(t)} (A^{\alpha\beta} \hat{a}_{\text{ev}}(t) - a^{\alpha\beta}). \quad (166)$$

In tensor notation, this becomes

$$\boldsymbol{\sigma}_{1(\text{el})} = \sigma_{1(\text{el})}^{\alpha\beta} (\mathbf{a}_\alpha \otimes \mathbf{a}_\beta) = \frac{\mu_1 (\mathbf{B} \hat{a}_{\text{ev}}(t) - \mathbf{i})}{J \hat{a}_{\text{ev}}(t)} = \frac{\mu_1 (\lambda^2 \hat{a}_{\text{ev}}(t) - 1)}{\lambda^2 \hat{a}_{\text{ev}}(t)} \mathbf{i} = \mu_1 \left(1 - \frac{1}{\lambda^2 \hat{a}_{\text{ev}}(t)} \right) \mathbf{i}, \quad (167)$$

where the kinematic relations for \mathbf{B} and J have been inserted. Similar to Eq. (156), the in-plane normal stress is compared to $\tilde{\sigma} = pr/2/\tilde{t}$ to obtain the pressure-stretch relation, see Eq. (105). The total pressure in the system is then given by the sum of Eqs. (104) and (105), see also Eq. (103). The surface tension w.r.t. the intermediate configuration, see also Eq. (30.1), is then given by $\hat{\gamma} = \mu_1 (1 - \lambda^{-2} \hat{a}_{\text{ev}}^{-1})$.

B.2 Pure bending of a flat strip

In this section, the analytical solution from Eqs. (110)–(112) is derived. The initially flat sheet of dimension $L \times S$ is deformed to a curved sheet with radius $r = 1/\kappa_2$. The boundary and loading conditions are chosen such that the surface stretches are equal to one, i.e. $\lambda_1 = \lambda_2 = 1$. The derivation follows the elastic case considered in Sauer and Duong (2017). The surface is parametrized by the coordinates $\xi \in [0, L]$ and $\eta \in [0, S]$, i.e. ξ points along the x -direction in Fig. 17 and η points along the y -direction. The reference and current surface can be described via the mappings

$$\mathbf{X}(\xi, \eta) = \xi \mathbf{e}_1 + \eta \mathbf{e}_2, \quad (168)$$

and

$$\mathbf{x}(\xi, \eta) = \xi \mathbf{e}_1 + r \sin \theta \mathbf{e}_2 + r (1 - \cos \theta) \mathbf{e}_3, \quad (169)$$

with $\theta := \kappa_2 \eta$. Based on these mappings, the tangent vectors follow as $\mathbf{A}_1 = \mathbf{e}_1$, $\mathbf{A}_2 = \mathbf{e}_2$, $\mathbf{a}_1 = \mathbf{e}_1$, and $\mathbf{a}_2 = \cos \theta \mathbf{e}_2 + \sin \theta \mathbf{e}_3$, and the surface normal follows as $\mathbf{n} = -\sin \theta \mathbf{e}_2 + \cos \theta \mathbf{e}_3$. The surface metrics are then given by

$$[A_{\alpha\beta}] = [A^{\alpha\beta}] = [a_{\alpha\beta}] = [a^{\alpha\beta}] = \begin{bmatrix} 1 & 0 \\ 0 & 1 \end{bmatrix}, \quad (170)$$

such that the surface stretch is $J = 1$ by construction. The curvature tensor components are given by

$$[b_{\alpha\beta}] = [b_{\beta}^{\alpha}] = [b^{\alpha\beta}] = \begin{bmatrix} 0 & 0 \\ 0 & \kappa_2 \end{bmatrix}, \quad (171)$$

such that the mean and Gaussian curvature follow as $H = \kappa_2/2$ and $\kappa = 0$, respectively. Similar to Eqs. (170)–(171), the intermediate surface metric and curvature tensor components are

$$[\hat{a}_{\alpha\beta}] = [\hat{a}^{\alpha\beta}] = \begin{bmatrix} 1 & 0 \\ 0 & 1 \end{bmatrix}, \quad \text{and} \quad [\hat{b}_{\alpha\beta}] = [\hat{b}^{\alpha\beta}] = \begin{bmatrix} 0 & 0 \\ 0 & \kappa_2^{\text{in}} \end{bmatrix}, \quad (172)$$

with inelastic curvature κ_2^{in} . The intermediate mean curvature follows from $\hat{H} = \kappa_2^{\text{in}}/2$. Further, $J_{\text{in}} = J_{\text{el}} = 1$.

Based on the Neo-Hookean and Koiter bending material models for the elastic and Maxwell branch, see Eqs. (36) and (44), the stresses are given by $\sigma^{11} = \sigma^{12} = \sigma^{21} = \sigma^{22} = 0$, as $\lambda_1 = \lambda_2 = \lambda_1^{\text{el}} = \lambda_2^{\text{el}} = 1$. The moment components are $M^{11} = M^{12} = M^{21} = 0$ and

$$M^{22} = c \kappa_2 + c_1 (\kappa_2 - \kappa_2^{\text{in}}). \quad (173)$$

The resulting in-plane stress components $N^{\alpha\beta} = \sigma^{\alpha\beta} + b_{\gamma}^{\alpha} M^{\gamma\beta}$ follow as

$$N^{11} = N^{12} = N^{21} = 0, \quad \text{and} \quad N^{22} = c \kappa_2^2 + c_1 (\kappa_2^2 - \kappa_2 \kappa_2^{\text{in}}). \quad (174)$$

As $[a_{\alpha\beta}]$ is equal to the identity matrix, see Eq. (170), it follows that $[N_{\beta}^{\alpha}] = [N^{\alpha\beta}]$. Considering a cut at θ , which is perpendicular to the normal $\boldsymbol{\nu} = \mathbf{a}_2$, the distributed bending moment on this cut can be computed as

$$M = M^{\alpha\beta} \nu_{\alpha} \nu_{\beta} = c \kappa_2 + c_1 (\kappa_2 - \kappa_2^{\text{in}}), \quad (175)$$

such that the curvature $\kappa_2(t)$ follows as given in Eq. (112).

Still, the inelastic curvature $\kappa_2^{\text{in}}(t)$ is unknown. Using Eqs. (62), (112) and (172), the ODE for κ_2^{in} is given by

$$\dot{\kappa}_2^{\text{in}} = \frac{c_1}{\eta_{\text{b}} (c + c_1)} (M - c \kappa_2^{\text{in}}), \quad (176)$$

with initial condition $\kappa_2^{\text{in}}(t = 0) = 0$. Using the definition from Eq. (111), the ODE is rewritten in the form

$$\dot{\kappa}_2^{\text{in}} + \frac{1}{\tau_b} \kappa_2^{\text{in}} = \frac{1}{c \tau_b} M(t). \quad (177)$$

In analogy to Appendix B.1.2, this ODE can be solved based on the variation of parameters. The solution reads

$$\kappa_2^{\text{in}}(t) = \frac{1}{c \tau_b} e^{-t/\tau_b} \int_0^t M(\tilde{t}) e^{\tilde{t}/\tau_b} d\tilde{t}. \quad (178)$$

Using the moment profile $M(t)$ from Eq. (108), the integral in Eq. (178) can be analytically solved such that $\kappa_2^{\text{in}}(t)$ is obtained as given in Eq. (110).

B.3 Inflated spherical shell

This section derives the analytical solution for the inflated spherical shell example from Sec. 5.4, see also Eqs. (116)–(118). The derivation of the elastic pressure, $p_{\text{el}}(t)$, can be found in Sauer et al. (2017), but it is repeated here for completeness.

B.3.1 Pressure from the elastic branch

Given the material models from Eqs. (41) and (46), the in-plane traction components are given by

$$N_{\text{el}}^{\alpha\beta} = N_a^{\text{el}} a^{\alpha\beta} + N_b^{\text{el}} b^{\alpha\beta}, \quad (179)$$

with

$$N_a^{\text{el}} := \mu \left(1 - \frac{1}{J^3} \right) + k (H - H_0)^2, \quad \text{and} \quad N_b^{\text{el}} := -k (H - H_0). \quad (180)$$

Based on the surface parametrization

$$\mathbf{x}(\phi, \theta) = \begin{bmatrix} r \cos \phi \sin \theta \\ r \sin \phi \sin \theta \\ -r \cos \theta \end{bmatrix}, \quad (181)$$

the following relations can be found

$$[a^{\alpha\beta}] = \frac{1}{r^2} \begin{bmatrix} 1/\sin^2 \theta & 0 \\ 0 & 1 \end{bmatrix}, \quad b^{\alpha\beta} = -a^{\alpha\beta}/r, \quad \text{and} \quad H = -\frac{1}{r}. \quad (182)$$

The traction vector $\mathbf{T} = \mathbf{T}^\alpha \nu_\alpha$ on a cut orthogonal to $\boldsymbol{\nu}$ then becomes

$$\mathbf{T} = (N_{\text{el}}^{\alpha\beta} \mathbf{a}_\beta + S^\alpha \mathbf{n}) \nu_\alpha = \left[N_a^{\text{el}} - \frac{N_b^{\text{el}}}{r} \right] \boldsymbol{\nu}, \quad (183)$$

where the kinematic relations from Eq. (182) have been used. Similar to Appendix B.1, the in-plane component $T_\nu := N_a^{\text{el}} - N_b^{\text{el}}/r$ needs to equilibrate the current pressure according to (Needleman, 1977)

$$p_{\text{el}} = \frac{2T_\nu}{r} = \frac{2}{r} \left[N_a^{\text{el}} - \frac{N_b^{\text{el}}}{r} \right]. \quad (184)$$

Plugging Eq. (180) into Eq. (184) and using the kinematic relations $J = \lambda^2$, $r = \lambda R$ and $H = -1/r$ yields the elastic pressure given in Eq. (117).

B.3.2 Solution of the evolution laws

To determine the Maxwell moments, the intermediate configuration needs to be fully specified. The intermediate surface metric is the same as derived in Appendix B.1.2, i.e. $\hat{a}^{\alpha\beta}(t) = A^{\alpha\beta} \hat{a}_{\text{ev}}(t)$ and $J_{\text{el}}(t) = J(t) \hat{a}_{\text{ev}}(t)$ with $\hat{a}_{\text{ev}}(t)$ given in Eq. (106). The bending of the intermediate surface follows from the solution of the evolution laws

$$\dot{\hat{b}}_{\alpha\beta} + \frac{c_1}{\eta_b} \hat{b}_{\alpha\beta} = \frac{c_1}{\eta_b} b_{\alpha\beta}(t), \quad \hat{b}_{\alpha\beta}(t=0) = B_{\alpha\beta}, \quad (185)$$

see Eq. (62). Based on the surface parametrization in Eq. (181), the relation $b_{\alpha\beta}(t) = \lambda(t) B_{\alpha\beta}$ can be derived. As Eq. (185) resembles first-order, linear, inhomogeneous ODEs, the same approach as in Appendix B.1.2 can be used in order to solve for $\hat{b}_{\alpha\beta}$. The solution is then given by

$$\hat{b}_{\alpha\beta}(t) = B_{\alpha\beta} \hat{b}_{\text{ev}}(t), \quad (186)$$

with $\hat{b}_{\text{ev}}(t)$ given in Eq. (119). Note that the function $\lambda(t)$ from Eq. (100) has been inserted to obtain a closed-form solution for $\hat{b}_{\text{ev}}(t)$.

B.3.3 Pressure from the Maxwell branch

Given the material models in Eqs. (36) and (44) with $\Lambda = 0$, the Maxwell stresses and moments follow as

$$\sigma_{1(\text{el})}^{\alpha\beta} = \frac{\mu_1}{J_{\text{el}}} (\hat{a}^{\alpha\beta} - a^{\alpha\beta}), \quad \text{and} \quad M_{1(\text{el})}^{\alpha\beta} = \frac{1}{J_{\text{el}}} \hat{f}^{\alpha\beta\gamma\delta} \kappa_{\gamma\delta}^{\text{el}}. \quad (187)$$

Using the kinematic relations from Eq. (158), $b_{\alpha\beta} = \lambda B_{\alpha\beta}$ and $B^{\alpha\beta} = \lambda^3 b^{\alpha\beta}$ yields

$$\sigma_{1(\text{el})}^{\alpha\beta} = \mu_1 \left(1 - \frac{1}{J_{\text{el}}} \right) a^{\alpha\beta}, \quad \text{and} \quad M_{1(\text{el})}^{\alpha\beta} = c_1 \hat{a}_{\text{ev}} (\lambda^2 - \lambda \hat{b}_{\text{ev}}) b^{\alpha\beta}, \quad (188)$$

with $\hat{a}_{\text{ev}}(t)$ given in Eq. (106) and $\hat{b}_{\text{ev}}(t)$ given in Eq. (119). Similar to Eq. (179), the in-plane traction components for the Maxwell branch are given by

$$N_{\text{visc}}^{\alpha\beta} = N_a^{\text{visc}} a^{\alpha\beta} + N_b^{\text{visc}} b^{\alpha\beta}, \quad (189)$$

where

$$N_a^{\text{visc}} := \mu_1 \left(1 - \frac{1}{\lambda^2 \hat{a}_{\text{ev}}} \right), \quad \text{and} \quad N_b^{\text{visc}} := \frac{c_1}{R} \hat{a}_{\text{ev}} (\hat{b}_{\text{ev}} - \lambda). \quad (190)$$

Using Eq. (184) and replacing the elastic traction components with the viscous traction components from Eq. (190) yields the pressure $p_{\text{visc}}(t)$ as given in Eq. (118).

References

- Adolfsson, K. and Enelund, M. (2003). Fractional derivative viscoelasticity at large deformations. *Nonlinear Dynamics*, **33**:301–321.
- Altenbach, H. and Eremeyev, V. (2015). On the constitutive equations of viscoelastic micropolar plates and shells of differential type. *Mathematics and Mechanics of Complex Systems*, **3**(3):273–283.

- Ambati, M. and De Lorenzis, L. (2016). Phase-field modeling of brittle and ductile fracture in shells with isogeometric NURBS-based solid-shell elements. *Computer Methods in Applied Mechanics and Engineering*, **312**:351–373.
- Ambati, M., Kiendl, J., and De Lorenzis, L. (2018). Isogeometric Kirchhoff–Love shell formulation for elasto-plasticity. *Computer Methods in Applied Mechanics and Engineering*, **340**:320–339.
- Amin, A., Lion, A., Sekita, S., and Okui, Y. (2006). Nonlinear dependence of viscosity in modeling the rate-dependent response of natural and high damping rubbers in compression and shear: Experimental identification and numerical verification. *International Journal of Plasticity*, **22**(9):1610–1657.
- Bartezzaghi, A., Dedè, L., and Quarteroni, A. (2019). Biomembrane modeling with isogeometric analysis. *Computer Methods in Applied Mechanics and Engineering*, **347**:103–119.
- Benson, D. J., Hartmann, S., Bazilevs, Y., Hsu, M.-C., and Hughes, T. J. R. (2013). Blended isogeometric shells. *Computer Methods in Applied Mechanics and Engineering*, **255**:133–146.
- Bonet, J. (2001). Large strain viscoelastic constitutive models. *International Journal of Solids and Structures*, **38**(17):2953–2968.
- Borden, M. J., Scott, M. A., Evans, J. A., and Hughes, T. J. R. (2011). Isogeometric finite element data structures based on Bézier extraction of NURBS. *International Journal for Numerical Methods in Engineering*, **87**(1–5):15–47.
- Borzeszkowski, B., Lubowiecka, I., and Sauer, R. A. (2022). Nonlinear material identification of heterogeneous isogeometric kirchhoff–love shells. *Computer Methods in Applied Mechanics and Engineering*, **390**:114442.
- Ciarlet, P. G. (2005). An introduction to differential geometry with applications to elasticity. *Journal of Elasticity*, **78**(1):1–215.
- Coleman, B. D. and Noll, W. (1961). Foundations of linear viscoelasticity. *Reviews of Modern Physics*, **33**:239–249.
- Cottrell, J., Hughes, T., and Bazilevs, Y. (2009). *Isogeometric Analysis: Toward integration of CAD and FEA*. Wiley.
- Crochet, M. and Naghdi, P. (1969). A class of simple solids with fading memory. *International Journal of Engineering Science*, **7**(12):1173–1198.
- Dadgar-Rad, F. and Firouzi, N. (2021). Time-dependent response of incompressible membranes based on quasi-linear viscoelasticity theory. *International Journal of Applied Mechanics*, **13**(3):2150036.
- Deng, X., Korobenko, A., Yan, J., and Bazilevs, Y. (2015). Isogeometric analysis of continuum damage in rotation-free composite shells. *Computer Methods in Applied Mechanics and Engineering*, **284**:349–372.
- Dörr, D., Schirmaier, F. J., Henning, F., and Kärger, L. (2017). A viscoelastic approach for modeling bending behavior in finite element forming simulation of continuously fiber reinforced composites. *Composites Part A: Applied Science and Manufacturing*, **94**:113–123.
- Dortdivanlioglu, B. and Javili, A. (2021). Boundary viscoelasticity theory at finite deformations and computational implementation using isogeometric analysis. *Computer Methods in Applied Mechanics and Engineering*, **374**:113579.

- Duong, T. X., Itskov, M., and Sauer, R. A. (2022). A general isogeometric finite element formulation for rotation-free shells with in-plane bending of embedded fibers. *International Journal for Numerical Methods in Engineering*, **123**(14):3115–3147.
- Duong, T. X., Roohbakhshan, F., and Sauer, R. A. (2017). A new rotation-free isogeometric thin shell formulation and a corresponding continuity constraint for patch boundaries. *Computer Methods in Applied Mechanics and Engineering*, **316**:43–83.
- Echter, R., Oesterle, B., and Bischoff, M. (2013). A hierarchic family of isogeometric shell finite elements. *Computer Methods in Applied Mechanics and Engineering*, **254**:170–180.
- Evans, E. and Hochmuth, R. (1976). Membrane viscoelasticity. *Biophysical Journal*, **16**:1–11.
- Evans, J. A., Bazilevs, Y., Babuška, I., and Hughes, T. J. (2009). n-Widths, sup-infs, and optimality ratios for the k-version of the isogeometric finite element method. *Computer Methods in Applied Mechanics and Engineering*, **198**(21):1726–1741.
- Fancello, E., Ponthot, J.-P., and Stainier, L. (2006). A variational formulation of constitutive models and updates in non-linear finite viscoelasticity. *International Journal for Numerical Methods in Engineering*, **65**:1831–1864.
- Faroughi, S., Shafei, E., and Rabczuk, T. (2020). Anisotropic solid-like shells modeled with NURBS-based isogeometric approach: Vibration, buckling, and divergence analyses. *Computer Methods in Applied Mechanics and Engineering*, **359**:112668.
- Ghaffari, R., Duong, T. X., and Sauer, R. A. (2018). A new shell formulation for graphene structures based on existing ab-initio data. *International Journal of Solids and Structures*, **135**:37–60.
- Ghaffari, R., Shirazian, F., Hu, M., and Sauer, R. A. (2019). A nonlinear hyperelasticity model for single layer blue phosphorus based on ab initio calculations. *Proceedings of the Royal Society A: Mathematical, Physical and Engineering Sciences*, **475**(2229):20190149.
- Govindjee, S. and Simo, J. C. (1992). Mullins’ effect and the strain amplitude dependence of the storage modulus. *International Journal of Solids and Structures*, **29**(14):1737–1751.
- Gupta, A., Steigmann, D. J., and Stölken, J. S. (2007). On the evolution of plasticity and incompatibility. *Mathematics and Mechanics of Solids*, **12**(6):583–610.
- Helfrich, W. (1973). Elastic properties of lipid bilayers: Theory and possible experiments. *Zeitschrift für Naturforschung C*, **28**(11–12):693–703.
- Hernandez, E., Naranjo, C., and Vellojin, J. (2020). Modelling of thin viscoelastic shell structures under Reissner–Mindlin kinematic assumption. *Applied Mathematical Modelling*, **79**:180–199.
- Hirschler, T., Bouclier, R., Duval, A., Elguedj, T., and Morlier, J. (2019). The embedded isogeometric Kirchhoff–Love shell: From design to shape optimization of non-conforming stiffened multipatch structures. *Computer Methods in Applied Mechanics and Engineering*, **349**:774–797.
- Holzappel, G. A. and Gasser, T. C. (2001). A viscoelastic model for fiber-reinforced composites at finite strains: Continuum basis, computational aspects and applications. *Computer Methods in Applied Mechanics and Engineering*, **190**(34):4379–4403.

- Hossain, M., Possart, G., and Steinmann, P. (2010). A finite strain framework for the simulation of polymer curing. Part II. Viscoelasticity and shrinkage. *Computational Mechanics*, **46**:363–375.
- Hughes, T. J. R., Cottrell, J. A., and Bazilevs, Y. (2005). Isogeometric analysis: CAD, finite elements, NURBS, exact geometry and mesh refinement. *Computer Methods in Applied Mechanics and Engineering*, **194**(39–41):4135–4195.
- Huynh, G., Zhuang, X., Bui, H., Meschke, G., and Nguyen-Xuan, H. (2020). Elasto-plastic large deformation analysis of multi-patch thin shells by isogeometric approach. *Finite Elements in Analysis and Design*, **173**:103389.
- James, K. A. and Waisman, H. (2016). On the importance of viscoelastic response consideration in structural design optimization. *Optimization and Engineering*, **17**:631–650.
- Javili, A. and Steinmann, P. (2009). A finite element framework for continua with boundary energies. Part I: The two-dimensional case. *Computer Methods in Applied Mechanics and Engineering*, **198**(27):2198–2208.
- Javili, A. and Steinmann, P. (2010). A finite element framework for continua with boundary energies. Part II: The three-dimensional case. *Computer Methods in Applied Mechanics and Engineering*, **199**(9):755–765.
- Kang, P. and Youn, S.-K. (2016). Isogeometric topology optimization of shell structures using trimmed NURBS surfaces. *Finite Elements in Analysis and Design*, **120**:18–40.
- Kästner, M., Obst, M., Brummund, J., Thielsch, K., and Ulbricht, V. (2012). Inelastic material behavior of polymers – Experimental characterization, formulation and implementation of a material model. *Mechanics of Materials*, **52**:40–57.
- Kiendl, J., Ambati, M., De Lorenzis, L., Gomez, H., and Reali, A. (2016). Phase-field description of brittle fracture in plates and shells. *Computer Methods in Applied Mechanics and Engineering*, **312**:374–394.
- Kiendl, J., Bletzinger, K.-U., Linhard, J., and Wüchner, R. (2009). Isogeometric shell analysis with Kirchhoff-Love elements. *Computer Methods in Applied Mechanics and Engineering*, **198**:3902–3914.
- Kiendl, J., Hsu, M.-C., Wu, M. C., and Reali, A. (2015). Isogeometric Kirchhoff-Love shell formulations for general hyperelastic materials. *Computer Methods in Applied Mechanics and Engineering*, **291**:280–303.
- Kiendl, J., Schmidt, R., Wüchner, R., and Bletzinger, K.-U. (2014). Isogeometric shape optimization of shells using semi-analytical sensitivity analysis and sensitivity weighting. *Computer Methods in Applied Mechanics and Engineering*, **274**:148–167.
- Koh, S. and Eringen, A. (1963). On the foundations of non-linear thermo-viscoelasticity. *International Journal of Engineering Science*, **1**(2):199–229.
- Li, F. (2012). A justification of two-dimensional nonlinear viscoelastic shells model. *Abstract and Applied Analysis*, 2012:1–24.
- Liu, L., Yu, M., Lin, H., and Foty, R. (2017). Deformation and relaxation of an incompressible viscoelastic body with surface viscoelasticity. *Journal of the Mechanics and Physics of Solids*, **98**:309–329.

- Lubarda, V. (2004). Constitutive theories based on the multiplicative decomposition of deformation gradient: Thermoelasticity, elastoplasticity, and biomechanics. *Applied Mechanics Reviews*, **57**(1–6):95–108.
- Lubarda, V. (2011). Rate-type elasticity and viscoelasticity of an erythrocyte membrane. *Journal of Mechanics of Materials and Structures*, **6**(1–4):361–376.
- Macneal, R. H. and Harder, R. L. (1985). A proposed standard set of problems to test finite element accuracy. *Finite Elements in Analysis and Design*, **1**(1):3–20.
- Marques, S. P. and Creus, G. J. (2012). *Computational viscoelasticity*. Springer Science & Business Media.
- Miehe, C. and Keck, J. (2000). Superimposed finite elastic–viscoelastic–plastoelastic stress response with damage in filled rubbery polymers. Experiments, modelling and algorithmic implementation. *Journal of the Mechanics and Physics of Solids*, **48**(2):323–365.
- Nagy, A. P., IJsselmuiden, S. T., and Abdalla, M. M. (2013). Isogeometric design of anisotropic shells: Optimal form and material distribution. *Computer Methods in Applied Mechanics and Engineering*, **264**:145–162.
- Needleman, A. (1977). Inflation of spherical rubber balloons. *International Journal of Solids and Structures*, **13**(5):409–421.
- Neff, P. (2005). A geometrically exact viscoplastic membrane-shell with viscoelastic transverse shear resistance avoiding degeneracy in the thin-shell limit. *Zeitschrift für angewandte Mathematik und Physik*, **56**:148–182.
- Nguyen, V. P., Anitescu, C., Bordas, S. P., and Rabczuk, T. (2015). Isogeometric analysis: An overview and computer implementation aspects. *Mathematics and Computers in Simulation*, **117**:89–116.
- Ogden, R. W. (1997). *Non-linear elastic deformations*. Courier Corporation.
- Paul, K., Zimmermann, C., Duong, T. X., and Sauer, R. A. (2020a). Isogeometric continuity constraints for multi-patch shells governed by fourth-order deformation and phase field models. *Computer Methods in Applied Mechanics and Engineering*, **370**:113219.
- Paul, K., Zimmermann, C., Mandadapu, K. K., Hughes, T. J. R., Landis, C. M., and Sauer, R. A. (2020b). An adaptive space-time phase field formulation for dynamic fracture of brittle shells based on LR NURBS. *Computational Mechanics*, **65**:1039–1062.
- Proserpio, D., Ambati, M., De Lorenzis, L., and Kiendl, J. (2020). A framework for efficient isogeometric computations of phase-field brittle fracture in multipatch shell structures. *Computer Methods in Applied Mechanics and Engineering*, **372**:113363.
- Reese, S. and Govindjee, S. (1998). A theory of finite viscoelasticity and numerical aspects. *International Journal of Solids and Structures*, **35**(26):3455–3482.
- Reina, C., Fokoua Djodom, L., Ortiz, M., and Conti, S. (2018). Kinematics of elasto-plasticity: Validity and limits of applicability of $F=FeFp$ for general three-dimensional deformations. *Journal of the Mechanics and Physics of Solids*, **121**:99–113.
- Roohbakhshan, F. and Sauer, R. A. (2017). Efficient isogeometric thin shell formulations for soft biological materials. *Biomechanics and Modeling in Mechanobiology*, **16**(5):1569–1597.

- Roohbakhshan, F. and Sauer, R. A. (2019). A finite membrane element formulation for surfactants. *Colloids and Surfaces A: Physicochemical and Engineering Aspects*, **566**:84–103.
- Sauer, R. A. (2014). Stabilized finite element formulations for liquid membranes and their application to droplet contact. *International Journal for Numerical Methods in Fluids*, **75**(7):519–545.
- Sauer, R. A. (2016). A contact theory for surface tension driven systems. *Mathematics and Mechanics of Solids*, **21**(3):305–325.
- Sauer, R. A. (2018). On the computational modeling of lipid bilayers using thin-shell theory. In Steigmann, D. J., editor, *The Role of Mechanics in the Study of Lipid Bilayers.*, pages 221–286. Springer International Publishing, Cham.
- Sauer, R. A. and Duong, T. X. (2017). On the theoretical foundations of thin solid and liquid shells. *Mathematics and Mechanics of Solids*, **22**(3):343–371.
- Sauer, R. A., Duong, T. X., and Corbett, C. J. (2014). A computational formulation for constrained solid and liquid membranes considering isogeometric finite elements. *Computer Methods in Applied Mechanics and Engineering*, **271**:48–68.
- Sauer, R. A., Duong, T. X., Mandadapu, K. K., and Steigmann, D. J. (2017). A stabilized finite element formulation for liquid shells and its application to lipid bilayers. *Journal of Computational Physics*, **330**:436–466.
- Sauer, R. A., Ghaffari, R., and Gupta, A. (2019). The multiplicative deformation split for shells with application to growth, chemical swelling, thermoelasticity, viscoelasticity and elastoplasticity. *International Journal of Solids and Structures*, **174-175**:53–68.
- Schillinger, D., Ruthala, P. K., and Nguyen, L. H. (2016). Lagrange extraction and projection for NURBS basis functions: A direct link between isogeometric and standard nodal finite element formulations. *International Journal for Numerical Methods in Engineering*, **108**(6):515–534.
- Schulte, J., Dittmann, M., Eugster, S., Hesch, S., Reinicke, T., dell’Isola, F., and Hesch, C. (2020). Isogeometric analysis of fiber reinforced composites using Kirchhoff–Love shell elements. *Computer Methods in Applied Mechanics and Engineering*, **362**:112845.
- Shafei, E., Faroughi, S., and Rabczuk, T. (2021). Nonlinear transient vibration of viscoelastic plates: A NURBS-based isogeometric HSDT approach. *Computers & Mathematics with Applications*, **84**:1–15.
- Shaw, S., Johnson, A., and Whiteman, J. (1999). Modelling and finite element analysis of applied polymer viscoelasticity problems. *Mathematics of Finite Elements and Applications*, **10**:63–86.
- Shutov, A., Landgraf, R., and Ihlemann, J. (2013). An explicit solution for implicit time stepping in multiplicative finite strain viscoelasticity. *Computer Methods in Applied Mechanics and Engineering*, **265**:213–225.
- Sidoroff, F. (1974). Nonlinear viscoelastic model with an intermediate configuration. [un module viscoelastique non linéaire avec configuration intermédiaire.]. *Journal de Mécanique*, **13**(4):679–713.
- Simo, J. (1987). On a fully three-dimensional finite-strain viscoelastic damage model: Formulation and computational aspects. *Computer Methods in Applied Mechanics and Engineering*, **60**(2):153–173.

- Simo, J. and Fox, D. (1989). On a stress resultant geometrically exact shell model. Part I: Formulation and optimal parametrization. *Computer Methods in Applied Mechanics and Engineering*, **72**(3):267–304.
- Sun, D., Dai, R., Liu, X., Zhan, Y., and Dong, C. (2021). RI-IGABEM for 2D viscoelastic problems and its application to solid propellant grains. *Computer Methods in Applied Mechanics and Engineering*, **378**:113737.
- Tepole, A. B., Kabaria, H., Bletzinger, K.-U., and Kuhl, E. (2015). Isogeometric Kirchhoff–Love shell formulations for biological membranes. *Computer Methods in Applied Mechanics and Engineering*, **293**:328–347.
- Thai, C. H., Nguyen-Xuan, H., Nguyen-Thanh, N., Le, T.-H., Nguyen-Thoi, T., and Rabczuk, T. (2012). Static, free vibration, and buckling analysis of laminated composite Reissner–Mindlin plates using NURBS-based isogeometric approach. *International Journal for Numerical Methods in Engineering*, **91**(6):571–603.
- Toshniwal, D., Speleers, H., and Hughes, T. J. (2017). Smooth cubic spline spaces on unstructured quadrilateral meshes with particular emphasis on extraordinary points: Geometric design and isogeometric analysis considerations. *Computer Methods in Applied Mechanics and Engineering*, **327**:411–458.
- Valizadeh, N. and Rabczuk, T. (2019). Isogeometric analysis for phase-field models of geometric PDEs and high-order PDEs on stationary and evolving surfaces. *Computer Methods in Applied Mechanics and Engineering*, **351**:599–642.
- Vu-Bac, N., Duong, T., Lahmer, T., Zhuang, X., Sauer, R., Park, H., and Rabczuk, T. (2018). A NURBS-based inverse analysis for reconstruction of nonlinear deformations of thin shell structures. *Computer Methods in Applied Mechanics and Engineering*, **331**:427–455.
- Zhang, W., Li, D., Kang, P., Guo, X., and Youn, S.-K. (2020). Explicit topology optimization using IGA-based moving morphable void (MMV) approach. *Computer Methods in Applied Mechanics and Engineering*, **360**:112685.
- Zimmermann, C., Toshniwal, D., Landis, C. M., Hughes, T. J. R., Mandadapu, K. K., and Sauer, R. A. (2019). An isogeometric finite element formulation for phase transitions on deforming surfaces. *Computer Methods in Applied Mechanics and Engineering*, **351**:441–477.